# Attosecond Dynamics in Molecules and on Interfaces

Dissertation

von

**Michael Jobst**

## Fakultät für Physik

Laser– und Röntgenphysik

# Attosecond Dynamics in Molecules and on Interfaces

### Michael Johannes Jobst

# Abstract

In this thesis three experimental approaches to the measurement of electronic movement on the attosecond time scale in complex systems are presented. The first chapter describes the basic theory and technology necessary for these endeavors as well as the actual equipment used and refined during this thesis.

The subsequent chapters present the experiments on three different types of systems: molecules in the gas phase (specifically ozone), molecules on surfaces (metal-organic molecules on semiconductors) and metal surfaces and interfaces (tungsten in two crystal orientations and oxygen on tungsten).

The first of these three chapters begins with a report on the development of a high purity ozone source. The creation of ultrashort deep UV pulses (ca. 220 nm–300 nm) through frequency tripling for pump probe experiments and the suppression of the NIR fundamental light is described. The combination of UV and isolated XUV pulses in an experiment is realized and demonstrated on ozone. An overview over the current theory on electron dynamics in ozone in the Frank–Condon region is given and complemented with the current status of the time dependent measurements.

The second chapter focuses on the sample choice for the detection of a time dependent chemical shift in photoelectron spectroscopy experiments with metal-organic molecules on semiconductor surfaces. Observation of the metal center as well as iodine tagging for improved XUV sensitivity are explored.

In the third chapter the recent measurements of attosecond delays between photoelectron emission from the tungsten 4f and valence levels are described. In a first step the extension of the experimentally usable XUV spectrum up to energies of 150 eV is reported, then streaking measurements at 145 eV photon energy are demonstrated. The multitude of theoretical explanations for the origin of photoemission delays in tungsten is summarized and compared with experimental results. Delay measurements at 145 eV and their results on W(110), W(100) and oxygen on tungsten are presented. A synthesis of all measurements on clean tungsten, oxygen on tungsten and hydrogen on tungsten that have been performed before and during this thesis is given.

At the end of every chapter there is a section containing conclusions and an outlook for the respective experiments.

# Kurzzusammenfassung

Im Rahmen dieser Arbeit werden drei experimentelle Ansätze zur Messung von Elektronendynamik auf der Attosekunden Zeitskala präsentiert. Das erste Kapitel befasst sich mit der zu Grunde liegenden Theorie, Technologie und den für diese Arbeit verwendeten und verbesserten Geräten.

Die darauf folgenden Kapitel präsentieren Experimente an drei verschiedenen Klassen von Systemen: gasförmige Moleküle (Ozon), Moleküle auf Oberflächen (metallorganische Moleküle auf Halbleitern) sowie Metall Oberflächen und Grenzflächen (Wolfram in zwei verschiedenen Kristallorientierungen und Sauerstoff auf Wolfram).

Im ersten dieser drei Kapitel wird zunächst die Konstruktion einer Quelle für hochreines Ozon beschrieben. Die Herstellung von ultrakurzen Pulsen für Anrege Abfrage Experimente im tiefen UV (ca. 220 nm–300 nm) durch Frequenzverdreifachung von Nahinfrarot Pulsen wird erläutert. Die Kombination von Attosekunden XUV Pulsen und Femtosekunden UV Pulsen in einem Experiment wird gezeigt. Die hierfür nötige Unterdrückung des Nahinfrarot Treiberpulses wird behandelt. Die relevante Theorie zur Elektronendynamik in Ozon in der Frank–Condon Region wird präsentiert und deren Ergebnisse mit dem momentanen Status der zeitaufgelösten Messungen verglichen.

Das zweite der experimentellen Kapitel konzentriert sich auf die Auswahl einer vielversprechenden Probe für die Detektion einer zeitabhängigen chemischen Verschiebung in Photoelektronen Experimenten an metallorganischen Molekülen auf Halbleiter Oberflächen. Die direkte Detektion durch Beobachtung des Metall Zentrums sowie eine indirekte Messung an Molekülen, die mit Jod Atomen markiert wurden, wird diskutiert.

Im dritten Kapitel werden die jüngsten Attosekunden Messungen zur Verzögerung der Photoemission zwischen den Wolfram 4f und Valenz Niveaus beschrieben. Zunächst wird über die Ausweitung der erreichbaren Photonenenergie berichtet. Streaking Messungen bei 145 eV werden demonstriert, wobei das Photonen Spektrum sich bis mindestens 150 eV erstreckt. Die theoretischen Ansätze zur Erklärung der gemessenen Verzögerungen werden zusammen gefasst und mit experimentellen Resultaten verglichen. Verzögerungsmessungen an W(110), W(100) und Sauerstoff auf Wolfram werden gezeigt. Ein Überblick über alle bisher erfolgten Messungen an sauberem Wolfram, Sauerstoff auf Wolfram und Wasserstoff auf Wolfram wird gegeben.

Zu Ende jedes Kapitels befinden sich sowohl eine Zusammenfassung der jeweiligen Experimente als auch der zugehörige Ausblick.

# Contents

# Chapter 1

# Introduction

Electronic motion on the Angstrom length scale is a fundamental process that drives a wide variety of phenomena from chemical bond rupture to photosynthesis. In order to truly understand the evolution of these microscopic phenomena one needs to trace the charges as they are moving, which can demand an extremely high temporal resolution. Microscopic motion is determined by the evolution of coherent superpositions of electronic states (wavepackets). The time scale of the dynamics of these wavepackets is given by $h/\Delta E$, where $h$ is Planck's constant and $\Delta E$ is the energy separation of the levels involved in the formation of the wavepacket. The typical energy scale of valence electron dynamics is known from spectroscopy to be in the range of a few electron volts. This translates to a time scale in the range of attoseconds ($1\,\text{as} = 1 \times 10^{-18}\,\text{s}$) to few femtoseconds ($1\,\text{fs} = 1 \times 10^{-15}\,\text{s}$). This time resolution has only been available for little more than a decade [1] and so it comes as no surprise that a significant part of the research performed so far focused on the development and refinement of experimental techniques. In the following section an overview over selected approaches to study electronic motion on an ultrashort timescale is given.

## Attosecond Experimental Techniques

In order to get experimental access to the electron dynamics we need a time gating mechanism on the attosecond scale: either be a process internal to the sample or an externally applied field.

One technique that uses an internal process is the Core Hole Clock [2]. It can for example be used to measure charge transfer times in dielectric adsorbates on metals and is typically performed in synchrotron facilities where tunable and intense X–ray pulses are available. When the sample is exposed to the X–ray beam, a photon excites a core electron of the adsorbate and creates a core hole. The hole is filled within its characteristic lifetime and simultaneously the charge transfer process from the excited state of the adsorbate to the surface takes place. In an autoionization process an electron is ejected from the adsorbate and subsequently detected. The ratio between the lifetimes of the excited state and the core hole can be calculated from the kinetic energy distribution of this electron when the photon energy is varied. If the core hole lifetime is very short, well known and comparable to the exciton lifetime it is possible to achieve attosecond time resolution, which was demonstrated by Föhlisch et al. for sulfur on ruthenium [2]. We can conclude that the core hole clock is a powerful method for the measurement of

charge transfer times, but it does require quite specific properties from the sample in order to be usable.

From here on we will focus on approaches utilizing externally applied field gradients, which promises greater versatility. The key towards a much higher time resolution lies in taking the step from the envelope of the laser field to the oscillating electromagnetic field of the laser. This is achieved by controlling the carrier envelope phase[1] (CEP) with the technology pioneered by Udem et al. [3]. For few cycle pulses[2] changes in CEP affect the temporal shape of the electric field significantly. The combination of few cycle pulses and CEP stabilization yields control over temporal field gradients on the attosecond timescale [4].

Few cycle pulses in the near infrared (NIR) range are used for a variety of different experiments, among which we have selected three to present here. The first example is the attoclock [5]. In this setup an intense circularly polarized few cycle laser pulse is used to photoionize helium atoms. From the radial distribution of the resulting photoelectrons Eckle et al. draw conclusions about a lower bound to the tunneling time of the photoelectron [6]. While the interpretation of this measurement is challenging [7] it does provide information about electron dynamics on a very short timescale.

Another noteworthy experiment is the investigation of nonsequential double ionization [8]. Bergues et al. report a strong CEP dependent correlation in the electron emission from argon when double ionized with few cycle laser pulses–a clear signature of ultrafast multielectron dynamics. For this experiment the carrier envelope phase was not stabilized– but it was measured for every single laser shot [9]. Then the acquired data was mapped to the phase and revealed the CEP dependence.

In both of the just mentioned publications the scrutinized effect depends nonlinearly on the electric field. This is not a coincidence but a necessary property when employing few cycle pulses for attosecond time gating. The contrast in field strength between the two most intense field peaks is only about 1.3 for even the shortest conventionally achievable pulses. If the studied effect depends exponentially on the field strength (as tunneling does) the effective time contrast is enhanced such that the effect is limited to an attosecond interval within the most intense optical cycle.

The third example is high harmonic spectroscopy (HHS) [10]. When gas atoms are subjected to an intense laser field they can go through a three step process: ionization, acceleration of the released electron away from and then back to the ion in the reversing laser field, and recombination of the accelerated electron with the parent ion [11]. The energy accumulated in the field is released as a soft X–ray (or extreme ultra violet, XUV) photon. Since the returning electron is well defined in space and time one can in principle extract information with Angstrom spatial and attosecond temporal resolution from the resulting photon spectrum. In fact, there have been reports on tomographic measurements of molecular orbitals [12], vibrational excitations [13] and even chemical reactions [14]. HHS is often labeled as a pump–probe type experiment. In this picture the

---

[1]The carrier envelope phase describes the phase of the light oscillations within the envelope. For a CEP of 0 or $\pi$ the maximum of an oscillation coincides with the envelope maximum.

[2]Pulses that are so short that they containing less than two field oscillations

ionizing laser field represents a pump pulse (starting the dynamics of interest) while the returning electron takes the role of the probe (reading out the properties of the system). In a standard pump–probe experiment the temporal evolution of a system is studied by scanning the time delay between the two pulses. For HHS the time delay is determined by the oscillation period of the driving laser (i.e. the central wavelength), which is either challenging or impossible to change significantly.

## Attosecond Pulses

In order to perform pump–probe experiments in the conventional sense attosecond pulses are necessary. It has been shown that the XUV pulses that are used as an observable in HHS can serve this purpose. If the high harmonic generation (HHG) process is performed with a long driving pulse (containing significantly more than two field oscillations) the harmonics will form pulse trains spaced in time by half an oscillation period of the driving laser. Due to the high photon energy of the XUV pulses they offer access to electrons beyond the valence shell and enable the measurement of dynamic chemical shifts of core levels [15]. Of course the time resolution for pulse trains is limited by the duration of the train, not the individual pulses. If intense few cycle pulses are used to drive the HHG process and the resulting radiation is carefully manipulated, one can obtain isolated XUV pulses as short as 67 as [16]. Two of the ways in which isolated attosecond XUV pulses can be applied in pump–probe experiments will be presented here. The first one is called attosecond transient absorption spectroscopy (ATTAS), the second one is attosecond photoelectron spectroscopy (APS).

For ATTAS, the XUV probe beam is focused onto the sample, is transmitted through it and then analyzed with a spectrometer. Absorption lines of the sample that overlap with the XUV spectrum are detected as dips in the spectral intensity. As the delay between NIR pump and XUV probe beam is varied one can draw conclusions about the population of electronic states from the temporal evolution of these dips. One beneficial property of ATTAS is the fact that the time and energy resolution are not coupled. The time resolution of ATTAS is limited by the pulse length of the XUV probe pulse. Even if the driving pulse is longer than the probe pulse it is still phase locked and thus the optical field is identical for every pulse. The XUV pulse can then read out the evolution of the sample within the electric field with attosecond resolution. The spectral resolution is limited by the employed spectrometer–not the spectral resolution of NIR or XUV pulses. Due to this the ATTAS method can be used to study slow processes (for which high spectral resolution is necessary) and fast processes (requiring high temporal resolution) simultaneously. It has been used to measure valence electron motion in krypton atoms [17] and showed that strong–field ionization can produce long lived coherences. The method is also applicable to thin solids as was shown by Schultze et al. [18] who scrutinized the change in the electronic structure of fused silica exposed to intense laser radiation.

The second experimental ansatz utilizing isolated XUV pulses is attosecond photoelectron spectroscopy (APS). This approach is used for all experiments presented in this thesis. In APS the XUV probe pulse ionizes the sample, thereby releasing photoelectrons which

are subsequently detected and analyzed. In contrast to ATTAS no resonance overlapping with the XUV spectrum is necessary and APS is applicable to a very broad range of samples. One merely needs an appreciable absorption cross section in the energy range of the XUV pulse. The temporal and spectral resolution of APS are both limited by the same quantity: the bandwidth of the XUV pulse. This means that compromises have to be made when determining the appropriate bandwidth for the specific experiment. At the currently achievable photon energies APS cannot be used to study dynamics in bulk solids because photoelectrons with the kinetic energies typically produced by XUV pulses have a mean free path in solids of only a few Angstrom. Only the photoelectrons created within a few layers from the surface can escape the solid and be detected. On the other hand APS is very well suited for surface dynamics.

There is a special variant of APS, called streaking, which essentially measures a cross correlation between the photoelectrons and the NIR laser field [1]. It can provide information on the release time of photoelectrons relative to the driving field with a precision of less than ten attoseconds as demonstrated in neon gas [19]. The method is also applicable to monocrystalline, polycrystalline and amorphous solids [20, 21]. A particularly intriguing experiment on a complex layered sample was performed by Neppl et al. [22]. The authors fabricated a tungsten crystal with a monolayer of magnesium on top. They then varied the thickness of the adlayer between one and four atomic layers and measured the corresponding emission delay between the tungsten 4f level and the magnesium 2p level. They found the delay to increase linearly with the adlayer thickness, which is a direct measurement of two effects:

- electronic transport on the attosecond and angstrom scale through the magnesium layer.

- dielectric screening on the angstrom scale at the vacuum/magnesium interface. The observed increase in delay can only be explained with a vanishing penetration depth of the NIR streaking field into the magnesium.

### Current Advances in Attosecond Dynamics in Molecules and on Interfaces

As mentioned in the first paragraph of the introduction, new experimental techniques had to be developed for many exciting findings in attosecond science so far. But now this branch of ultrafast physics matures and there are an increasing number of reports on applications of tried and tested methods exploring new samples or refining previous findings. The three projects presented in this thesis form a microcosm of this evolution. In the first project one we explore a new experimental ansatz–the combination of deep UV pulses and APS on ozone. For the second one we study a very complex sample: molecular layers on surfaces. And for the third one we synthesize and expand previous photoemission delay measurements on tungsten. These three experiments are summarized in the following paragraph.

- *Attosecond photoelectron spectroscopy of electron dynamics in ozone triggered by deep UV pulses.*

The photophysics of ozone play a vital role for life on our planet. Stratospheric ozone absorbs a large part of the UV-B radiation that causes DNA damage [23] due to its high photon energy. After the discovery of ozone depletion and the ozone hole [24, 25] there have been extensive studies of its photodissociation [26]. Even decades later the research topic is still being pursued and the decay channels are being studied with ever greater precision. Yet so far all the performed studies lacked one crucial experimental feature: the time resolution to track the electron motion triggering the decay. Even though the dissociation itself takes place on the timescale of ca. 30 fs the dynamics within the valence electronic states that precedes it will happen within the first few femtoseconds of an excitation by UV light. During this time the nuclei can still be regarded as stationary [27]. In addition to being the first experimental studies on the onset of photodissociation of ozone our experiments would also be the first deep UV pump/XUV probe studies with isolated attosecond pulses. Here we present steps that were undertaken in order to shed light on these first few femtoseconds of time evolution.

We designed and built a frequency tripling device capable of producing 7 µJ deep UV pulses centered at 260 nm from 540 µJ NIR pulses centered at 780 nm. The UV pulses were combined with isolated attosecond XUV pulses for time resolved experiments on ozone. The current theory on valence electron motion in ozone is reviewed and compared with the first experimental results.

The development of an apparatus capable of measuring UV induced electron dynamics in molecules at the attosecond time scale opens the door for many possible applications. The basic building blocks of life, the amino acids guanine, thymine, cytosine and adenine all have a strong and broad absorption band that overlaps at least partially with our UV spectrum. This means that it is in principle possible to induce dynamics in them with the experimental tools at our disposal– and there have been theoretical findings that predict experimentally accessible attosecond electron dynamics on selected peptides [28, 29].

- *Attosecond photoelectron spectroscopy of electron dynamics in metal–organic molecules on semiconductor surfaces.*
  Metal-organic molecules are widespread in nature, with heme or chlorophyll being particularly prominent examples. Similar molecules also have technical applications as sensitizers in solar cells [30, 31]. In a standard solar cell the absorption range of silicon limits the working bandwidth of the device. In the dye sensitized solar cell (called Grätzel cell) the absorption range can be tuned through the selection of suitable dye molecules as adlayers on semiconductors. Let us discuss the working cycle of the Grätzel cell in more detail: Due to the absorption of a photon there is an intramolecular charge rearrangement as electrons are lifted to the excited state. The charge density of this excited state compared to the ground state is typically lower on the metal center and higher on the organic part of the molecule (constituting a metal to ligand charge transfer). Then the electron is transferred to the substrate, which was found to happen within less than 3 fs in a model system [32]. In the solar cell the circuit has to be closed via a liquid redox system surrounding

the semiconductor substrate. Our object of interest is the hithertho unexplained very first step: intramolecular charge rearrangement. We study the dynamic chemical shift of core electrons in a selected atom within the metal–organic molecule as a proxy to the charge density in its vicinity and its temporal evolution.

This is the first experiment with molecular layers on surfaces with our setup. Transitioning from crystalline solid samples to molecule layers promises a drastically lower signal and naturally our first step is the choice of a detectable sample. We determine whether the chosen molecules can be properly prepared and yield a strong enough signal for time dependent investigations. After careful studies on selected molecules we can conclude that iodine tagged phthalocyanines are very promising candidates.

- *Streaking measurements of photoemission delays in tungsten and oxygen on tungsten at high photon energies.*

  Due to the ongoing miniaturization of semiconductor electronics electron transport through few atomic layers will soon be an important topic for transistor development. Attosecond delay spectroscopy provides a unique approach to study electron transport on the attosecond and angstrom scale. The first such experiment was performed by Cavalieri et al. [20]. They reported that the photoemission from the tungsten 4f level was delayed by $(110 \pm 70)$ as with respect to the valence band. Obviously the error bars on this measurement are quite high and allow room for different theoretical approaches. The challenging interpretation of the result is best illustrated by a short overview of the multitude of physical origins proposed in theoretical publications. Localization properties, static band structure, surface contributions, scattering effects and interference have all been suggested in recent years and were all able to explain the measured value. In this work we strove to broaden the data basis and provide measurements over a broad range of photon energies. We extended the accessible XUV energies up to $150\,\text{eV}$ and performed streaking measurements at $145\,\text{eV}$. We have unveiled a step-like behavior in the relationship between photon energy and delay. This feature exists for both the (110) and (100) crystal orientation, which makes the static band structure an unlikely explanation. This is a particularly interesting finding because it could hint at a lower bound for the minimum time necessary for the establishment of a band structure in tungsten.

# Chapter 2

# Experimental and Theoretical Tools

## 2.1 Principles of Attosecond Experiments

In order to measure or control phenomena on a certain timescale one needs a gating mechanism which works on the same order as the phenomenon one is interested in. In the traditional photo camera this mechanism is provided by a shutter that generally blocks light but lets it pass for a short time once activated. Our research interest lies on timescales that are prohibitively short for any kind of mechanical or even electronic gating. So we are taking a different approach. We put ourselves in the equivalent situation to taking a photograph in a dark room with a long exposure time – but with a very short flash. These very short pulses and the tools used to create and measure them are described in the following sections.

### 2.1.1 Few Femtosecond Pulses

Consider the following representation of the electric field of a laser pulse at an arbitrary point in space:

$$\vec{E}(t) = \tilde{E}(t)e^{i\phi_{CE}}e^{i\phi(t)}e^{i\omega_L t}, \tag{2.1}$$

with the real envelope function $\tilde{E}(t)$, the carrier envelope phase (CEP) $\phi_{CE}$, the temporal phase $\phi(t)$ and the central frequency of the laser $\omega_L$. The envelope in the cases relevant to us is well represented by a Gaussian of form

$$\tilde{E}(t) = \vec{E}_0 exp(-\frac{2\ln 2}{\tau_L^2}t^2), \tag{2.2}$$

where $\tau_L$ denotes the full width at half maximum of the pulse. The derivative of the temporal phase defines the instantaneous frequency,

$$\omega(t) = \omega_L + \frac{\mathrm{d}}{\mathrm{d}t}\phi(t). \tag{2.3}$$

We can perform an expansion of $\phi(t)$ in powers of $t$,

$$\phi(t) = a_0 t + a_1 t^2 + a_2 t^3 + \dots \tag{2.4}$$

There is no constant term in this expansion because the time independent part of the phase is included in the carrier envelope phase. If there are nonzero terms $a_n$ the pulse
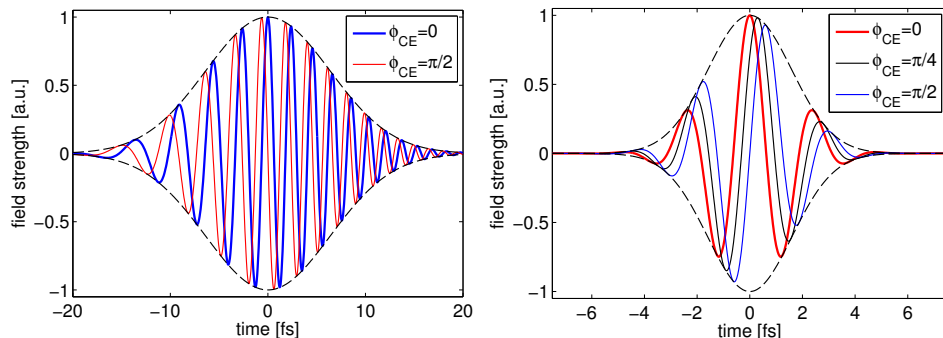
(a) Two 15 fs pulses at 780 nm with positive second order chirp (lower frequencies arrive first) and two different CEP values

(b) Three 1.5 cycle pulses with flat spectral phase and multiple carrier envelope phases.

Figure 2.1: In direct comparison it is apparent that the CEP only plays a role in temporal space when dealing with very short pulses: the longer pulse in **a)** does not change its shape as strongly as the few cycle pulse shown in **b)**. Both pulses are centered at the typical wavelength for our experiments: 780 nm

is called chirped, with the chirp being linear, quadratic, cubic etc for $n = 0, 1, 2,$ etc. For the shortest possible pulse length, which is called Fourier limited, $a_n = 0$ for all $n > 0$ is necessary [33]. This is called a flat phase. Consider a pulse with $\phi(t) = 0$. The CEP then defines the relative position of the oscillations at a constant frequency $\omega_L$ within the envelope. This is an important property when considering pulses that are not much longer than the oscillation period of the electromagnetic field. Figure 2.1 shows such a pulse with $\tau_L = 3.75$ fs and a period $\Delta\tau_{FWHM}$ of 2.5 fs. This is called a 1.5 cycle pulse because the temporal full width at half maximum $\Delta\tau_{FWHM}$ is equal to 1.5 times the period. Alongside it there is a 15 fs pulse that can no longer be considered a few cycle pulse. We varied the CEP by $\pi/2$ to show the maximum change for both pulses[1]. The discussion here was conducted in real space. A similar discussion holds in frequency space.

### 2.1.2 Generation of Isolated Attosecond Pulses

In order to perform experiments on the attosecond timescale we need access to pulses with sub femtosecond durations. This section will explain how we employ CE-phase-locked pulses in the near infrared (NIR) to generate attosecond pulses in the extreme ultraviolet (XUV). Since the period of the electromagnetic field is a limiting factor for the pulse length the much shorter attosecond pulses have to be at a higher frequency.

---

[1] Of course the periodicity is actually $2\pi$, but in many experiments (most notably in the gas phase) a global sign reversal of the field does not play a role due to the inversion symmetry of the gas. So the interesting periodicity reduces to $\pi$

The standard approach for obtaining these pulses is called high harmonic generation (HHG) [10]. In this process an intense linearly polarized laser pulse is focused into a gas target. When a medium is exposed to intense electromagnetic waves the linear polarization response does not apply. The polarization in the material can be expressed as

$$
\begin{aligned}
P =& \tilde{\epsilon}_0 \left( \chi^{(1)} E_L(t) + \chi^{(2)} E_L(t)^2 + \chi^{(3)} E_L(t)^3 + \dots \right) \\
\equiv& P^{(1)}(t) + P^{(2)}(t) + P^{(3)}(t) + \dots,
\end{aligned}
\tag{2.5}
$$

where $\tilde{\epsilon}_0$ denotes the vacuum permittivity, $\chi$ is the susceptibility, $P(t)$ is the polarization vector and $E_L(t)$ is the electric field [33]. This approach follows perturbation theory and works well for low order harmonics (we will follow up on this in chapter 2.1.4). We can easily see that it predicts the yield for higher harmonics to diminish exponentially with increasing order (this is the region labeled perturbative regime in figure 2.3). For higher energies (the plateau region in figure 2.3), the perturbatory approach breaks down. For very intense laser pulses[2] the harmonics of low orders indeed decrease exponentially, but the higher orders in the plateau region are produced with almost constant efficiency up to a certain cutoff frequency. This curious behavior can be explained in the semiclassical three step model (illustrated in figure 2.2). It describes the process as follows: [11, 34, 35]

- The strong electric field bends the potential of the atom, allowing an electron to tunnel through the barrier.

- The electron is accelerated away from the ion by the laser field. As the oscillatory field reverses direction the electron is accelerated towards the atom and gains energy in the field

- The electron recombines with the atom, shedding its entire gained kinetic energy and the ionization energy in the form of a single high energy photon.

It should be noted that there is also a completely quantum mechanical description of this process which was published by Lewenstein et al. in 1994 [36]. It predicts spectra that are very similar to the semiclassical model and will not be discussed in detail here. Since the HHG process takes half the cycle period of the electric field and it happens during every half cycle with sufficient field strength we can see from the Fourier transform that the emitted harmonics are $2\omega_L$ apart in frequency, where $\omega_L$ denotes the central frequency of the driving laser. The typical nonlinear medium in our experiments is neon. It is an inversion symmetric medium and thus we only observe odd harmonics, since the even terms must vanish. The maximum energy of the plateau region is the cutoff energy $E_{\text{cut-off}}$, which is given by

$$
\begin{aligned}
E_{\text{cut-off}} &= I_p + 3.17 U_p \\
U_p &= \frac{e^2 E_L^2}{4 m \omega_L^2},
\end{aligned}
\tag{2.6}
$$

---

[2]Intense in this context means that the averaged energy over one field cycle, the ponderomotive energy, is larger than the ionization potential.

where $e$ and $m$ are the charge and the mass of the electron, respectively. The factor of 3.17 is the result of the semiclassical calculations in [11]. $U_p$ is the ponderomotive potential and $E_L$ is the electric laser field at its peak. Above this energy, the efficiency of the HHG process decreases exponentially with photon energy. The energy of the released photon depends on the exact ionization time and on the path it travels. There is an optimum for this time of birth and path for which the highest photon energies are reached [37].

Now suppose that we have a driving pulse like the one shown in 2.1b with $\Phi_{CE} = 0$. It is so short that there is an appreciable difference between the highest spike in the oscillatory field and the next highest one. Here the electrons which are being accelerated during the half cycle with the highest field strength will gather the most kinetic energy. They will lead to the release of the highest energy photons in the pulse. This is the process responsible for the emission in the cutoff. It is in principle simple to distinguish between the plateau and the cutoff regions in a measured spectrum since the cutoff region shows a much weaker modulation in the photon spectrum than the plateau (as shown in figure 2.3). The origin of the modulation is interference between photons produced during neighboring half-cycles – but since there is only one half cycle contributing to emission in the cutoff the modulation vanishes. A shorter driving pulse creates a broader cutoff as the range of energy that is only accessible to a single cycle of the field increases. Figure 2.3 shows a mock-up of a typical HHG spectrum. If we now use a combination of mirrors and filters that transmits only photons from the cutoff region we are left with an isolated pulse of attosecond duration[3].

Typically we employ a multilayer XUV mirror in the range of 90 eV to 145 eV with a bandwidth of 3 eV to 5 eV to focus the XUV light onto the sample [40, 41]. These optics provide a gauss shaped reflectivity at the target wavelength. Since the XUV spectral intensity decreases exponentially towards higher photon energies there is a lot more light at lower energies. Even if the mirror suppresses low energy photons they can still cause a stronger signal than the isolated pulse we are interested in. We put a metal filter with a transmission curve that opens up towards the higher energies that we are using in the beam. In this way we can suppress the unwanted photons at low XUV energies[4] in the XUV beam. The metal also suppresses the NIR driving pulse, which is of importance for the streaking experiments shown in chapter 5.

The emitted XUV light copropagates with the fundamental field due to phase matching in the medium. After careful alignment the two beams are concentric and the XUV mode shape is spherical. The mode shape is extremely sensitive to wavefront curvature. An analysis of the focus with a high resolution camera is not precise enough to make predictions about it[5]. The XUV mode is considerably smaller than the mode of the

---

[3]This is the most direct approach towards isolated attosecond pulses, but not the only one. Very short pulses have also been produced with other techniques like polarization gating [38] or relativistically oscillating mirror harmonics [39]

[4]Depending on the photon energy we use zirconium or palladium foils of 150 nm to 200 nm thickness.

[5]Common causes for the introduction of wavefront distortions are imperfectly glued vacuum windows or mirrors that are fastened too hard. By tightening the nylon tipped screws (<u>never</u> use pure steel screws) only very, very slightly this can be avoided.
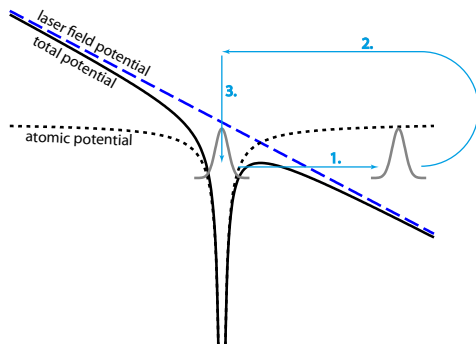
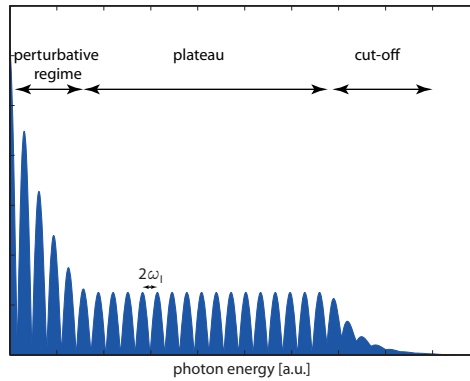Figure 2.2: Illustration of the three step model [37]



Figure 2.3: The spectrum of XUV photons generally produced by short and intense laser pulses

fundamental light. We use this property to spatially separate the beams (for the technical details see sections 2.2.2 and 2.2.2).

### 2.1.3 Streaking

As we have discussed in section 2.1.2 the HHG process leaves us with an attosecond XUV pulse which is copropagating and inherently temporally synchronized with the driving NIR pulse. It seems natural to make use of this fact by recombining both of them for an experiment [42, 43, 44]. The attosecond streaking technique that will be discussed here gets its name from the streak camera [45]. In this device the properties of an ultrashort light pulse in the picosecond range can be measured. First the short pulse creates an electron pulse by ionizing a target medium, then these electrons propagate through a rapidly varying electric field perpendicular to the propagation direction of the electrons (the streaking field) and their trajectory is affected by the field. Then the electrons are detected on a screen. From the spatial distribution of electrons on the screen one can deduce the pulse shape. Attosecond streaking is in principle very similar: the short pulse to be measured is the XUV pulse and the streaking field is provided by the NIR pulse. Due to the drastically higher field gradients achievable in an intense laser pulse compared to an electronic device like the streak camera the time resolution is pushed from the picosecond to the attosecond range.

Let us now assume that we are hitting a gaseous target with the XUV pulse. The central energy of such pulses typically lies in the range of 30 eV to 145 eV, which is above the ionization threshold for any non-exotic target material. So the attosecond pulse will produce photoelectrons within a very narrow time window given by the temporal profile of the pulse. We make the assumption that the electrons are shielded from the electric field of the driving laser prior to their ejection via the XUV pulse. When these electrons
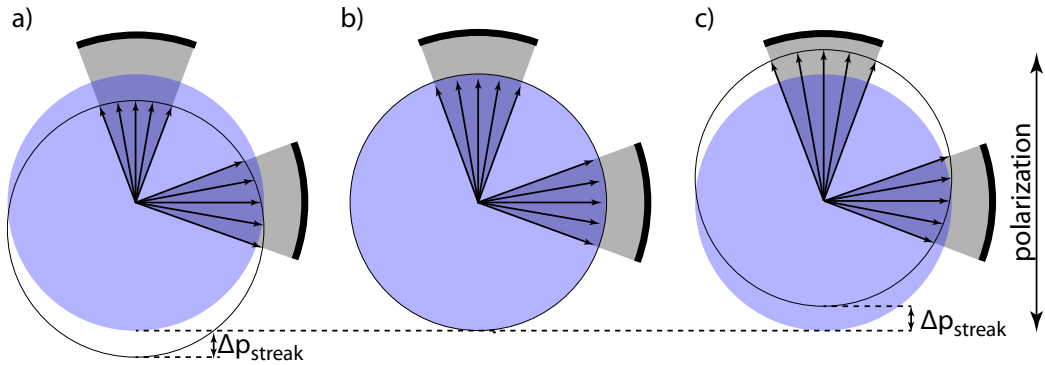
Figure 2.4: Illustration of the streaking process. The gray cones and thick black bars represent the collection angle and detectors. The blue circle denotes the unstreaked momentum distribution of photoelectrons released by the XUV pulse. **a)** is streaked away from the detector, **b)** is unstreaked and **c)** is streaked towards the detector. We are measuring the time of flight to the detector, from which we calculate the momentum of photoelectrons. In this diagram this corresponds to the length of the black vectors. As the streaking field acts upon the initially isotropic momentum distribution it adds a momentum vector $\Delta p_{\text{Streak}}$ in the polarization direction. When monitoring in this direction we see a modulation of the momentum towards lower (a, black vectors all contained in blue sphere) and higher (c, black vectors extend beyond blue sphere) values. In the direction perpendicular to the polarization both cases look identical: a broadening of the momentum distribution that extends to both higher and lower values – but much stronger to lower momenta. Adapted from [1].

are now released from the parent ions they feel the oscillatory field of the NIR pulse. We further make the assumption that the Coulomb field of the nucleus is negligible after ionization due to the large kinetic energy of the electron. For the remainder of this discussion we will only consider linearly polarized laser pulses and study all quantities on the polarization axis. Then the equation of motion (in atomic units $|e| = \hbar = m_e = 1$) is:

$$\ddot{x} = -E_L(t) \tag{2.7}$$

With $x$ being the position of the particle and $E_L$ the electric field of the NIR laser, the streaking field. The quantity commonly measured in streaking experiments is the time of flight of electrons to the detector, which can easily be mapped onto the kinetic energy and momentum. A particle that is exposed to the complete pulse of a laser does not retain a net momentum transfer after the pulse is gone. But if we vary the delay between NIR and XUV we can let the electron be released within the duration of the pulse – so it can receive a net momentum transfer from the part of the pulse that has not passed it yet. Mathematically speaking we integrate the equation of motion starting from $t_0$ to receive

$$\dot{x} = -\int_{t_0}^{t} E_L(\tau)\, d\tau$$
$$= v(t_0) + A_L(t) - A_L(t_0), \tag{2.8}$$

where $A_L$ is the vector potential of the NIR field. And since we measure the momentum long after the pulse is gone we set $t \to \infty$ and get

$$\dot{x} = v(t_0) - A_L(t_0) \tag{2.9}$$

The velocity $v_0$ is determined by the central energy of the ionizing XUV pulse. So we can see that attosecond streaking measures the vector potential of the light field [46]. For an intuitive picture explaining the measurement see figure 2.4. Here we illustrate the qualitative shape of measured streaking traces depending on the observation direction. In the polarization direction we can indeed claim that the trace follows the vector potential – in the orthogonal direction we see a different behavior. Here the individual spectra will be smeared out mostly towards lower momenta independent of the sign of the vector potential. We will refer to the streaking trace observed in the direction orthogonal to the polarization as transverse streaking. Its amplitude is proportional to the square of the field, so it changes more strongly with suppression/enhancement of the driving pulse.

Up to now we have implicitly made the assumption that the XUV pulse is so short in time that the NIR field does not vary at all over its duration. This is not really the case and we can use it to extract further information from the streaking data. Photoionization happens over the whole length of the XUV pulse with a probability given by the amplitude of the field (i.e. the envelope of the field). The initial kinetic energy of released electrons depends on the instantaneous frequency of the XUV pulse. Let us assume that the leading edge of the attosecond pulse has a lower frequency than the trailing one. When the temporal center of the XUV pulse is at a zero crossing of the vector potential with a

rising slope we can observe the following behaviour: the leading photoelectrons of lower kinetic energy would be accelerated while the trailing photoelectrons of higher kinetic energy would be decelerated. In total this would make the spectrum narrower. On the falling slope of the vector potential we would be able to observe the opposite: a broadening of the spectrum [47].

While a full derivation of the retrieval of XUV and NIR pulses will not be discussed here it shall be mentioned that this technique does not only measure the temporal evolution of the two pulses that interact with the electrons – the retrieved spectra also carry a signature of the transition matrix element from the medium to the free state and one could potentially use that to learn something about these matrix elements [48].

There are two typically used algorithms for the extraction of delay times from streaking spectrograms: the Center Of Energy (COE) method [20] and the approach relying on solving the Time Dependent Schrödinger Equation (TDSE). The algorithm for the COE method applies the following steps:

- subtract the background

- find the center of energy of the photoline for each delay step (either by a first moment analysis or a Gaussian fit to the spectrum)

- fit a streaking waveform of she shape

$$S(\tau) = S_0 e^{-4\ln 2((\tau + \Delta\tau)/\tau_L)^2} \sin(\omega_L(\tau + \Delta\tau) + \phi_{CE}) \tag{2.10}$$

  to the data.

Here $S_0, \tau_L$ and $\omega_L$ denote the streaking amplitude, pulse length and frequency of the NIR streaking laser respectively, $\phi_{CE}$ is the carrier envelope phase. The parameter $\Delta\tau$ is used when there is more than one photoline present, as will be discussed in chapter 5. This method yields no information about the temporal properties of the XUV pulse. The TDSE algorithm is more complex and reveals more physical parameters from the spectrogram. This calculation makes the assumption that the physics of XUV photoionization are well represented through the single active electron picture and first order perturbation theory. It also requires the transition dipole matrix elements to remain constant over the range of the experiment. This is the case when studying photoionization far away from resonances and with small relative bandwidths. For the modeling of the interaction with the laser field it is assumed that the final state kinetic energy of the photoelectron is much greater than the ionization potential of the neutral atom. Based on these prerequisites a transition matrix element is constructed that depends on the parameters of the NIR and XUV pulse. A first guess for the input values is made based on known attributes of the system such as the XUV mirror bandwidth or the NIR pulse length and central wavelength. Then the parameters are varied by a MATLAB program in order to find the best fit to the spectrogram. A more detailed description can be found in the Master's thesis of Ossiander [49], who wrote the retrieval software employed for the streaking experiments performed in this thesis.

## 2.1.4 Generation of Ultrashort UV Pulses

For now our toolbox contains intense and phaselocked near infrared pulses and very short XUV pulses. Now we will add another part of the spectrum: deep UV pulses.

We are again creating photons of higher energy from our NIR driving pulses. As we can see from equation 2.5 the polarization response of a medium to intense light pulses will contain terms that are proportional to the square, cube... of the impinging electric field. If we write the time dependent part of the field in the complex representation $E(t) \propto e^{i\omega t}$ we immediately see that this corresponds to terms with twice, three times... the frequency appearing

$$
\begin{aligned}
P =& \tilde{\epsilon}_0 \left( \chi^{(1)} E_L(t) + \chi^{(2)} E_L(t)^2 + \chi^{(3)} E_L(t)^3 + \dots \right) \\
=& \tilde{\epsilon}_0 \left( \chi^{(1)} e^{i\omega t} + \chi^{(2)} e^{i2\omega t} + \chi^{(3)} e^{i3\omega t} + \dots \right).
\end{aligned}
\tag{2.11}
$$

This is of course a simplification of the involved processes. There are many other phenomena that are associated with nonlinear optics that will not be mentioned here. For reference, see [33].

Within the perturbative regime the conversion efficiency for a second order process is much higher than for a higher order process. So one might be tempted to suggest second harmonic generation (SHG) as a means for ulstrashort pulse generation in the deep UV. There have indeed been very successful attempts at this endeavor, creating sub 10 fs pulses [50, 51]. But the very shortest pulses below 3 fs have been achieved with third harmonic generation (THG) [52]. The technical reason for this is that second harmonic generation is not possible in a gas. If we consider a medium with complete inversion symmetry, the even terms of the expansion must vanish for symmetry reasons. So for SHG we need a medium without inversion symmetry – a carefully selected solid. But in the UV range dispersion is much stronger than in the visible and increasingly harder to combat for shorter and shorter pulses. In addition the intensities that we would likely be using are above the damage threshold for most solids. So we are avoiding strong dispersion and damages by using a suitable medium: a gas, in our case neon.

In our case frequency tripling has another benefit: the central wavelength of our pulses translates to a third harmonic centered at 265 nm, which overlaps with the absorption bands of DNA and ozone, two very important compounds that could possibly be studied with our setup.

## 2.1.5 Measurement of Femtosecond Pulses: FROG

One of the biggest appeals of ultrafast science is also one of its standard problems: there is no measurement device in the laboratory that rivals the time resolution of the employed pulses. To characterize the pulses one typically has to use a replica of the pulse as a gating mechanism. This replica is delayed by $\tau$ and overlapped with the original in a nonlinear medium, which yields a spectrogram of the form:

$$
S(\omega, \tau) = \left| \int_{-\infty}^{\infty} E(t) g(t - \tau) e^{-i\omega t} dt \right|^2,
\tag{2.12}
$$

where $S(\omega, \tau)$ is the measured spectrogram, $E$ is the electric light field, $g(t - \tau)$ is the gate function and $\omega$ the angular frequency. In an actual measurement one would scan $\tau$ over the entire pulse length and record the transmitted spectrum for each step in $\tau$ with a spectrometer, giving the technique the name frequency resolved optical gating (FROG) [53, 54].

There are many different types of FROGs, but in the scope of this thesis we will only use two types: second harmonic (SHG) FROG and transient grating (TG) FROG. If the employed gating mechanism is second harmonic generation then the spectrogram takes the form:

$$S_{SHG}(\omega, \tau) \propto \left| \int_{-\infty}^{\infty} E(t)E(t - \tau)e^{-i\omega t}dt \right|^2 . \tag{2.13}$$

The generated signal is not at the same wavelength as the fundamental beam. As we are creating second harmonic radiation over the thickness of the nonlinear medium we have to ensure that the signal stays in phase and adds up contructively. This is given when the fundamental and second harmonic are traveling through the medium at the same phase velocity. In the presence of dispersion this is usually not fulfilled. But for birefringent crystals one can create the harmonic at the orthogonal polarization of the fundamental and then find an angle at which the refractive indices for fundamental in one polarization and signal in the other polarization match. This idea is called phase matching and it is typically the limiting factor for the spectral bandwidth (and hence the minimal pulse length) that can be measured with a SHG FROG.

The main advantage of TG versus SHG FROG is the fact that the signal is at the same wavelength as the fundamental. So it can be automatically phasematched and allows the measurement of the large spectral bandwidths that we need for our short pulses [55]. In a TG FROG the nonlinearity is of third order. One creates three beams with a mask with three holes that are located at the three corners of a square. Then one of the created beams is delayed with respect to the other two. When the two synchronous beams are focused into the nonlinear medium they create a time dependent modulation of the refractive index via the Kerr effect. The other beam is then diffracted off this grating and the first diffraction order is recorded as the signal. A TG FROG spectrogram has the form

$$S_{TG}(\omega, \tau) \propto \left| \int_{-\infty}^{\infty} E(t) \left| E(t - \tau) \right|^2 e^{-i\omega t}dt \right|^2 . \tag{2.14}$$

Once the $S(\omega, \tau)$ is measured, we need to retrieve the electric field from it. The electric field must be found by iteration: fit a waveform from an initial guess (e.g. the auto-correlation) to the spectrogram, check the mismatch to the data, improve the guess, repeat. The measurement is inherently heavily oversampled: $N \times N$ measured points for a retrieval of $N$ values for amplitude and phase respectively. This makes a convergence towards the real value quite likely.

## 2.2 Equipment

### 2.2.1 The Laser System: FP3

From the previous section 2.1 we learned that we need short, intense and CE phaselocked pulses for attosecond experiments. Our workhorse for this purpose is the FP3[6] laser system. A schematic overview of the setup is given in figure 2.5. In the following sections there will be a short description of the system. For more information see reference [56].

#### The Oscillator

The front-end of FP3 is a Kerr lens mode locked titanium doped sapphire (Ti:Sa) oscillator[7] which is pumped by a frequency doubled cw Nd:YVO$_4$ laser[8] which is usually used at $\approx 3.9$ W for our purposes. The oscillator produces $\approx 6$ fs pulses at a repetition rate of 80 MHz with an energy of $\approx 3$ nJ [57, 58]. After the oscillator the compressed pulses are focused into a periodically poled lithium niobate crystal which is optimized for difference frequency generation (DFG). The light spectrum will be broadened by self phase modulation- and the longer wavelength part of this broadened spectrum overlaps with the DFG signal [59]. In the spectral overlap there is a CE offset beat between the two waves at $f_{\mathrm{CEO}}$. This signal is used to provide feedback to the oscillator via a modulation of the pump power with an AOM in the so called fast loop. So we can see that the oscillator alone would already satisfy two of the criteria for our experiments: short and CE phaselocked pulses. But for efficient HHG we need at least five orders of magnitude more pulse energy.

#### The First Amplification Stage

In order to obtain higher energies we will employ the chirped pulse amplification scheme [60]. Here a light pulse is first stretched in a controlled way, then it is amplified and then it is recompressed. In this way one avoids damaging the gain medium with the high electric fields of a compressed and intense pulse. In order to stretch the pulse to 17 ps we let it pass twice through a 13.5 cm block of SF57 glass. Behind the glass block there is a pair of wedges the use of which will be explained later. The first amplification stage of the CPA is a nine-pass Ti:Sa crystal that is pumped with a 32 W 300 ns 532 nm laser. During operation the crystal is kept at a temperature of $\approx 178$ K. After the first four passes a Pockels cells acts as a pulse picker that reduces the repetition rate to 4 kHz. Instead of the Gauss filters that were used in previous setups FP3 uses a Dazzler[9] [61] to shape the spectrum and avoid gain narrowing. This versatile device can be used for much more

---

[6]FP stands for Femtopower, which is the commercially available CPA system from Femtolasers which forms the base of our setup. It was the third such system in the team and is thus called FP3.
[7]Femtolasers Rainbow
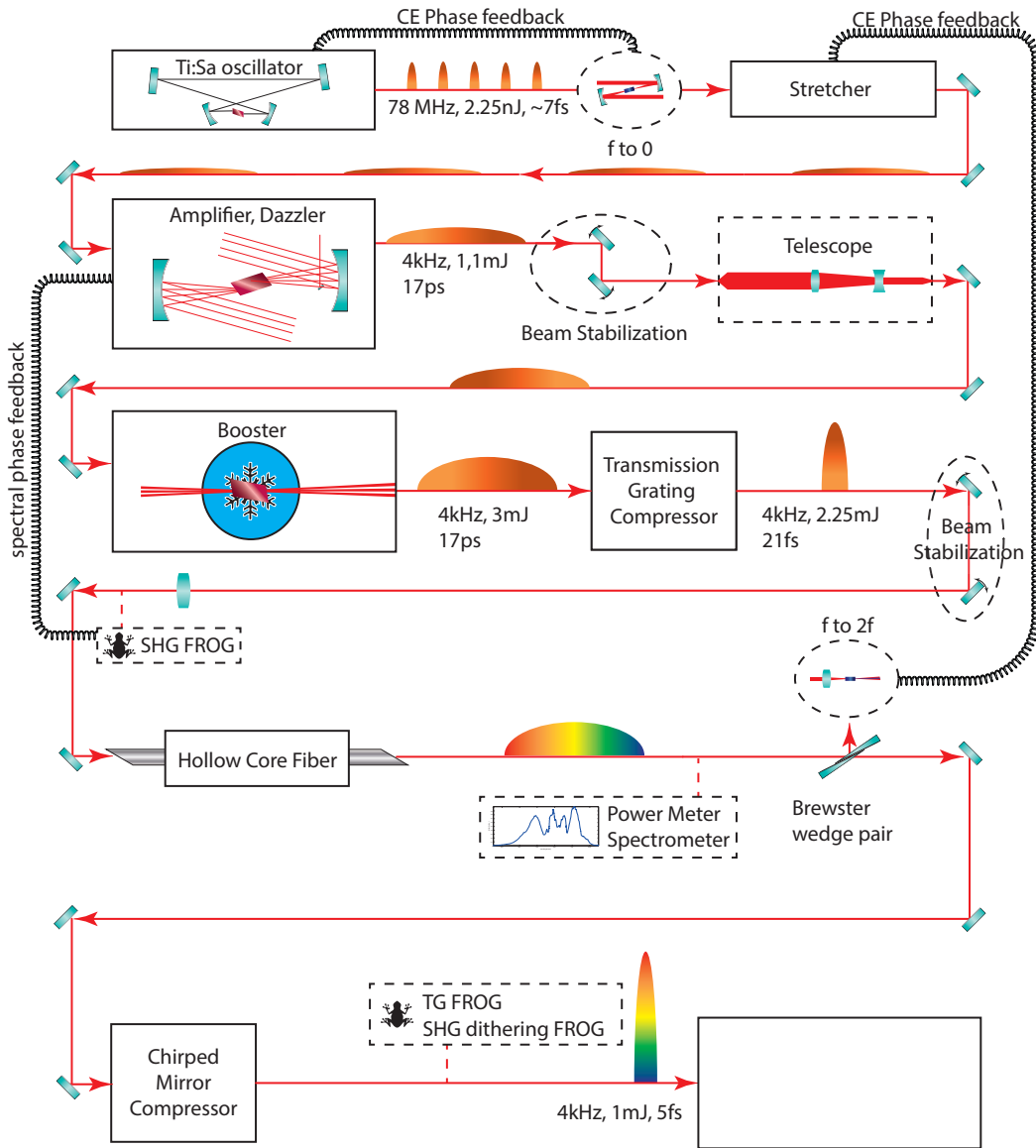[8]Coherent Verdi V6
[9]Produced by FASTLITE

Figure 2.5: The FP3 Laser Setup consisting of an oscillator, two amplification stages, a hollow core fiber and a chirped mirror compressor.

than just static filtering of the spectrum. It is capable of changing the spectral phase and even the CE phase. This allows one to fine tune the compression the output pulse of the CPA in a simple manner which will be discussed in more detail below. It also makes it possible to alternate the CE phase by a desired value (usually $\pi$) between two adjacent pulses. It will become apparent in section 4 why doing this can be beneficial for an experiment. Finally, after passing through the crystal for 5 more times the pulse is amplified to 1.05 mJ to 1.15 mJ. It is not necessary to have this stage running at the maximum possible power as long as one is able to extract the maximum usable power out of the second amplification stage.

**The Booster**

The second amplification (Booster) stage is also a Ti:Sa multipass system pumped by two mode-locked 532 nm pump lasers[10]. Apart from the general idea however, it differs significantly from the first stage in multiple respects. First of all it is only a three pass system that has a much lower amplification factor. The goal here is not to increase the energy by orders of magnitude but rather by roughly a factor of three. Secondly the crystal is cooled to the much lower temperature of 58 K. This reduces thermal lensing and thus improves the mode profile since the thermal conductivity of sapphire increases with decreasing temperature. Of course it also introduces the technical complications associated with a cryogenically cooled setup. Thirdly the focusing into the crystal is very loose in order to avoid damages to the crystal. In fact the focusing is so loose that the entire setup of the booster is within the Rayleigh range of one of the tree passes. This fact makes refocussing the beam into the crystal challenging. Intuitively one would assume that moving the focusing optic would also move the focus. But if the optic is placed within the Rayleigh range of the beam the position of a focusing optic changes almost nothing about the focus. Only the curvature of the optic has a significant impact. But unfortunately it is necessary to set two parameters when adjusting the focus: we have to match the focus size of the seed beam to the pump beam and we have to set the focus position inside the crystal. The solution to this conundrum is a telescope before the booster with which ce can precisely set the beam diameter and divergence. The correct combination of refocusing optics for each respective pass inside the booster with the correct seed beam parameters can only be found when running the system at full power because the thermal lens changes the divergence markedly. Despite these considerable difficulties during alignment the system is very user friendly once set up. Two position sensitive diodes that are spaced far apart are used to mark the beam path of the seed pulse. If the incoupling is done carefully in this manner it is possible to run the system for months without the need for any alignment of the booster stage. At this stage the pulse power reaches 2.5 mJ to 3 mJ.
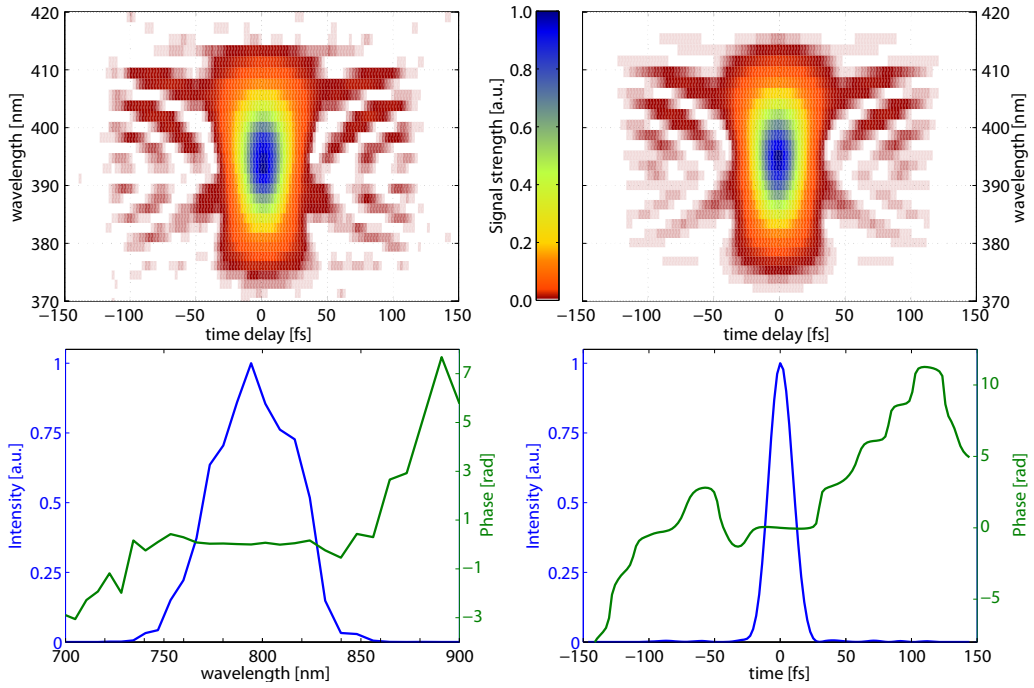
---

[10]Thales ETNA HP.

Figure 2.6: SHG FROG measurement and retrieved pulse in temporal and frequency space of the output of the booster after the transmission grating compressor (see figure 2.5). The retrieved pulse length is 21.5 fs, which is essentially Fourier limited.

**Recompression and Spectral Phase Feedback**

After recollimation the pulse is compressed in a transmission grating compressor with 86% transmission efficiency [62]. We are not using the same method for compression as for stretching and so we can expect not to compensate the higher order chirp. Here the dazzler comes into play again. There is a second harmonic FROG after the compressor that can be included in the beam path with a glass wedge on a flip mount. The spectral phase that is extracted from a measurement with this device can be subtracted from the previously applied phase in the dazzler. This does not necessarily result in a compressed pulse because there could be nonlinear effects on the way to the FROG that would change in addition to the applied phase feedback. But in that case one can simply iterate and repeat the phase measurement and the feedback cycle until the pulse is sufficiently compressed. Typically no more than three such iterations are necessary. A measurement of such a compressed pulse at this stage of the setup can be seen in figure 2.6. It shows the retrieval of a 21.5 fs pulse, which is almost identical with the Fourier limit.

**Supercontinuum Generation and Final Compression**

In order to obtain a few cycle pulse the spectrum is then broadened in a Neon filled hollow core fiber (HCF). The produced supercontinuum (see figure 2.7) stretches from 400 nm to 1100 nm. With harder focusing and a different fiber geometry it is also possible to broaden the spectrum further, but since the wavelength range that we can compress with the chirped mirrors on hand[11] ranges from 550 nm to 1100 nm the first step towards shorter pulses would be the extension of the chirped mirror range – not the spectrum. The broadened spectrum easily spans an octave and enables f-to-2f CE phase detection [63, 64]. The result of this measurement is fed back on a piezo motorized double prism in front of the amplifier stage for CE phase stabilization. This is the slow loop complementing the fast loop inside the oscillator.

The compression for the higher energy system does not simply follow the same procedure as for the one stage amplifier. Due to the higher pulse energy we see filamentation at the exit of the hollow core fiber, which changes the beam profile and potentially the temporal profile – especially because it keeps the beam profile very compact as it propagates through the exit window of the fiber tube. There could be nonlinear effects in this window that we cannot easily prevent. In the near future a double sided differentially pumped fiber will be installed. The much lower gas pressure at in and outlet will prevent filamentation and improve the beam profile.

**Measuring the Compressed Supercontinuum:**
**Transient grating and external dithering FROG**

To check the compression after supercontinuum generation a TG-FROG is in use. While the trivial phase matching condition of the TG process means that TG-FROG is in prin-

---

[11]*PC5*, for specifications see http://www.ultrafast-innovations.com/index.php/database/article/174-pc5
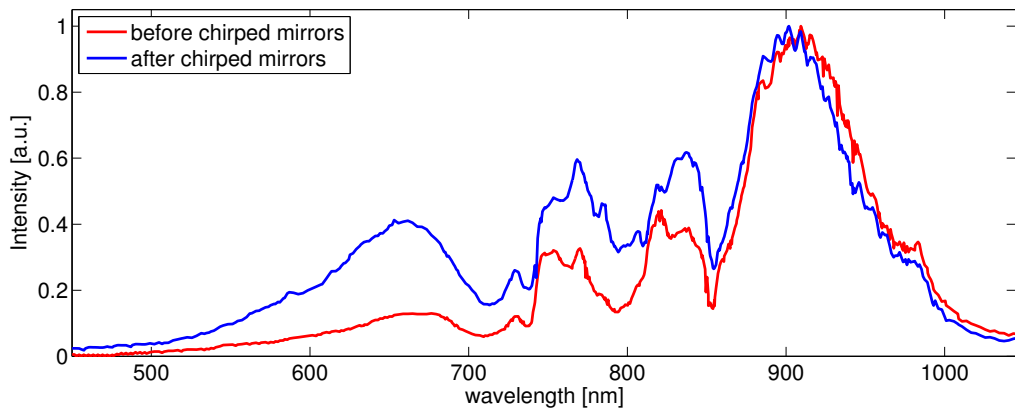
Figure 2.7: Comparison of supercontinuum spectra created at 1.2 bar in the hollow core fiber before and after compression via chirped mirrors. It is evident that these specific mirrors cut the blue part of the spectrum up to 850 nm. This reduces the bandwidth and lengthens the minimally achievable pulse duration.

ciple able to measure extremely broad spectra the strong alignment dependence of the measurements makes it difficult to use. This diagnostic is not in use everyday and so it is usually necessary to realign it completely once it does get used. There is no direct way to judge whether a trace is correctly showing an uncompressed pulse or whether the FROG itself is not well aligned[12]. A typical measurement yields a pulse duration of 5.5 fs for optimum compression. The currently achievable pulse duration is not as short as one could expect, given the sub–4 fs performance of similar one stage amplifier systems [65]. But for many experiments, notably the delay measurements performed for this thesis (see section 5) it is absolutely short enough.

In a SHG FROG the situation is easier. Not only is it simpler to align in the first place, but also there is one criterion that allows one to judge the alignment of the interferometer in one glance: the trace has to be symmetric. Unfortunately the large bandwidth of the supercontinuum makes a SHG measurement difficult. One can either use a thick nonlinear crystal (and lose phasematching bandwidth) or a very thin crystal (and lose a large part of the signal). A possible solution is provided by the dithering method [66]. Here the crystal is swiftly rotated during the acquisition of a single delay step in a FROG measurement. This leads to a different central phasematched wavelength for each rotation angle. Since the rotation is performed faster than the acquisition the result is an average over the entire phasematching range. For a thick crystal with a precisely defined phasematched frequency this amounts to scanning a delta-like function over the spectrum and then adding up all the frequencies (for each delay step). In this manner it is possible to greatly increase the bandwidth of a thick crystal. For few cycle pulses this remains

---

[12]There is an indirect way: put some material of known dispersion in the beam, measure with and without this material and then check if the material dispersion is reproduced correctly.

challenging – if one decides to use a thick crystal the pulse is changed significantly by the medium. And for a thin crystal it is essential to place the rotation axis inside the crystal without shifting it through the focus. Of course the thinner the crystal, the more precise the rotation axis has to be placed. With our pulse parameters we would have to use a $100\,\mu m$ to $200\,\mu m$ thin crystal, making the alignment very difficult. This is why we chose to circumvent this dilemma by modifying the angle of the incoming beam with motorized mirrors instead of the crystal. With a camera in place of the crystal the alignment during the dithering process can be verified and it can be ensured that the focus does not shift significantly, then the camera is replaced by a BBO crystal. Of course this only delays the precise alignment problem to a later point: coupling into the spectrometer. But this can again be remedied by using scattering elements like a cosine corrector. First measurements with the External Dithering SHG FROG have been carried out and look very promising [67].

### Stability

Figure 2.8 shows how stable the laser system is currently running. The traces that are shown here have been recorded in a streaking measurement which has been evaluated with the COE method. It is apparent that the laser system produces extremely similar pulses over an extended period of at least 4.5 h. It has to be mentioned that this was in principle also possible with older systems. The very first streaking measurement in 2001 took 8 h [1], which proves that the waveforms were stable at least this long. But for these measurements the laser performance was so volatile that experiments were only possible at night when the laboratory was quiet. Now we are able to provide a solid laser performance frequently, even while the lab is busy. The stability shown here is now actually the routine performance.

## 2.2.2 The Surface Science Beamline: AS3

When one has succeeded in producing a few femtosecond pulse it must be sent into vacuum quite soon because air dispersion is strong enough to have an impact on the pulse length. So directly after the chirped mirror compressor there is a fused silica Brewster window that seals an entry port to vacuum. Then the beam is guided to the beamline of choice. In this thesis two of these setups were used, each with its own unique capabilities. The first one we will discuss here is the surface science beamline, AS3 [68]. Ultra high vacuum conditions are imperative for performing surface science experiments on many materials. However, for HHG one needs a gas target with pressures on the range of 200 mbar. So one of the main tasks of the AS3 beamline is to work as a differential pumping setup that can provide the pressure gradient from 200 mbar to $5 \times 10^{-11}$ mbar. An overview of the first vacuum chambers is shown in figure 2.9. The beam enters from the right side. It is focused into a quasi static gas cell to produce high harmonics. The intensity is regulated with an iris diaphragm (A1). Directly behind the HHG target there is a skimmer (S, a conical piece of metal with a small hole at the converging side).
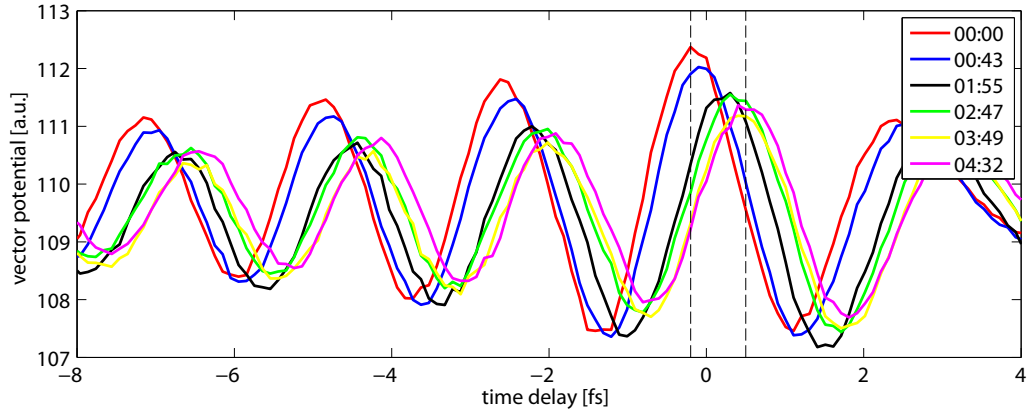
(a) COE retrieved data, time passed since the first acquisition is shown in the legend.
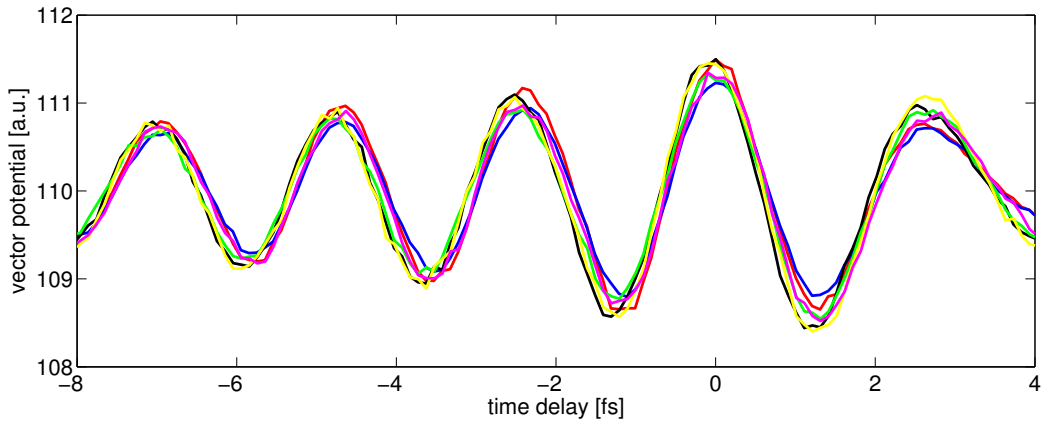


(b) COE retrieved data, time shifted and normalized

Figure 2.8: Center of energy retrieved streaking traces that were recorded in AS3 on clean tungsten over an extended time period. The shift of 0.7 fs in time is meaningless for most experiments and can be explained by slow pointing or temperature drifts in the beamline before high harmonic generation. It corresponds to a drift of only 200 nm. Normalizing the graphs is justified because the streaking intensity can and does change with the alignment of the overlap on the target. It does not necessarily mean that the actual intensity output of the laser changes. If it were to change we would see a change in the intensity of the produced harmonics, which is not the case. Over the timescale of a minute the harmonics intensity has a root mean square fluctuation of 1 %. It is evident that the laser system is capable of producing essentially identical waveforms over a period of at least 4.5 h.
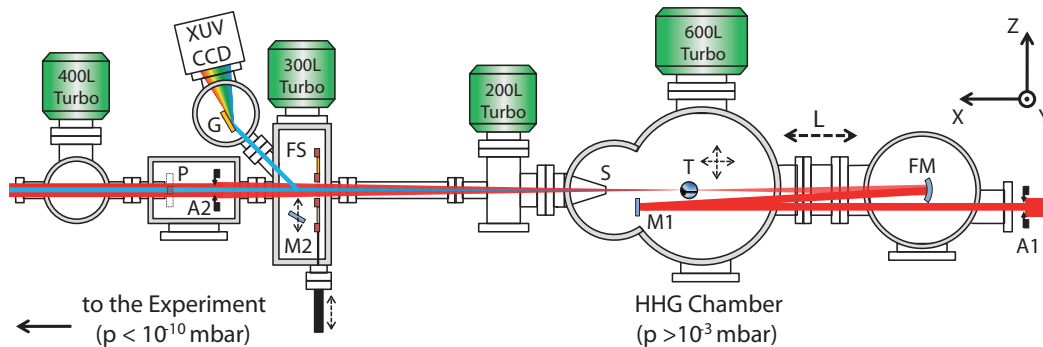
Figure 2.9: AS3 beamline (adapted from [69]). S: Skimmer, FM: focusing mirror, FS: filter slider, A1: iris aperture for HHG optimization, A1: iris aperture for streaking optimization,P:pellicle, G:grating

Over the length of the beamline there are repeated apertures and pumps to reduce the pressure.

Behind the experimental chamber (see figure 2.10) there is a multichannel plate (MCP) combined with a phosphorus screen which is monitored with a CCD camera. With the help of appropriate metal filters in the filter slider (FS) it is used to characterize and optimize the harmonic flux. For further diagnosis the XUV spectrum can be scrutinized with a spectrometer (read: a concave grating and a XUV CCD camera) which can be put in the beam path with the help of a movable mirror(M2).

In the surface science end station we have access to a number of sample preparation tools:

- A load lock to keep the main chamber clean when exchanging samples

- A sputter gun for sample cleaning

- A heating and cooling setup with which the sample temperature can be varied from 30 K to 2400 K

- Two types of Knudsen evaporation cells – one for metals (see [22]) and one for organic molecules[13]

- A Low Energy Electron Diffraction (LEED) device for structural analysis of surfaces

With a freshly prepared surface we can move the sample over to the experimental chamber and analyze it by performing X-ray Photoelectron Spectroscopy (XPS) [70]. As a light source for this technique we have a cw X-ray source with an aluminum cathode at 1486 eV and a magnesium cathode that emits at 1253 eV. The high photon energy makes it possible to reach a large number of core states that cannot be accessed with our XUV pulses. The typical flux rates are also significantly higher and the energy resolution is

---
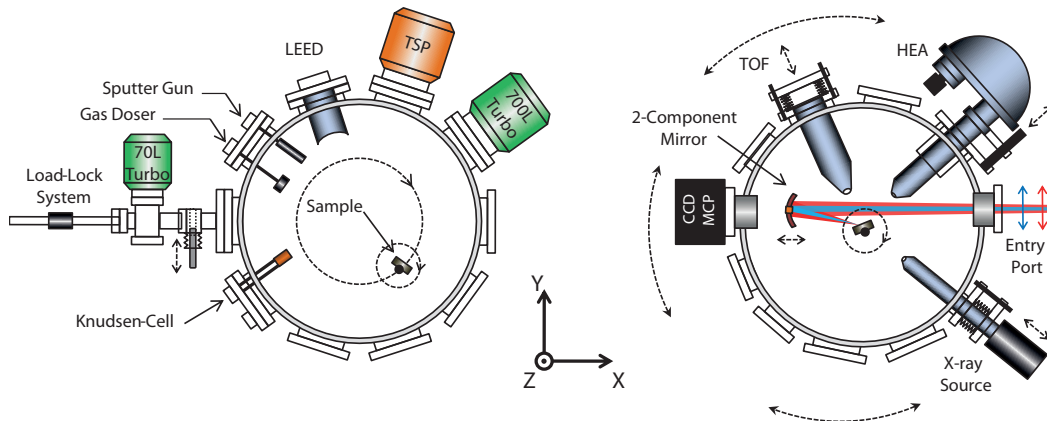
[13]A 4-cell evaporator by Dodecon

Figure 2.10: AS3 sample preparation (left) and experimental (right) chamber with surface science tools (adapted from [69]). The pressure in both these chambers is kept below $10^{-10}$ mbar. The chambers are explained in more detail in section 2.2.2.

much better than in attosecond experiments. With XPS one can obtain characteristic spectra from a sample, check these spectra against tabulated values [71] and identify the present atomic species. We use a hemispherical analyzer (HEA) for the detection of photoelectrons. For the measurement of XUV/NIR produced photoelectrons we employ an electron time-of-flight detector (TOF).

In order to create a time delay between the copropagating XUV and NIR beams we separate them from each other. In AS3 this is performed with a pellicle[14] with a thin metal filter in the center. The metal filter transmits high energy XUV light but blocks NIR light and low energy XUV light [72, 73]. The pellicle is transparent to the NIR beam. After passing the pellicle the two beams hit a concentrically split mirror. The inner mirror is a specially coated XUV multilayer optic which is mounted on a piezo actuator. This actuator creates the time delay between the pulses. The outer mirror is a partially reflecting metal mirror[15]. Both optics are cut from the same substrate and focus the beam onto the sample surface. In the two dimensional drawing it is not apparent that in order to bring the beam from the MCP used for optimization to the split mirror used for the experiment we can rotate the vacuum chamber around the axis labelled as $y$ in the figure. For more information about this beamline see references [74, 68]

---

[14]A 2 µm thin nitrocellulose membrane

[15]It is experimentally easier to set the correct NIR intensity for the experiment if the mirror is only partially reflective because this means that a change in iris opening translates to a smaller change in intensity on the sample.
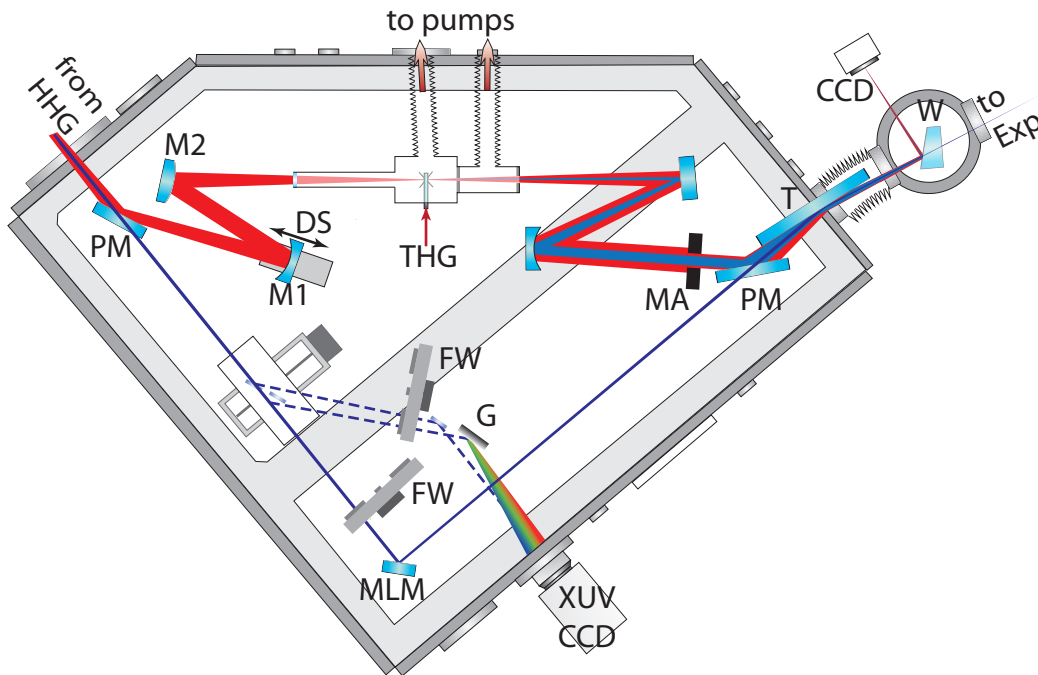
Figure 2.11: The delay chamber of AS2 (adapted from [76]). PM: perforated mirror, DS: delay stage, THG: third harmonic generation, MA: motorized aperture, FW: filter wheel, MLM: multilayer XUV mirror, XUC CCD: XUV compatible CCD camera, T: toroidal mirror, W: glass wedge, CCD: UV/NIR CCD camera

### 2.2.3 The Interferometric Beamline: AS2

In the previous section we presented a beamline with a highly sophisticated experimental end station. For the AS2 beamline the unique capabilities lie in a part that is realized with just a split mirror in AS3: the delay chamber (see figure 2.11) [75].

As in other beamlines we first generate high harmonics with NIR light in a separate chamber[16]. Then we need to spatially separate the two beams. Here the role of the pellicle is played by a perforated mirror (PM). The smaller XUV mode will pass through the hole in the mirror while a donut shaped NIR beam will be reflected. In the XUV beam path we find very similar diagnostics to the AS3: an XUV CCD that can either be used for direct observation of the beam profile (fulfilling the role of the MCP) or as a spectrometer. Here we also have the possibility to use different metal filters which can rapidly be switched through the use of filter wheels (FW). The XUV beam is reflected on a multilayer mirror (MLM) and recombined with the NIR at the second perforated mirror. They then both get focused by a Nickel coated grazing incidence toroidal mirror

---

[16]Not drawn here – it mainly consists of a focusing mirror and a quasi static gas cell
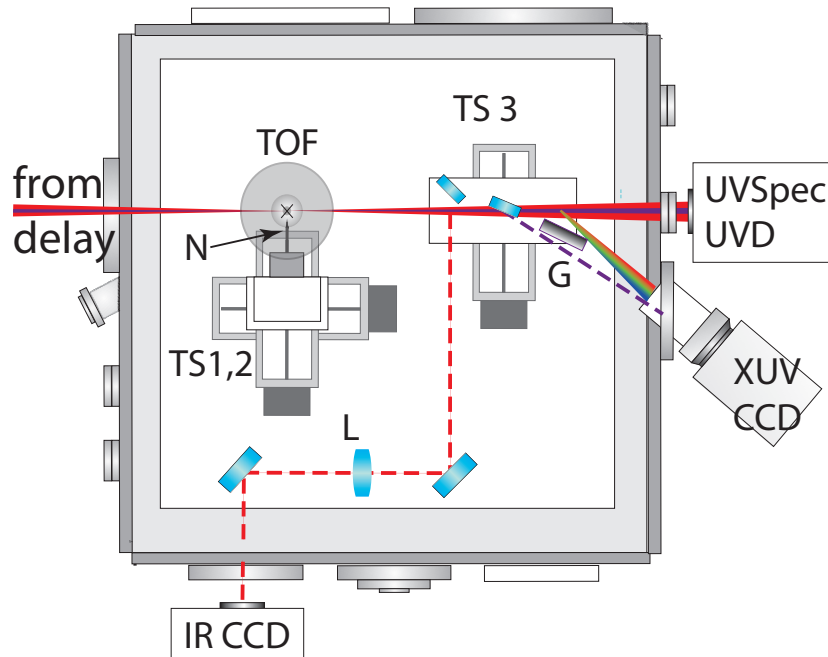
Figure 2.12: The experimental chamber of AS2, including translation stages (TS1,2) for positioning the nozzle (N) and guiding the beam to various diagnostics (TS3). Diagnostics include an XUV CCD camera for beam profile and pointing analysis, a XUV spectrometer with an imaging grating (G) and an IR CCD camera for the overlap alignment in collinear operation of the beamline. It is also possible to let the beam pass through unhindered and send it to a UV diode and a UV spectrometer for analysis of the THG light (adapted from [76]).

at the exit of the delay chamber.

The huge advantage of this design is the amount of freedom one gains in the NIR arm of the interferometer. Now it is possible to manipulate the beam after HHG, which is very challenging in a collinear setup. By choosing the radii of curvature of the mirror M1 and M2 accordingly one can refocus the light in the NIR arm and generate high intensities. Here one can use the short pulses for third harmonic generation – or one can place a sample in the beam path and analyze the transmitted field by streaking.

The experimental chamber of AS2 is shown in figure 2.12. It contains beam diagnostics for both XUV, NIR and UV light to characterize beam shape, position and spectrum of all three beams. It also houses a TOF detector and a gas nozzle for streaking experiments.

# Chapter 3

# Molecules in the Gas Phase: UV/XUV Pump Probe Experiments in Ozone

As outlined in chapter 1 we are exploring the first few femtoseconds of charge rearrangement in ozone triggered by intense deep UV light. We argue that the product of the subsequent molecular decay are determined by the electronic motion driving the nuclear dynamics. This is a replica of the photophysics in the stratosphere, where ozone absorbs harmful UV radiation.

## 3.1 Principle of the Experiment

We perform pump probe photoelectron spectroscopy on pure ozone gas. The sample is excited via an ultrashort NIR pulse at $1.5\,\text{eV}$ or a UV pulse at $4.5\,\text{eV}$. Upon excitation a part of the illuminated molecules will be lifted to the excited state. The valence electrons in this state are less tightly bound than those in the ground state. The molecules will then be ionized by an XUV pulse at $130\,\text{eV}$. This releases a photoelectron which we analyze with our time of flight detector (TOF). From the time of flight and the photon energy we can calculate the kinetic and binding energy of the electrons and distinguish between ground and excited state. In figure 3.1 the spectra of the fundamental laser beam, the frequency tripled UV and the absorption spectrum of ozone are shown. Evidently the spectral overlap is especially good in the Hartley band, where the cross section is also exceptionally high. Due to the high energy that is available to us in the NIR it seems like pump probe experiments might be possible even with all three pulses combined: NIR, UV and XUV. In this case there could be quantum beats between the populations of the Hartley and Chappuis and Wulf: the two excited states are simultaneously and coherently populated – so they can form a wavepacket that evolves in time and the population swaps back and forth between them. We will address the experimental feasibility of this in section 3.4.

### 3.1.1 Time Resolution versus Energy Resolution: The Choice of XUV Mirror

Attosecond photoelectron spectroscopy on molecules faces a fundamental conundrum. In these experiments we would like a high time resolution to track the evolution of the system – but we also need an appreciable energy resolution to resolve the signals. And in
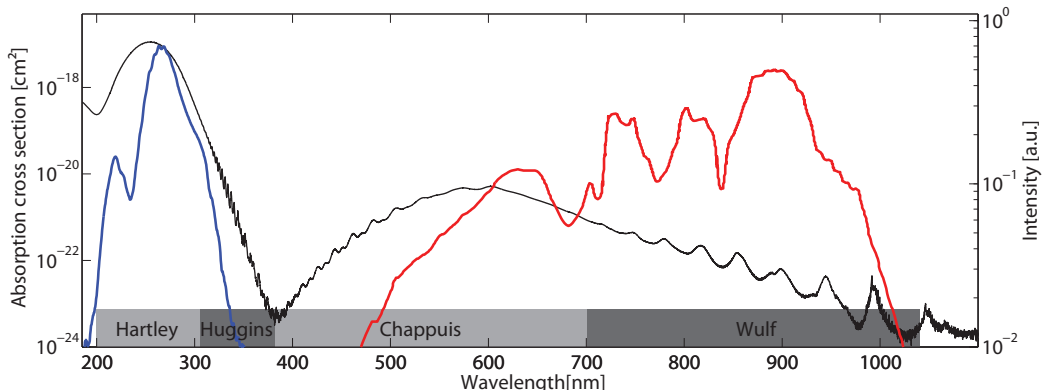
Figure 3.1: The absorption spectrum of ozone (black, referring to scale on left side of figure), the compressed spectrum of the FP3 laser system (red) and the frequency tripled spectrum (blue). Both spectra have been normalized individually. The UV pulses spectrally overlap completely with the Hartley band. In the near infrared there is still some overlap with the Chappuis band. This UV spectrum was produced at 8 bar backing pressure in the THG target. [77, 78, 79]

attosecond photoelectron spectroscopy both of these are chiefly determined by the same property: the bandwidth of the ionizing XUV pulse. For a gauss shaped spectrum the time bandwidth product is given by

$$\Delta\nu \cdot \Delta\tau = \frac{2\ln 2}{\pi}, \qquad (3.1)$$

$$\Delta E \cdot \Delta\tau = 1825 [\text{eV}][\text{as}], \qquad (3.2)$$

where the $\Delta$ denotes the full width at half maximum of the frequency $\nu$, the energy $E$ and the time $\tau$ respectively. Since we are mainly interested in dynamics triggered by the UV pulse at 4.5 eV and we need to be able to separate ground and excited state spectrally we chose a mirror with a bandwidth of 3.5 eV. This yields a temporal resolution of 520 as for a compressed pulse.

## 3.2 Sample Preparation: Ozone Distillation

When performing experiments with ozone there is always the danger of contaminating the sample with oxygen since ozone is metastable and naturally decays into oxygen. In our case we would not see any dynamics in oxygen since its absorption cross section is negligible in the spectral range of interest [78]. But we would still produce photoelectrons from oxygen, generating a background and making the actual signal harder to detect. So we need purified ozone. In order to judge the implications of this fact let us delve into the research of the 1950s. During this time ozone was studied not for its atmospheric
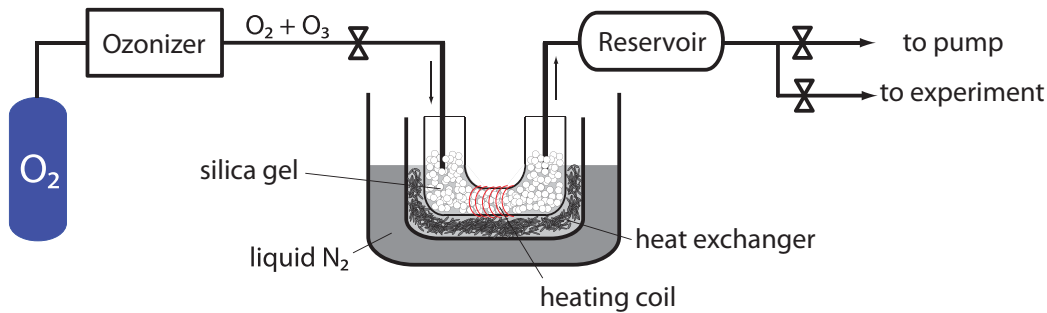
Figure 3.2: The distillation setup for delivery of pure ($> 95\%$) ozone to vacuum. After the ozonizer all pipes are made from stainless steel. The U-shaped pipe containing silica gel is made out of glass. In front of the pump there is a catalyst (Carulite 200) that turns the ozone to oxygen and thus protects the pump.

properties but because of its considerable oxidation potential and possible use as rocket fuel [80]. Unfortunately it turned out be unusable not for lack of contained chemical energy but due to its extreme instability [81]. Ozone explodes violently when triggered by vibrations, high temperature, sparks, organic contamination or light. It is also highly corrosive and toxic. Concentrated ozone can only be handled in containers made of nonreactive materials such as Teflon, stainless steel or silica. The parts of our setup that come into contact with purified ozone are built exclusively out of these materials.

In order to obtain pure ozone we proceed in the following way (see also figure 3.2):

- produce low concentration of ozone from oxygen in a gas discharge[1]

- Let $O_2/O_3$ mixture at 600 mbar flow through a cold trap at $-90\,°C$ filled with silica gel beads

- The silica gel passivates the $O_2$ similar to the sawdust that passivates nitroglycerin in dynamite[2]

- The higher vapor pressure [82, 83] and smaller surface area of $O_2$ compared to $O_3$ make sure that ozone adsorbs to the silica gel while oxygen does not [84]

- Pump the setup down to a few mbar to dispose of remaining gaseous oxygen

- increase the temperature of the glass tube to $-25\,°C$ with a heating coil until the pressure in the reservoir reaches 150 mbar to 200 mbar

This procedure leaves us with concentrated ozone. In order to measure the concentration we measure the pressure in the reservoir, shut it off from the rest of the setup and heat

---

[1]Commercially available product: Sander Labor– Ozonisator 301.19
[2]Explosions of adsorbed $O_3$ can still happen, but they are much less likely

it up to $130\,°C$. At any appreciable concentration this leads to an explosion. According to

$$2O_3 \rightarrow 3O_2 \tag{3.3}$$

for a formerly pure sample of ozone the pressure would increase by a factor of 1.5 (after cooling down to the temperature at the start of the procedure). In the presence of impurities and the residual pressure of oxygen $p_0$ when pumping down after adsorption we see a somewhat smaller pressure increase from $p_s$ to $p_e$. Assuming an ideal gas and constant volume we get the ozone concentration

$$C(O_3) = 2\frac{p_e - p_s}{p_s - p_0} \tag{3.4}$$

Note that here we are calculating the concentration of ozone in the gas that was desorbed from silica gel, not in the total amount of gas. It makes sense to consider this quantity because we will be constantly taking gas out of the volume and replenishing it through desorption. So the purity of the replenishing gas is the quantity of interest.

We typically reach purities of 95 % (in the total gas after desorption) and 99 % (in the desorbing gas). After two and a half hours of continuous desorption the concentration is still 95 %, which is sufficient for our experiments[3].

## 3.3 UV Generation and IR Suppression

### 3.3.1 UV Generation

As we have argued in section 2.1.4 our method of choice for ultrashort pulse generation is frequency tripling in a gas. The high pulse energy that we are using dictates a medium with a very high ionization threshold: Neon. Even if Argon or $SF_6$ have higher nonlinearities strong ionization leads to saturation and limits the maximum yield from these gases [85]. Since we are forced to use a medium with a low yield per atom we have to make sure that we have the maximum possible amount of atoms in the beam and use high pressures. The quasistatic gas cells that we were using in the beginning are simply stainless steel tubes with two small holes for laser entry and exit and a gas feed line. We predrilled the holes with diameters of $300\,\mu m$. But after one to three days of usage the targets are worn out (see figure 3.3) and damaged by the intense laser. This widens the holes, prevents pressure buildup inside the target and dramatically decreases the UV yield. It also produces a more painful problem: the ablated material is deposited not only in the differential pumping chamber but also on the first mirror after the target, which effectively destroys it. Targets made out of aluminum ceramics are a more durable alternative to steel. They are virtually indestructible by our laser[4]. Target preparation is more difficult since these ceramics are harder than the standard drill bits, but it is still

---

[3]The longevity of our ozone did improve over months. We assume that the ongoing passivation of the setup walls due to ozone exposure is responsible.

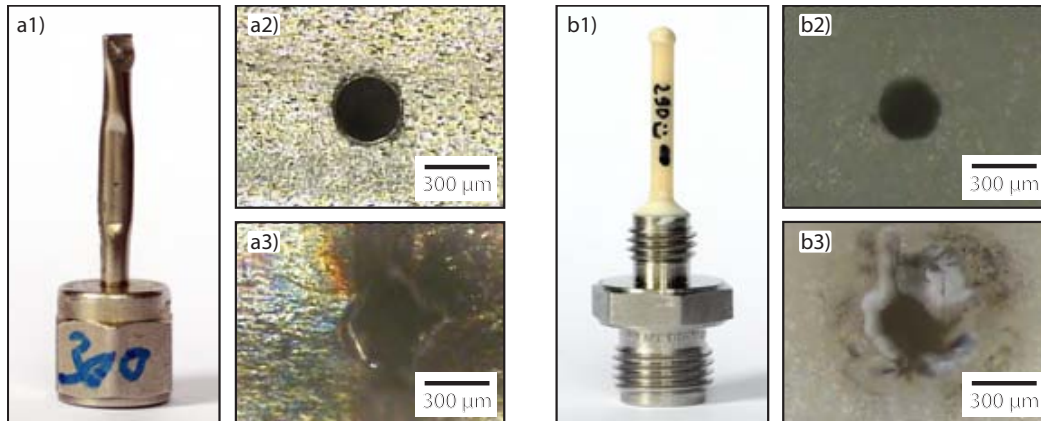[4]This assumption was experimentally thoroughly tested.

Figure 3.3: The different types of targets used for UV generation. **a)** shows the previously prevalent predrilled steel targets. In **a2)** an unused target is shown, contrasting with **a3)**, a used target. It is apparent that the hole is elliptic and considerably widened in the vertical. This would in practice reduce the UV flux. **b)** shows the ceramics targets with **b1)** being an unused target and **b2)** a used one. Also here strong wear is visible, but the central hole is still almost intact. This target was used daily for several weeks. During the alignment we were less careful about damaging the target with the full beam than with a steel target and could perform UV flux optimizations significantly faster.

possible. Either one can send the targets to a company that employs $CO_2$ laser drilling[5] or one can drill the holes with a high power disc laser available in house [86].

While the target is running the Neon flow is substantial. At a backing pressure of 9 bar we are using $16\,000\,\frac{\mathrm{N\,L}}{\mathrm{h}}$ or $16\,\frac{\%}{\mathrm{h}}$ of a 50 L gas bottle at 200 bar. Keeping in mind that this gas flow occurs inside the interferometer of the delay chamber we need to take precautions to keep the mechanical stability of the setup high enough to perform streaking measurements. The pump[6] for the first differential pumping stage (directly at the gas target, see figures 2.11, 3.4) is decoupled from the chamber through a helix stabilized pressure hose[7]. Additionally it is suspended from the laboratory ceiling. The second stage consists of another screw pump that is placed far away in a separate room[8]. While the target is running at 9 bar backing pressure the delay chamber is maintained at $6 \times 10^{-3}$ mbar. The experimental chamber is separated from the delay chamber by a plate with an aperture of 4 mm. Thanks to this additional barrier the background pressure here is not affected by the THG target. With this setup we can produce up to 7 µJ of deep UV pulses, which is also shown in figure 3.5.

---

[5]We used *LiLa Laser*

[6]A *Busch Cobra* screw pump

[7]These hoses may look crude in a high vacuum setup, but they provided a supreme vibrational decoupling – much better than the membrane bellows previously used for the same purpose.
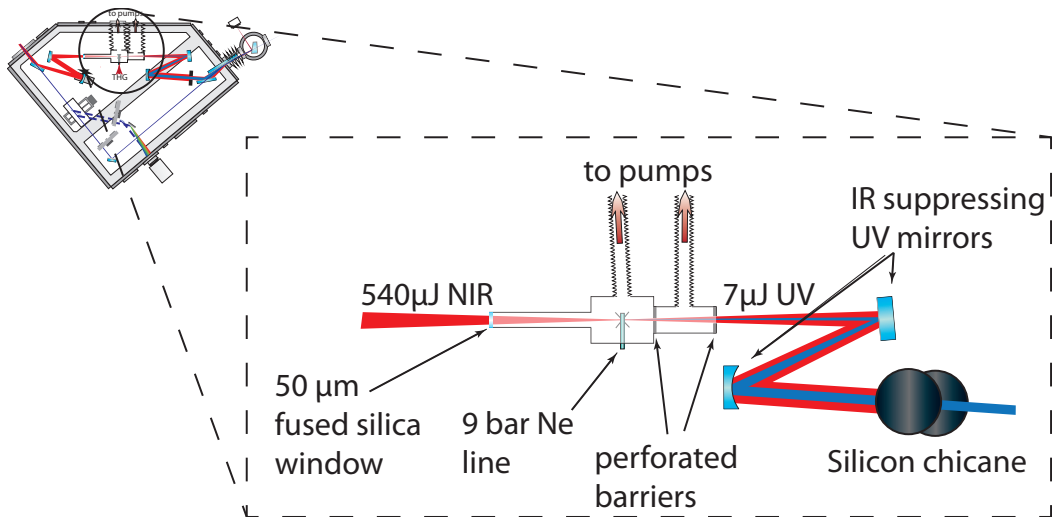
[8]*Leybold Screwline*

Figure 3.4: Cutout of the delay chamber of AS2 (figure 2.11). Neon is put into the chamber at up to 11 bar backing pressure. The target is motorized and can be positioned independent of the surrounding pumping stage. The differential pumping stages are separated from the main chamber by a 50 µm thin fused silica window and two perforated barriers. The IR suppressing mirrors and the silicon chicane are optional and are discussed in section 3.3.2. The silicon mirrors are used at Brewster's angle and have to be placed such that they reflect the beam up- or downwards due to the s-polarized field.
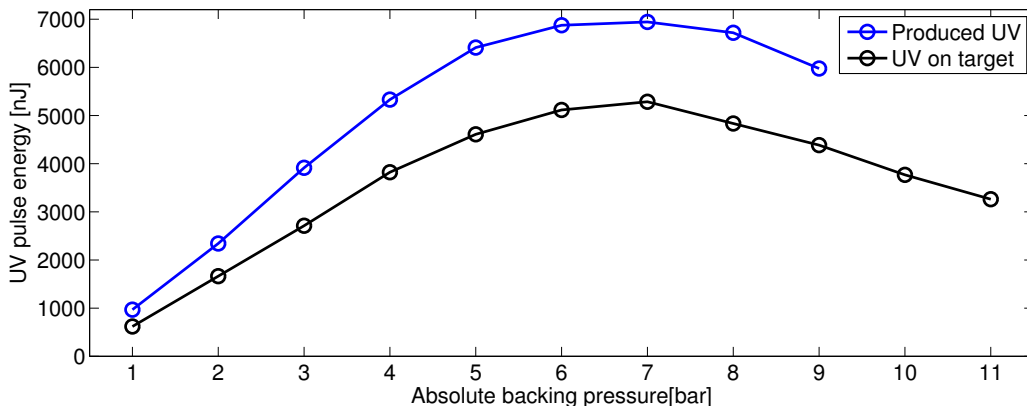
Figure 3.5: produced UV power vs backing pressure in gas target. Acquired with a ceramics target. The difference between the produced power and the one on target is caused by the optics that transport the beam to the experimental focus: three Aluminum mirrors and the Nickel coated toroidal mirror.

As one can see in section 2.2.3 the role of beamsplitters in our interferometer is performed by perforated mirrors. At the first mirror we use the fact that the high harmonic beam has a smaller wavelength than the fundamental and a smaller divergence. So it passes through the hole. The same holds true for the second perforated mirror – but here it is not a desired property. If we align the interferometer such that the beams copropagate after the second perforated mirror we lose 75 % of the UV power at this mirror. We have the option to align the beams such that they do not propagate collinearly but cross at the focus. This makes sure that we lose almost no energy on the way to the target[9]. But it severely complicates the alignment process of the spatial overlap. In a collinear setup we guide the beam out of the vacuum chamber with either an imaging system or a pick–off mirror. Outside of vacuum there is a UV compatible camera on which we detect both the IR beam going through the XUV arm and the UV beam and superimpose them. But if the beams are no longer collinear and they are passing through a window they get displaced differently (see figure 3.7 for an illustration). If we align them outside of vacuum then they generally do not overlap on target. In figure 3.6 one can see that the focus diameter (FWHM) is as small as $50 \times 70\,\mu$m, so the alignment precision necessary for maximum pumping efficiency is on the order of $10\,\mu$m. We overcome this with an alignment help that is very similar to our THG targets: a piece of ceramics with a $80\,\mu$m hole drilled by a high power disc laser. The alignment tool is positioned such that the transmission of the XUV beam is maximized on the XUV CCD. Then the UV beam is aligned on top of it with the motorized second perforated mirror. With this method we can transfer a large portion of the generated power to the sample. Assuming an almost

---

[9]Some losses are unavoidable since we have to use metal mirrors to avoid adding dispersion. That forces us to use Aluminum mirrors with a reflectivity of ca. 85 %
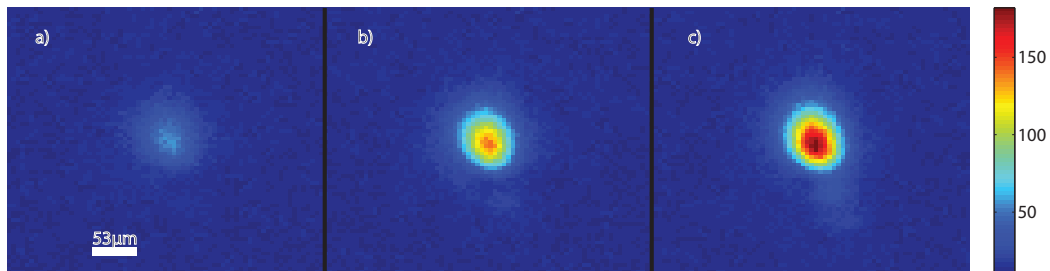
Figure 3.6: UV Beam profile at the focus in the experimental chamber underneath the TOF detector at different pressures in the THG target (a: 2 bar, b: 5 bar, c: 8 bar). The full width at half maximum (FWHM) of a two dimensional Gaussian with arbitrary rotation fitted to the spot at 8 bar is $50 \times 70 \mu m^2$ and almost identical at other pressures.

compressed pulse of 3.5 fs FWHM we can reach an intensity of $2.4 \times 10^{12}$ W/cm$^2$ on target.

Employing the frequency tripling approach with compressed pulses from a system very similar to FP3 pulse lengths of 2.8 fs have been demonstrated [52]. In this work there are no compression techniques in use after the tripling process. Since we are using precisely the same approach as in the work of Reiter et al. we made the assumption that our pulses would also be compressed and started the experiment without the capacity for UV pulse length measurement. Nevertheless it is noteworthy that a measurement of the pulse length with one of the three following approaches is planned and preparations have begun. Such a measurement should be possible with:

- A transient grating FROG 2.1.5. Here we need a very thin nonlinear medium so we change the UV pulse as little as possible during the measurement. A similar device has successfully been used by Graf and coworkers [85]. A downside to this approach is the fact that the pulse always has to propagate through some medium that potentially changes its temporal structure even if it is as little as the 10 μm thin fused silica slides available to us. It would be possible to design the FROG such that the beam transmitted through the entire apparatus is picked off behind the experimental chamber in an additional vacuum chamber. In this way a measurement is possible without disturbing the setup for the actual experiment.

- A UV/UV autocorrelation similar to the one performed in [52]. Here we would need to make drastic changes to the setup. Mounting an ion detector perpendicularly to the electron detector would not pose a problem in principle. But it would also be necessary to put a split mirror in the beam path of the UV arm of the delay chamber interferometer. Splitting the mode in this way even when there is currently no pulse length measurement planned would deteriorate the beam quality and reduce the amount of transmitted power.

- A streaking measurement of the UV light. This approach would yield the most
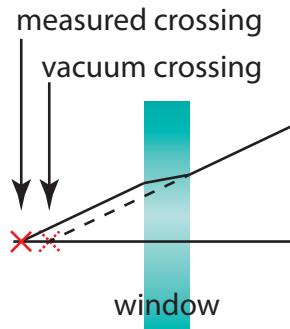
Figure 3.7: Illustration of the alignment complications of a noncollinear interferometer in vacuum. In this simplified two dimensional drawing it looks like the crossing is just shifted. In reality a similar thing happens for the orthogonal projection and the beams do not necessarily cross at all in vacuum when they are aligned outside. We cannot use a camera outside of vacuum for fine alignment of the spatial overlap.

detailed and relevant information about the pulse. Streaking would take place at the exact spot where the pulses are used for other experiments. It would also reveal the carrier envelope phase of the UV pulse. And one can extract the XUV pulse parameters from a spectrogram, allowing for a diagnostic measurement of one more possibly unknown quantity. Since streaking with UV pulses has never been done before it is also clearly the most interesting pulse measurement method. While this assessment makes it sound like streaking is the best approach for our diagnostic there are of course some technical challenges to overcome. Especially noteworthy is the fact that not only the UV light but also the fundamental NIR light will streak the photoelectrons. We will discuss how well we have to do this in the following chapter. Another caveat is the fact that the high temporal resolution necessary for a streaking measurement of UV light with a period of only $\approx 880$ as requires a large bandwidth. According to equation 3.2 we would need a bandwidth of about $4.25\,\mathrm{eV}$ to sample at a time resolution of $440\,\mathrm{as}$, half the period of the UV light. An excited state in ozone would be separated from the ground state by the central energy of one UV photon: only $4.5\,\mathrm{eV}$. So it is not possible to use the same XUV mirror for both UV streaking measurements and photoelectron spectroscopy of ozone because the signal from the excited state would not be distinguishable from the ground state. If we performed a UV/XUV cross correlation with a smaller mirror bandwidth it would not reveal the complete UV field – but we would be able to measure the envelope.

## 3.3.2 IR Suppression

When we want to perform UV pump XUV probe experiments with frequency tripled pulses we have to carefully consider how much fundamental light we can permit to shine
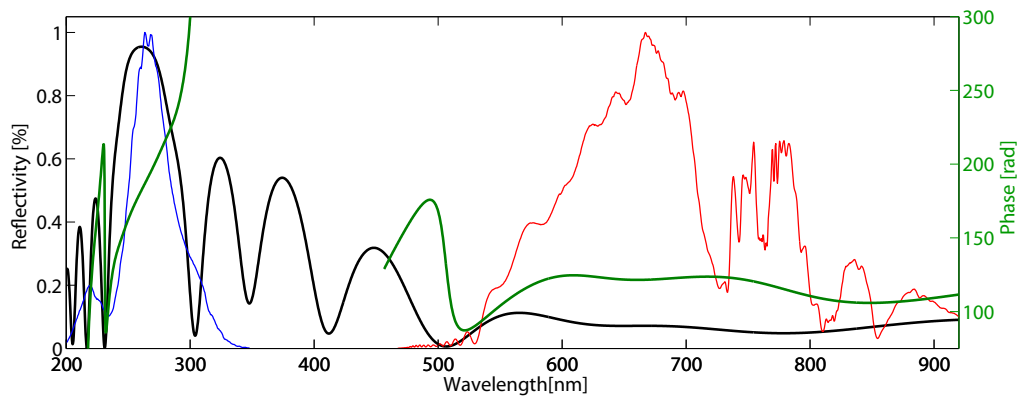
Figure 3.8: The reflectivity (black) and phase (green) of the NIR suppressing dielectric UV mirrors. The phase in the NIR has been shifted down by 1150 rad. The fundamental (red) and THG (blue) spectrum are plotted for comparison with the reflectance. After two reflections the NIR light is suppressed by roughly two orders of magnitude. Also the phase is flat over the majority of the UV spectrum, which means that it does not lengthen the pulse significantly. The reader might wonder why the NIR spectrum differs from the one shown in 3.12 – the spectrum shown here was acquired behind the experimental chamber with a running HHG and THG target. Especially the THG target can be expected to cause spectral shifts in the high pressure gas. The mirrors were designed and coated by Olga Razskazovskaya.

on the target without disturbing the experiment. In the experiments with ozone we have to make sure that we do not change the electronic configuration of the molecule with the NIR light. One way to find out whether there is an obvious influence of NIR light on our system is to perform experiments without UV light at high NIR intensities. While this will be discussed in more detail in section 3.5.1 we will forestall the result and claim that there is no visible change in the photoelectrons due to NIR irradiation apart from streaking. So there are no added requirements for IR suppression to prohibit population in the Chappuis band. If, on the other hand, we wanted to perform a streaking measurement of the UV light, the situation is quite different. We need to make sure that the UV field will yield the main contribution to the trace. As we can see in equation 2.9 the streaking amplitude scales with the vector potential. Calculating the vector potential for different wavelengths but identical intensities leaves us with the following consideration

$$
\begin{aligned}
A &\propto \frac{E_0}{\omega} \\
E_0 &\propto \sqrt{I} \\
A &\propto \frac{\sqrt{I}}{\omega} \\
\Rightarrow A_{UV,3\omega} &= \frac{1}{3} A_{IR,\omega}
\end{aligned}
\tag{3.5}
$$

where $A_0$, $E_0$, $I$ and $\omega$ denote the amplitude of the vector potential, the amplitude of the electric field, the intensity of the field and the frequency of the laser field, respectively. So simply the fact that the frequency of our UV field is three times that of the fundamental costs us a factor of three in the streaking signal. Adding in the fact that the conversion efficiency from NIR to UV is around 1 % we see that we need to suppress the intensity of fundamental light by at roughly three orders of magnitude to get a significantly stronger signal from UV streaking than from NIR streaking.

Due to the large bandwidth of our UV pulses it is virtually impossible to use optics in transmission in the UV beam path without significantly stretching the pulse in time. This narrows our options down to dichroic mirrors. We have employed two different types of such optics, the first being a specially coated multilayer system that has high reflectivity in the UV and low reflectivity in the NIR (see figure 3.8). In contrast to metal mirrors multilayer mirrors do potentially introduce a considerable spectral phase to the pulse. It is therefore absolutely necessary to have the high reflectivity region extend over the entire usable spectrum. At the point where the reflectivity drops sharply the phase also changes rapidly and a reflected pulse would be distorted.

While the dielectric mirrors have an even higher reflectivity than metal mirrors they can potentially stretch a UV pulse. A perfect match between the UV spectrum and the dielectric mirrors has not yet been found, but our efforts are ongoing. An option for NIR suppression that does not add any spectral phase are silicon mirrors used at Brewster's angle. This approach has been successfully used in a number of works [87, 52, 85]. The main idea is simple: while the reflectivity of p-polarized NIR light is very small (in theory it is zero) the UV reflectivity is still $\approx 0.44$. In practice it is possible to suppress

fundamental light by two orders of magnitude with two reflections. After such a chicane in the beam path we are left with $\approx 20\%$ of the original UV power.

Even when we suppress the largest part of the IR there is still a chance to observe streaking. Whether or not that is a problem depends on the streaking amplitude compared to the expected signal magnitude. If the signal from the excited state is very weak we have to do better in the IR suppression. Additionally the UV can of course also produce a streaking signal. In order to suppress this as well we can monitor the system in the direction that is orthogonal to the polarization of the NIR/UV fields. According to section 2.1.3 the transverse streaking signal goes with the square of the vector potential and will therefore be reduced more strongly than the longitudinal streaking signal. Another possible method for avoiding a streaking signal is called *differential streaking*. In this approach we modulate the CE-phase between adjacent pulses by $\pi$ [88]. This will not affect XUV or UV generation, but it will reverse the sign of the streaking field. Adding up the retrieved traces for adjacent pulses then subtracts the streaking signal. In our situation we can only use this technique for IR suppression, but it would not work for UV streaking. This is due to the fact that it is impossible to have both the time resolution for UV streaking and the energy resolution for the observation of a UV induced excited state at the same time. So a UV streaking spectrogram would be smeared out and it would be impossible to subtract the adjacent pulses. Transverse streaking of UV light on the other hand would be a very small effect. We can compare traces obtained from oxygen with those from ozone and distinguish between streaking and population signals.

## 3.4 Calculations and Expected Experimental Results

### 3.4.1 Full-fledged Quantum Calculations

Ozone is a molecule containing 24 electrons spread over three nuclei and its theoretical description is quite challenging. State of the art calculations take nine states into account when describing the photodissociation with different colours of light [89]. Most reports focus either on the timescale on which the core movement happens or on time independent spectra. This is absolutely reasonable since few femtosecond pump pulses are not widely available and have only been created recently. Nevertheless it is essential for the comprehension of experimental data to have a solid theoretical background for interpretation of measurements. To this end we have established a cooperation with the group of Professor Ágnes Vibók from Debrecen University who has explored the first femtoseconds after photoexcitation in great detail. We shall now review the findings of our collaborators.

As mentioned in section 3.1 it should in principle be possible to coherently excite the Chappuis and Hartley bands simultaneously, read them out and see a quantum beat between the levels. In order to do that one must take into account that the absorption cross section of the Chappuis band is about one thousand times weaker than the one in the Hartley band. One might assume that it is still possible to see the beating signal as long as one excites the NIR band with a pulse that is that much more intense. Of course

this is basically true up to a certain point where the intensity is so high that it triggers unwanted processes such as an excessive amount of ionization. In order to judge the feasibility of this experiment Halász and coworkers performed the following calculations [27].

In a first step the wavefunctions for electrons and cores are separated in the Born–Oppenheimer approximation. Stopping there would of course mean that some of the most interesting and crucial dynamics of the system could not be described. After the first $5\,$fs to $6\,$fs both electrons and nuclei are in motion. So the electron dynamics are introduced into the core wavefunctions by means of a nonadiabatic coupling term. This term also includes the electronic coupling to the laser field. Then the time dependent Schrödinger equation including the coupling term is solved in a *Multi-Configuration Time Dependent Hartree Fock* calculation. The results are used to calculate the density matrix of the system. From the diagonal and off-diagonal elements of the density matrix one can obtain the populations and coherences of the system. The laser parameters were close to what we were expecting to be able to deliver in an experiment, with the added exception that the UV intensity was adjusted to make sure the populations in both excited states roughly match. This means that the NIR central wavelength was $750\,$nm at $10^{14}\,$W/cm$^2$ and $4\,$fs (FWHM). For the UV the parameters were: $260\,$nm central wavelength at $2 \times 10^{11}\,$W/cm$^2$ and $3\,$fs (FWHM).

From these calculations we can learn three main points:

- After $5\,$fs to $6\,$fs the cores move and the system is no longer in the Frank Condon region. Before that the nuclei can be regarded as stationary.

- The symmetry of the ground state and the two excited states in the Hartley and Chappuis bands dictates that they cannot be excited with the same polarization. For the effective polarization for UV excitation relative to the molecule, see the inset in figure 3.9b.

- Even at a considerable NIR intensity of $10^{14}\,$W/cm$^2$ the population in the Chappuis band reaches a mere $1\,\%$

Taking the latter two points into account we can conclude that both the simultaneous excitation and detection of population in both excited states would be extremely challenging. Our UV light is created with the same polarization as the fundamental light. Transmissive optics cannot be used with our short pulses[10] and we have no way of rotating just one of the two polarizations. Also the population of one percent is usually below the noise level in attosecond photoelectron experiments. In conclusion, the three color experiment is probably not feasible. On the bright side, there is no additional requirement on the NIR suppression since the effect of fundamental light is so small.

After this finding it made sense to study the UV pump/XUV probe setting in more detail [90]. In their next paper Halász et al. used the same approach as before but considered only one pump pulse with a central energy of $260\,$nm and an intensity of $1 \times 10^{13}\,$W/cm$^2$

---

[10]The combination of the bandwidth, short wavelength of the UV and the large difference in central energy of our pulses prohibit the use of waveplates.

and a pulse length of 3 fs (FWHM). Here the goal was to simulate the largest possible population and thus the maximum possible UV intensity was taken for the calculation. The main results are:

- At the aforementioned pulse parameters we can transfer about 40 % population to the excited state. As mentioned before it is only possible to excite ozone with one polarization in the UV. Therefore this result is only valid for aligned molecules. Since we are dealing with a randomly oriented gas we are only populating one third of the calculated value: 13 %. As of now it is not known which cation state is formed by the ionization from the excited state. This would be necessary for determining the polarization response of the system. It is conceivable that the excited state preferably emits asymmetrically with respect to the polarization axis – and we would have to look for a signal in both directions.

- The Coherence between ground state and excited state rises sharply with the pulse, then decays when the pulse is gone – and rises again to a much smaller value roughly 17 fs after the pulse is over (see figure 3.9). The drop in coherence is explaind by the wavepacket moving away from the Frank-Condon region. For coherence some overlap between the wavefunctions is necessary. When the overlap is lost, the coherence is lost as well. The later revival is essentially the reverse process. A part of the wavepacket returns to the Frank-Condon region and can now overlap with the ground state again. The entire process is much too fast for typical decoherence processes like collisions between gas atoms. Coherence revival in principle is not a new phenomenon and has been seen in experiments at least 30 years ago [91] – obviously not on this ultrashort timescale.

These theoretical predictions have so far concerned only one side of the experiment: the pump process and subsequent dynamics in the system. Now we still need to understand the probe process and the signal that we could expect. In order to estimate the photoelectron spectra Perveaux et al. calculated the Dyson orbitals for Ozone [92]. These orbitals are constructed by calculating the overlap of the neutral molecule wavefunction with that for the ionized molecule [93]. They have the extremely useful property of being proportional to the angularly resolved photoelectron yield[11]. In the next step Perveaux et al. calculated the photoelectron yield for all relevant transitions in a stick spectrum [94]. Then they incorporated the poor spectral resolution of a short XUV probe pulse and convoluted the stick spectrum with a gaussian of FWHM 3.65 eV (see figure 3.10). This corresponds to a time resolution of 500 as. The best way to see the effect of rising population in a photoelectron spectrogram is a differential plot where the ground state spectrum is subtracted from all spectra. Such a spectrum is also shown in figure 3.10. Just as in the previous calculations the pump pulse parameters were: 260 nm central wavelength, an intensity of $1 \times 10^{13}$ W/cm$^2$ and a pulse length of 3 fs. Here a central energy of 95 eV for the probe pulse was used. The key lessons from the calculation based on Dyson orbitals are:

---

[11]In our setup we do not have angular resolution, but the photoelectron spectrum can still be reproduced by integrating over the collection angle or assuming emission along the detector axis.
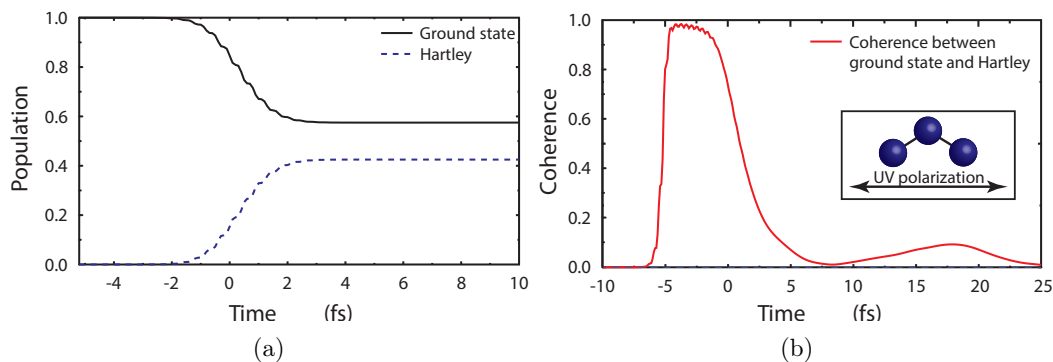
(a)                                        (b)

Figure 3.9: **a)** Population in ground state and excited state in the Hartley band of ozone. when pumped with intense UV radiation. The 3 fs, $10^{13}$ W/cm$^2$ UV pulse used for the calculations is centered at $t = 0$. **b)** Coherence between ground state and Hartley band excited state. The revival at $\approx 17$ fs is clearly visible. The polarization of the UV pump pulse relative to the molecule is depicted in the inset. Note the different scale on the time-axis. Adapted from [90]
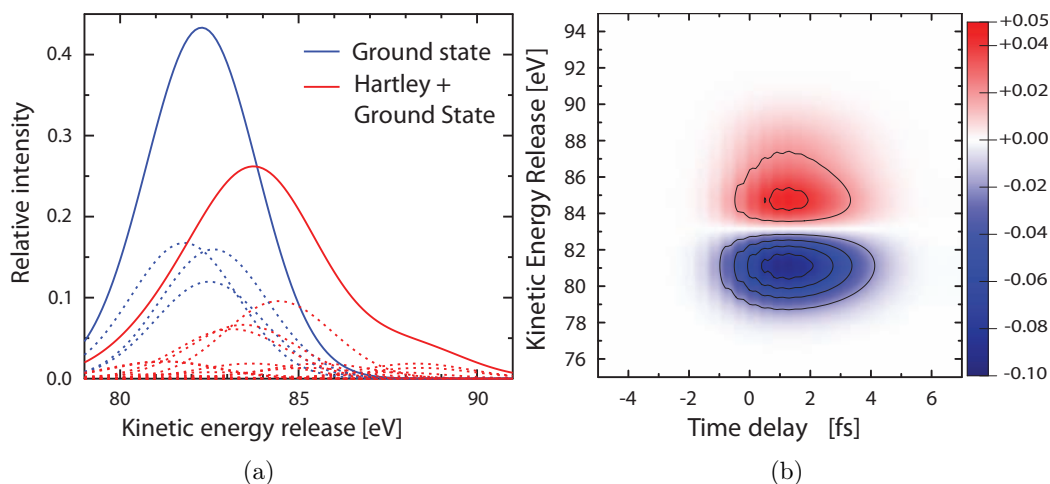


(a)                                        (b)

Figure 3.10: **a)** Calculated photoelectron spectrum of ozone excited with UV pulses at 260 nm with an intensity of $1 \times 10^{13}$ W/cm$^2$ and a pulse length of 3 fs. This graph is the result of a stick spectrum of individual transitions that was convoluted with a Gaussian of FWHM 3.65 eV to take into account the spectral width of the XUV pulse centered at 95 eV. The individual absorption lines are represented by dotted lines. **b)** Differential photoelectron spectrogram simulating the time evolution of the signal at the Frank-Condon point. The rapid decrease of the differential signal can be attributed to the wavepacket leaving the FC point. Adapted from [94]

- At the assumed pump parameters of $260\,\text{nm}$ central wavelength, $1 \times 10^{13}\,\text{W/cm}^2$ intensity and $3\,\text{fs}$ pulse length the differential signal has a contrast of $^{1.05}/_{0.9} \approx 1.17$.

- This result is only valid for aligned molecules. The population for non-aligned particles will be about $^1/_3$ of the population in the aligned case. The contrast for a differential signal will decrease accordingly.

### 3.4.2 Three Level Calculations

After reviewing the previous section one might wonder why another type of calculations is still useful after such a detailed theoretical description. The idea behind it is simple: we needed a way to quickly estimate the experimental outcome when parameters changed – without having to run a supercomputer or having to approach our collaborators. These calculations were performed by Tobias Latka [95]. The Ansatz is a simple Hamiltonian that shows the three levels and their separation by one UV/NIR photon.

$$\widehat{H}_0 = \hbar \begin{pmatrix} 0 & 0 & 0 \\ 0 & \omega_{\text{NIR}} & 0 \\ 0 & 0 & \omega_{\text{UV}} \end{pmatrix} \tag{3.6}$$

With the frequency of the NIR and UV fields denoted by $\omega_{\text{NIR}}$ and $\omega_{\text{UV}}$. Then the coupling terms to the field are added in:

$$\widehat{V}(t) = -\widehat{d} \cdot \widehat{E}(t) = - \begin{pmatrix} 0 & \vec{d}_{01} \cdot \vec{E} & \vec{d}_{02} \cdot \vec{E} \\ \vec{d}_{10} \cdot \vec{E} & 0 & \vec{d}_{12} \cdot \vec{E} \\ \vec{d}_{20} \cdot \vec{E} & \vec{d}_{21} \cdot \vec{E} & 0 \end{pmatrix} \tag{3.7}$$

$$\vec{d}_{ij} = \vec{d}_{ij}^{*} \tag{3.8}$$

Where 0 denotes the ground state, 1 the exited state accessible via a NIR photon, 2 the excited state accessible via a UV photon, $\vec{E}$ is the electric field and $\vec{d}_{ij}$ is the dipole moment coupling the states $i, j$. Then we make the assumption that Electric field and dipole are collinear (as in the more elaborate calculations). Of course this is an Ansatz that completely neglects nuclear dynamics. But this is justified in the first few femtoseconds after excitation, which is the time-window we will be concerned with. From here we calculate the density matrix via the Lindblad formalism [96]. For the magnitude of the dipole moment we can rely on the careful analysis of our collaborators. We perform a calculation for the standard pulse parameters used by Halász et al. and adjust the dipole moment such that the results match. This results in a dipole moment of $1.85\,\text{Debye}$. Then we can change the pulse parameters to those that we see in the experiment. Since we already know that the population in the Chappuis band will be near zero we leave the NIR amplitude at zero and calculate only the Hartley band. An exemplary graph is shown in figure 3.11.

When we apply the Ansatz to our parameters we see that we populate approximately $15\,\%$ of the excited state for aligned molecules- or $5\,\%$ for non-aligned molecules. That would be about $^1/_8$ of the assumed value for the differential spectrogram in figure 3.10.
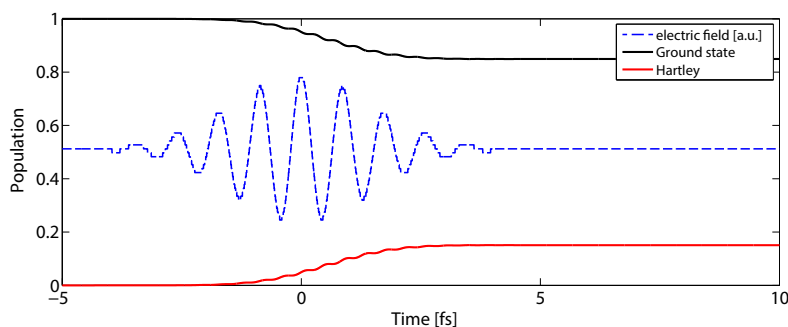
Figure 3.11: The result of a three-level calculation for ozone pumped with UV light with an assumed pulse length of 3.5 fs, a central wavelength of 265 nm and an intensity of $2.4\,W/cm^2$. These results can only be trusted for the first few femtoseconds because they are obtained while completely neglecting core movement. They also assume that the molecular dipole moment and electric field are aligned.

Since we only had a contrast of 1.17 there we can assume to have a weak signal that requires a high signal to noise ratio to see the excitation.

## 3.5 Time Resolved Photoelectron Spectroscopy on Ozone

### 3.5.1 IR Pump, XUV Probe

From the previous section we learned that an IR induced signal would be very weak and almost impossible to detect if the data quality is not very good. So the first experiment is the acquisition of a static spectrum in order to judge the attainable signal to noise. In order to compare with a well known and easily manageable system we used Neon gas. For the results, see figure 3.12. The spectra were acquired under very similar settings right after each other (while allowing some time for pumping the Neon gas out of the system). The XUV pulse was centered at 130 eV with a bandwidth of 3.5 eV. Typical acquisition times for a streaking spectrogram with Neon as an electron source range from 1 s to 4 s per individual spectrum. Evidently this is not going to be long enough for experiments with ozone. We only get acceptable signal to noise ratios for much longer acquisition times from 30 s to 120 s. The reason for this is not only the cross section of ozone and neon but also the slightly different alignment for the beamline when working with UV light: the high photon energy of the UV light is comparable to the work function of our multi channel plate detector. And while it is difficult to see the light reflected off the gas nozzle with NIR light we actually get a huge peak from UV light, because now the electron generating process is a one photon process as opposed to the three necessary photons for NIR. The large light induced peak has an asymmetric tail on the low energy side that can extend all the way to the energy of XUV produced photoelectrons and generate a noisy background. To avoid this we have to move the nozzle slightly away
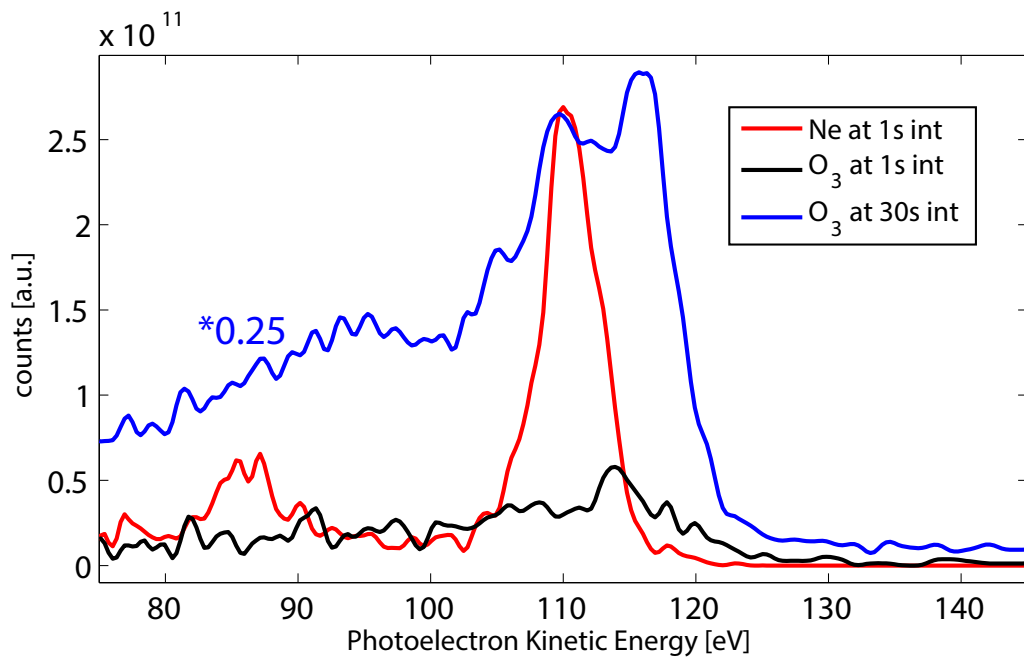
Figure 3.12: Stationary photoelectron spectra of Neon and ozone. The red and black
curve were obtained at an identical integration time of one second. The
blue spectrum was recorded at 30 s integration (divided by 4 for visibility
of the other spectra). Evidently the signal to noise ratio is much worse for
ozone at comparable integration times.

from the beam. This strongly reduces the background, but it also reduces the gas density
under the detector and thus the photoelectron signal. From figure 3.9 we can see that
a populated excited state should live for 10 fs without any decline. It seems plausible
that it would not abruptly cease to exist afterwards but to slowly decay. This is why we
chose to perform experiments with few time steps but a long integration time for each
individual step. Then we can compare the spectra after the pulse to a spectrum before
the pulse to see first signs of population in the excited state. One such spectrogram is
shown in figure 3.13. For this data we increased the NIR intensity so far that the lower
energy electron background was just outside of our region of interest for XUV produced
photoelectrons. The TOF detector is mounted perpendicularly to the field polarization
to suppress streaking. But we can see that transverse streaking is at least so strong
that it could overwhelm a weak signal from the excited state. So we definitely need to
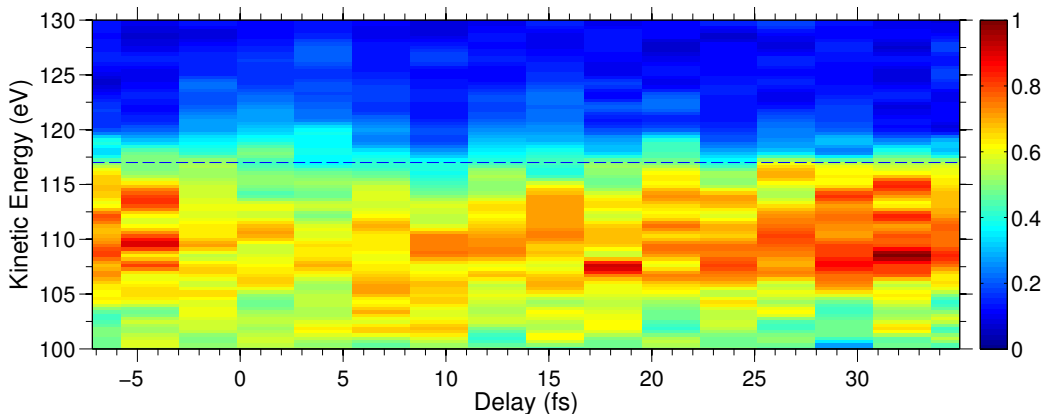suppress it for the final experiment.

Figure 3.13: Normalized differential spectrogram of ozone pumped with IR acquired perpendicular to the IR polarization. The dotted line shows the edge of the ground state. Indeed there is a signal above the line. At the same timesteps one can observe a shift of the center of the photoelectron line to smaller kinetic energies. This is *transverse streaking* as introduced in section 2.1.3. The integration time for this spectrogram was one minute per time step. A negative time means that the probe pulse comes before the pump pulse.

### 3.5.2 UV Pump, XUV Probe

Since we now know that sufficiently populating the Chappuis band is next to impossible with our experimental setup we study the Hartley band. We learned that we have to suppress the NIR field to eliminate transverse streaking. At this stage of the experiment the multilayer mirrors are not usable because we cannot measure the UV pulse duration yet and are there remains considerable uncertainty about the effect of the mirrors on it. So we have to resort to Brewster reflections off of Silicon wafers. This leads to a significantly reduced UV intensity of about $0.5 \times 10^{12}\,\mathrm{W/cm^2}$. We would not expect to see a signal at such a low intensity. Figure 3.14 shows a differential spectrogram that unfortunately confirms our expectations.

## 3.6 Conclusions

We have designed and built a setup that is capable of creating ultrashort pulses in the deep UV at a central wavelength $265\,\mathrm{nm}$ with pulse energies of up to $7\,\mathrm{\mu J}$ utilizing frequency tripling. This setup utilized neon gas at backing pressures from 1 bar to 11 bar, while a differential pumping setup ensures that the gas flow does not affect the adjacent high vacuum part of the beamline. While the UV target is running and large amounts of neon gas are being pumped through the setup we ensured that the mechanical stability was sufficient for streaking experiments. These capabilities were combined with the interferometric beamline AS2 and now experiments with intense ultrashort deep UV
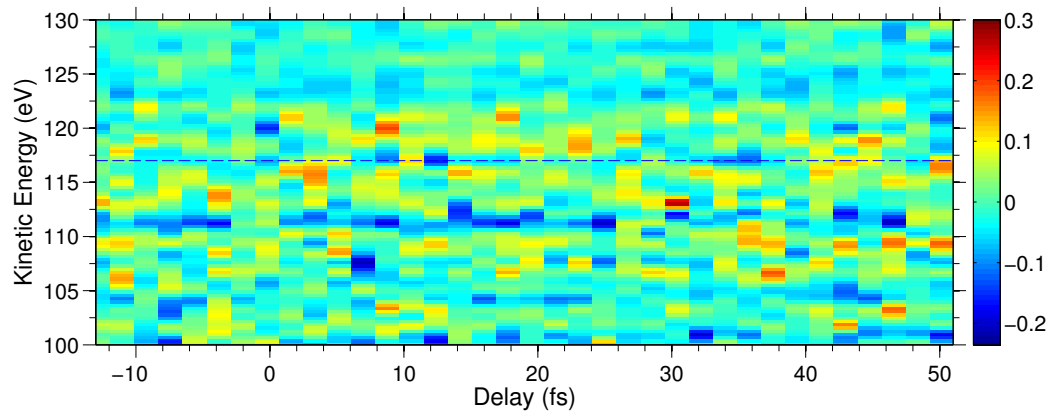
Figure 3.14: Normalized differential spectrogram of ozone pumped with $0.5 \times 10^{12}\,\mathrm{W/cm^2}$. There is no discernible signal present.
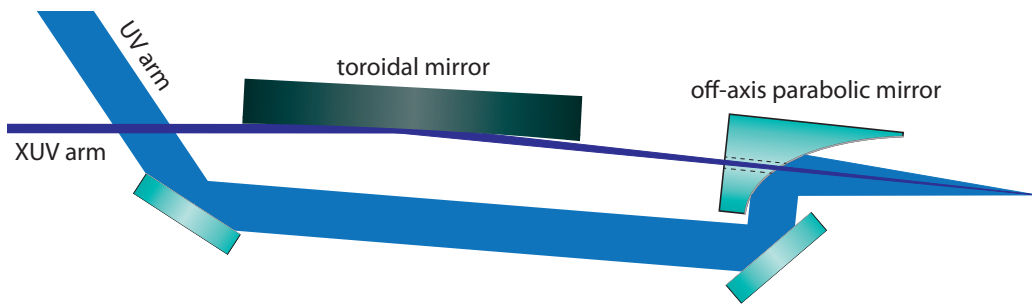


Figure 3.15: The proposed new focusing scheme that would focus the two beams with different optics.

pulses and attosecond XUV pulses are possible.

We have created an ozone source that is capable of fueling a gas target for photoelectron experiments with high purity ($\approx 95\,\%$) ozone for at least 2.5 hours.

We established a collaboration with the group of Professor Vibók. From their calculations we learned that the population that we can introduce to the Chappuis band will probably not be detectable with our setup. We also saw the precise way in which the Hartley band would be populated and the subsequent dynamics that we can expect. From this we learned to judge the UV intensity necessary for a strong enough population in the excited state to be visible in an experiment. For our current experimental situation a signal can not be expected. In the next section we sketch our next steps to obtain a detectable signal.

## 3.7 Outlook

The experimental difficulty of seeing a signal from the excited state can be viewed from two perspectives: either there needs to be enough population to detect it even with bad signal to noise ratio or we need to change the readout and detection in order to improve the signal to noise ration and the contrast between ground and excited state.

Building on the theoretical results we can assume that we need an order of magnitude higher UV fields in order to generate a large signal that is easy to detect. It is essentially impossible to generate that much more pulse energy with the gas harmonics that we are using. But we do not necessarily need higher energies- just higher energy densities of the UV light in the volume probed by XUV pulses. Naturally the idea of tighter focusing comes to mind. While this is a trivial task for visible wavelengths it can be rather demanding for XUV light. We would essentially need a toroidal mirror with a much shorter focal length. Optics need a surface quality that scales with the wavelength of the reflected light and thus it is very difficult and expensive to obtain large XUV capable optics. In addition toroidal mirrors are notoriously hard to align – and this behaviour scales unfavorably with decreasing focusing length. So our approach is slightly different: we still focus the XUV light with the toroidal that we are using at the moment. But we focus the UV light with a perforated off-axis paraboloid (see figure 3.15). Since the parabolic mirror is placed in the converging part of the XUV beam, the hole in it can be small. So we would not lose as much energy as before when we are working in a collinear geometry. Tighter focusing would also improve the signal to noise ratio as a smaller UV focus would permit us to move the gas nozzle closer to the XUV beam, yielding a higher gas density at the focus. A smaller focus for only the UV light would unfortunately prohibit streaking measurements, for which one needs a homogeneous streaking field over the XUV focus diameter. As long as both pulses are focused with the same optics this is certified by the much smaller wavelength of XUV.

Another easily implementable way to increase the contrast is by decreasing the spectral overlap between ground and excited state. An XUV mirror with a smaller spectral bandwidth would make the separation of the two peaks a lot easier. It would of course have a worse temporal resolution and is not suitable for high end experiments. But even a weak signal can be optimized. A narrow band mirror would certainly help in finding it, optimizing it and then switching mirrors and performing the experiment.

As we cannot be sure about the preferred emission direction of photoelectrons from the excited state it is possible that we have to rotate the NIR polarization relative to the XUV polarization in order to fulfill two criteria simultaneously: electron detection in the transverse streaking direction and in the main photoemission direction. We have designed a compact periscope for polarization rotation that can be inserted into the beam right before UV generation for this purpose.

Of course we would also benefit strongly from a completely compressed IR pulse. It would boost both UV and XUV generation. To this end a new combination of differentially pumped hollow core fiber and chirped mirrors is currently being produced and tested.

Even though we are using an approach that was proven to yield compressed pulses in

past reports [85, 52] we can not be certain that the UV pulses do not get stretched in the high pressure gas target or in other places such as the protective layers on the metal mirrors or the dielectric mirrors. We are currently constructing a UV capable transient gating FROG that will be placed behind the experimental chamber (where there is now a UV diode and spectrometer in figure 2.12).

# Chapter 4

# Metal–Organic Molecules on Surfaces

The dye–sensitized solar cell shows great potential for the delivery of cheap energy [30]. For more than a decade all of the involved charge transfers have been studied, but one of the steps was never experimentally monitored: the very first one. Here we present our efforts towards the detection of intramolecular charge rearrangement in a solar cell model system: metal–organic molecules on a semiconductor surface.

## 4.1 Principle of the Experiment

This experiment is carried out in a pump probe scheme. A few femtosecond NIR pulse excites the molecule and induces an intra-molecular charge rearrangement. When the electrons rearrange they change the amount of charge in the vicinity of the nuclei. This in turn affects the screened nuclear potential acting upon the remaining electrons- also the core electrons that do not take part in the formation of chemical bonds. And when these core electrons are subjected to a different binding potential, their binding energy will change, which can be measured by photoelectron spectroscopy. This effect is called *chemical shift*. It seems reasonable to assume that the effect will be strongest when the spatial overlap between the highest occupied molecular orbital ($HOMO$) and lowest unoccupied molecular orbital ($LUMO$) on the atom that provides the core level to read out is small. This is the case for a metal to ligand charge transfer ($MLCT$). The dye molecule that was originally used for dye sensitizing solar cells, $Ru(H_2L)_2(NCS)_2$, where $H_2L$ is 4,4'-dicarboxylic acid-2,2'-bipyridine, called *N3* shows such an MLCT for its absorption peak in the red [97]. Its structure is depicted in figure 4.1. For the detection of the chemical shift we then ionize the sample with an attosecond XUV pulse and plan to see the change in binding energy via a time-of-flight detector.

All of the experiments in this project are carried out in the AS3 beamline (see chapter 2.2.2 for a description of the apparatus). It provides the surface science tools that are necessary for sample manipulation, cleaning and diagnostics.

## 4.2 Sample Choice

The dynamics that we are interested in are common in the entire class of metal-organic molecules. We do however have a large number of experimental constraints that dictate which candidates are possibly suitable. In addition we have to consider the substrate
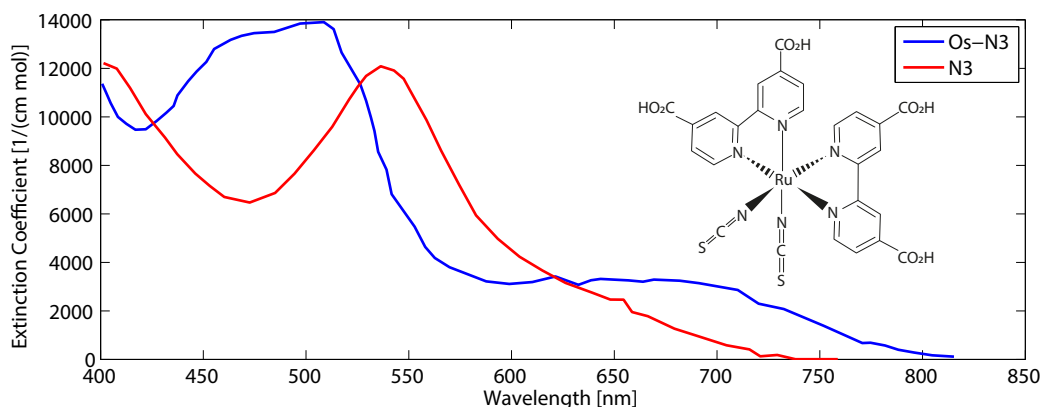
Figure 4.1: N3, the first successfully tested dye for solar cell sensitization. The red line denotes the absorption curve of N3 while the blue line represents an N3 molecule where the ruthenium center has been exchanged for an osmium center. The higher absorption in the near infrared for Os-N3 is caused by the heavy atom effect which facilitates triplet transitions due to improved spin-orbit coupling. Osmium also has a higher absorption cross section than ruthenium in the relevant XUV energy range (see figure 4.2). Data adapted from [98].

that our molecules will be resting on. So we have a lot of choice when it comes to the perfect sample for our experiments. Our selection criteria are as follows

- For the excitation we need an absorption band overlapping the NIR pulse centered at $780\,\mathrm{nm}$

- For efficient detection of the excited state we need an atom in the molecule with a core level that has with a binding energy small enough to be ionized by one XUV photon and has a large absorption cross section

- The core level has to be chemically shifted during the excitation

- The molecule must be durable enough to withstand pump and probe pulses

- The molecule must stick to the substrate- preferably with covalent bindings that withstand considerable laser intensities.

- The substrate cannot have electron emission that spectrally overlaps with that of the molecular core level – be it Auger electrons or direct photoemission.

- We have to be able to prepare a clean sample. This includes two points: cleaning the substrate and subsequently depositing the molecules. If there is a layer of contamination on top of the molecules we will not be able to perform the experiment

because photoelectrons at our typical kinetic energies have a very small mean free path on the order of a few Angstrom[1]. We would lose a large part of the signal due to inelastic electron scattering even with just a monolayer of contamination.

### 4.2.1 The Substrate

For the substrate we wanted to chose a semiconductor in order to stay close to the relevant system for the technical application. We decided to use silicon in the (111) orientation for several reasons. It is available cheaply and easily in great quality. The large amount of experience in the research community with this material means that cleaning and handling procedures are readily available. We can functionalize molecules with carboxy or hydroxy groups to make them form covalent bonds with the surface. Silicon does not have states that overlap with those of the metal center. Electrons from the 2p state at 99.3 eV will be emitted in our experiments, but they are separated in energy from those of the metal center (see figure 4.4). We do have to be careful to chose our XUV central energy such that we avoid the superposition of our signal with Auger emissions at 92 eV and 107 eV kinetic energy. One way to get around this is to choose a central XUV energy below the binding energy of Si 2p, which can be beneficial for the tagged molecules discussed in section 4.3.2 and following.

### 4.2.2 The Molecule

The first candidate for a molecule that comes to mind is the dye that was used in the first dye sensitized cell. It is called N3 and is shown in figure 4.1. Let us illustrate the experimental problems associated with this choice. First of all, the optical absorption curve does not match our laser very well. It is suitable for absorption of solar radiation which peaks around 500 nm. This wavelength is too short for efficient excitation with our laser system. Secondly, the central metal atom, Ruthenium, has a low absorption cross section of roughly 0.5 Mbarn in the reachable 90 eV to 145 eV photon energy range. For comparison, the solid state experiments that have so far been carried out with our equipment have mostly been using tungsten as a sample. Its valence band, comprised mostly of 5d electrons, has a comparable cross section. But a three–dimensional, crystalline material has a much higher density than the one metal atom in a monolayer of metal-organic molecules. So we can expect a signal from ruthenium to be very weak. A less obvious problem with this molecule is its lack of structural solidity. In an ideal situation we would like to deposit a layer of molecules onto a clean surface in ultra high vacuum. This is conventionally done via molecular beam epitaxy (*MBE*). In such a system one brings a reservoir of molecules in front of the surface to deposit them on and then heats them up in a controlled way. When the temperature surpasses the desorption temperature, the molecules will loosen from the reservoir and travel ballistically to the sample surface where they can attach. But If N3 is heated up it has a tendency to break

---

[1] See [99] for data on mean free paths of elemental solids. To our knowledge there is no such data for unordered molecular films, but since the qualitative form of the mean free path is so similar for so many different elements we conclude that it will at least follow the same tendency.
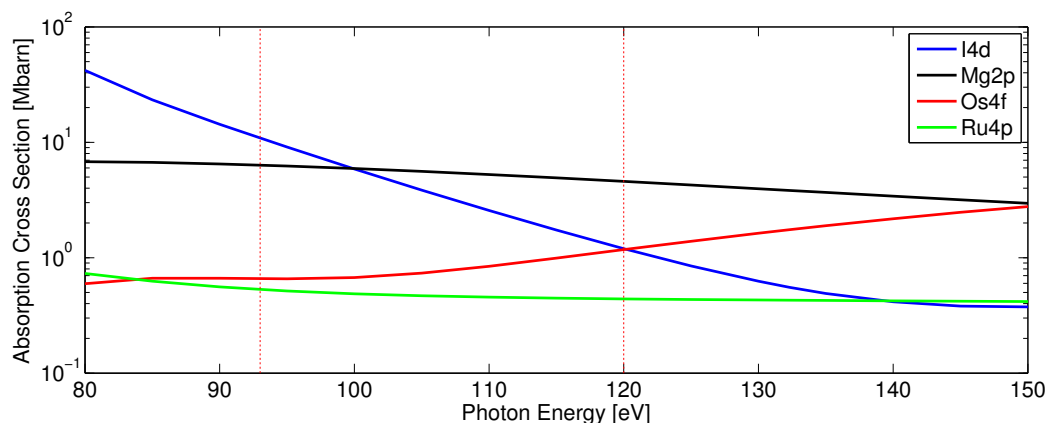
Figure 4.2: Absorption cross sections for a number of suitable candidates as a part of the molecular compound to be studied. The cross sections are plotted for the maximum currently reachable photon energies with our light source. The dotted vertical lines show the photon energies at which we have performed the experiments presented in this thesis. Magnesium has been included in this graph since it has also been tried as a central atom for direct detection- but the cross section is still too low for a time resolved measurement [100]. Data taken from [101, 102].

apart before sublimation. This was confirmed by scanning tunneling microscopy studies performed at the E20 chair of TUM by Agustin Schiffrin. We believe that this behavior is due to the structure of the molecule – every part of it hinges on the metal atom through a coordinated binding. In such a bond both binding electrons in an orbital originate from the same nucleus. A coordinate of bond can be as strong as a covalent one, but it is typically weaker [93, 103]. When the molecule is heated up the organic parts, which are only connected through the metal center, can gain enough kinetic energy to tear the molecule apart.

When selecting a better sample we can kill two birds with one stone when we try to re-place the central ruthenium atom with an osmium atom. Osmium has a core level with an absorption cross section that is two to four times larger than that of ruthenium (de-pending on the photon energy, see figure 4.2 for an overview of potential candidates' cross sections). In addition it induces the *heavy atom effect* [104] in the molecules it is part of. In molecules similar to N3 the absorption in the NIR range of the spectrum is typically a spin forbidden triplet transition. This is the reason for it being a lot weaker than the absorption in the blue and UV range. The introduction of a heavy atom strengthens the spin-orbit coupling and hence increases the absorption strength of triplet transitions [105, 98]. We chose Os2172, which is shown on figure 4.3 [106]. It is very similar to Os-N3, but it has an absorption curve that fits better to our laser system.
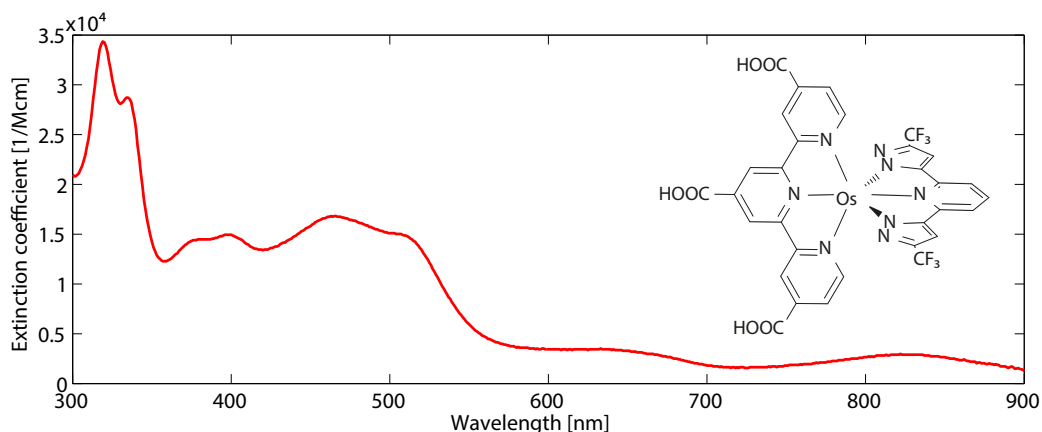
Figure 4.3: Os2172, another compound used for solar cell sensitization. The organic parts of the molecule are bound through coordination bindings with an osmium atom at its center. The presence of a heavy atom leads to stronger absorption bands in the NIR range through the the heavy atom effect. In addition, the absorption cross section in the XUV is higher for osmium than for ruthenium, as present in N3.

### 4.2.3 Sample Preparation

In the first step we cleaned the silicon substrate by sputtering and annealing in vacuum. The cleanliness was checked with X-ray Photoelectron Spectroscopy (XPS).

For the deposition of the molecule we chose a method that took the fragility of the molecule into account. We took a clean slide of Silicon in the (111) orientation and put a drop of ethanol containing $1.8 \times 10^{-3}$ M Os2172 on it. Then we waited for it to almost evaporate and put another drop on top and so forth. A typical preparation procedure involved roughly 30 to 50 drops. We put so many individual drops onto the surface because we wanted to be sure to have a thick layer of molecules on the sample for the first experiments. Once the thick layer is successfully detected we can move on to a controlled monolayer. We could not create a more concentrated solution due to the poor solubility of Os2172 in common solvents. The entire procedure was carried out in a fumehood, then the sample was transferred to vacuum.

## 4.3 Steady State Experiments

### 4.3.1 Direct Observation of the Metal Center: Os2172

#### X-Ray Photoelectron Spectroscopy of Os2172

In order to characterize the molecular layer on the sample we performed *X-ray Photoelectron Spectroscopy* (XPS) with an aluminum K-$\alpha$ cathode at 1486 eV [70]. The results are shown in figure 4.4. We can clearly identify the main peaks of the spectrum with the

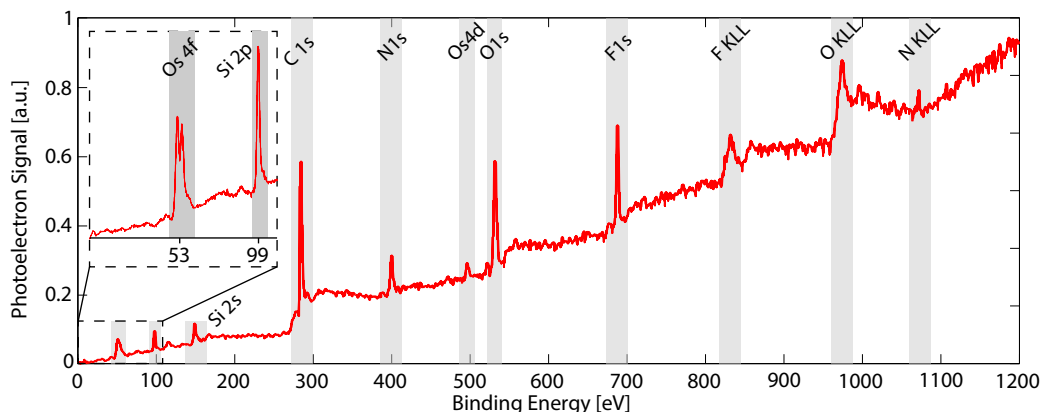Figure 4.4: XPS spectrum of Os2172 on Si(111) acquired with an Al K-$\alpha$ X-ray cathode at 1486 eV. The visible peaks are identified as the characteristic spectra of the constituents of the molecular adlayer. Hydrogen, whose absorption cross section is very low, cannot be detected in XPS.

help of research databases available online [71] and map them onto the constituents of our molecule. Typically this method is also used to check the cleanliness of a sample. It can easily detect small amounts of contamination on an otherwise flat background. This works very well for substrates without organic adlayers. In our case however it is more challenging to identify organic contaminants because the molecule that we deposited on the surface already has all the typical components of such compounds. We can however compare the peak areas corresponding to a molecular signal to those that might also be coming from a contaminant (such as the carbon 1s peak) and see whether the ratio between them matches the one we would expect from the stoichiometry of the molecule. In the case of drop-deposited Os2172 we have to make another concession. The thickness of the adlayer is very uneven – to the extent that this is clearly visible by the naked eye. At the same time we can still see a signal from the substrate core levels. So the adlayer is very thin in parts and very thick in others. As the mean free path for electrons changes with kinetic energy we would normally have to consider it when comparing the afore-mentioned peak areas at different kinetic energies. This is unfortunately not possible for the greatly varying layer thickness and will be neglected.

For Os2172 we compared the peak area of the carbon 1s at 285 eV level to that of fluorine 1s at 687 eV. Fluorine is not abundant in the laboratory environment and is used as a proxy for the molecule whereas carbon is a part of any organic contamination and serves as a proxy for a signal from both the molecule and the contamination layer. From the cross sections we would expect the ratio to be $(^{\text{C1s}}/_{\text{F1s}})_{\text{theory}} \approx 1.1$. In the measurement we get a ratio of $(^{\text{C1s}}/_{\text{F1s}})_{\text{experiment}} \approx 1.5$. This would mean that there is more carbon than expected on the surface, hinting at a contamination layer.
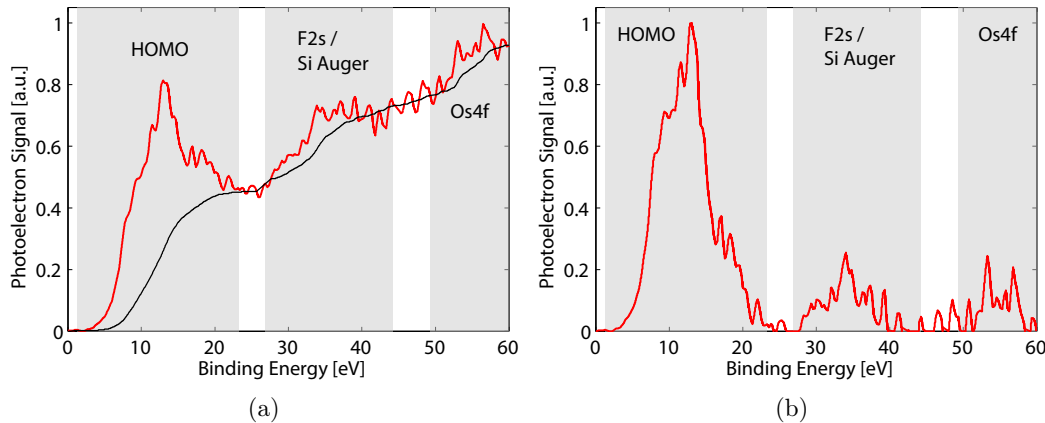
Figure 4.5: Photoelectron signal obtained from Os2172 on a Si(111) surface. The acquisition time was 3.5 h, the measurement was performed without an electrostatic lens in the detector. **a)** The red line is a obtained from the raw data with a sliding average over five points. This is justified because the energy resolution of our time of flight detector is much higher then the physical energy resolution in the experiment. Typically the resolution is limited by the bandwidth of the XUV mirror. The black line is the background subtracted from the signal. **b)** The signal with the background subtracted. Clearly the signal to noise ratio for the osmium peaks is too low for a time resolved experiment.

## XUV Experiments on Os2172

As a next step we performed experiments with our XUV source utilizing a mirror with a central energy of 124 eV and a width of 4 eV. This experiment was carried out with the FP2 laser system [65]. It is very similar to FP3, the only major difference being the fact that there is no second amplification stage and hence a lower pulse energy of about 400 µJ. The repetition rate is also lower, as mentioned above.

For the first step we did not shine any NIR onto the sample. In that sense we were performing an XPS measurement with an unusual source as opposed to a time resolved photoelectron experiment. The results are shown in figure 4.5. The data shown here were acquired without using the electrostatic lens of the detector. This lens greatly improves signal to noise ratio for a part of the spectrum, but it can also distort it and lead one to mistaking peaks produced by the electrostatic lens for actual signals. This is why we abstained from using it for the identification of our peaks. Even when we use the lens the signal is too weak for time resolved experiments.
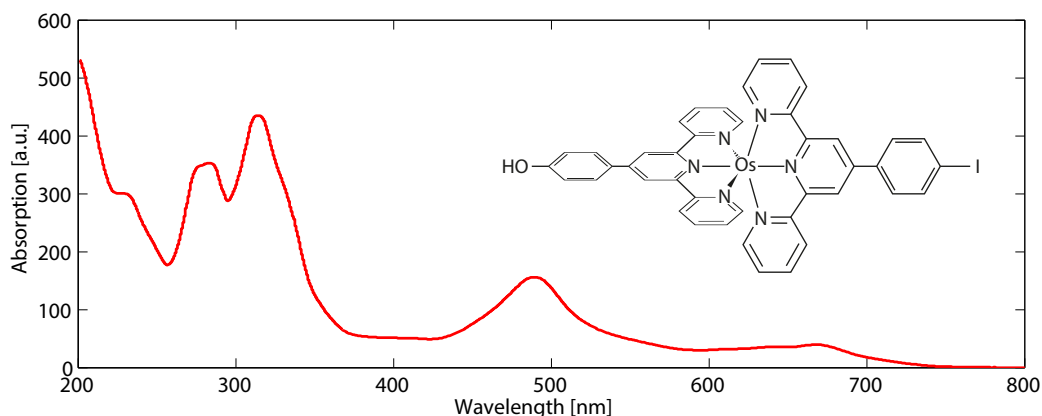
Figure 4.6: MBM4179, a compound specifically synthesized for time resolved experiments by Majewski and Wolf [107].

### 4.3.2 Iodine Tagging: MBM4179

We can see that is not possible to perform the desired experiments with Os2172 as a sample. Equally we can deduce that studying the metal center directly is unlikely to be possible since Osmium was already selected for its high cross section. There is another possibility to study charge rearrangement within such molecules: we can attach a *tag* atom to the molecule that has a core level with a high absorption cross section. Then we probe said core level and observe its chemical shift. Naturally the question arises whether such an extra atom would be affected by charge rearrangement and whether it would experience such an observable chemical shift. There have been reports on the successful detection of a shift on the order of $3\,\mathrm{eV}$ on a molecule tagged with iodine [15]. In this specific case there is no large spatial charge rearrangement in the molecule (as opposed to the previously considered case of a metal to ligand charge transfer), but the electronic configuration of the iodine atom is still sensitive enough to it to exhibit a detectable shift. So our next sample choice was a tagged molecule: *MBM4179*, shown in figure 4.6. It was synthesized for our experiments as part of a collaboration with Marek Majewski and Michael Wolf from the University of British Columbia [107]. The molecule is functionalized with a hydroxy group for surface attachment and a iodophenyl group for tagging. In its ground state the molecule is doubly positively charged. In order to counter this charge there are two negatively charged $PF_6$ molecules per MBM4179 present in the sample.

#### X-Ray Photoelectron Spectroscopy of MBM4179

We prepared the samples for our XUV photoelectron experiments in a way similar to Os2172 and performed an XPS measurement. This time the molecule was deposited from a $1 \times 10^{-4}\,\mathrm{M}$ acetonitrile solution with 40 drops. This yielded the data shown in figure 4.7. The XPS data also reveals the presence of the above mentioned counterions.
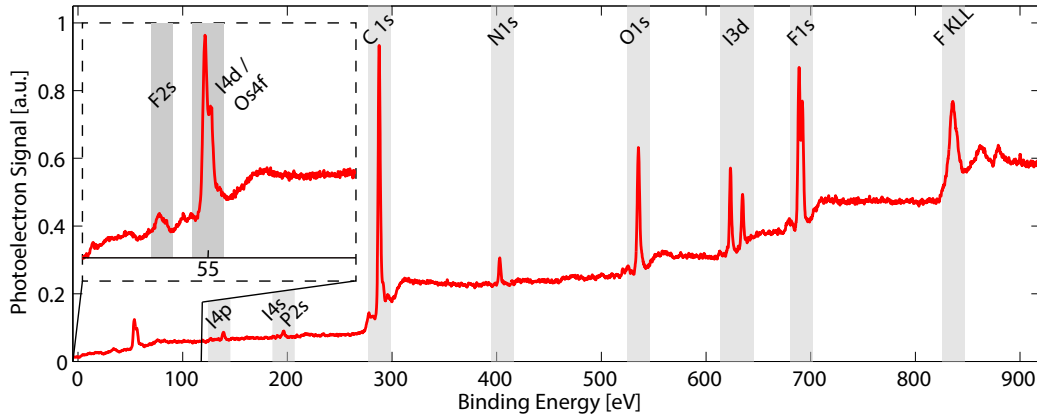
Figure 4.7: XPS data of MBM4179. The constituents of the molecule are clearly discernible. The F1s peak is split up in two. Since this is a level with an angular momentum of zero it cannot be a spin orbit splitting but rather a chemical shift. This indicates that the fluorine must be subect to two different surroundings – either binding to different atomic species or at different sites. The spin-orbit splitting of Os4f is not clearly visible anymore because the Os4f level overlaps with the I4d level. At 93 eV the cross section of Os4f will be roughly 17 times smaller than that of I4d and thus this will not be a problem for the actual experiment.

We compared the peak area of C1s as a proxy for a superposition of contamination and molecular signal to that of I3d (originating only from the molecule) to judge the cleanliness of the surface. The XPS data shows no peaks from the substrate so we can conclude that there is layer on top of the substrate which is thick enough for us to include the mean free path into our considerations as discussed for Os2172. The expected value from the cross sections and mean free path was $(^{C1s}/_{I3d})_{\text{theory}} \approx 0.7$, while the measured value was $(^{C1s}/_{F1s})_{\text{experiment}} \approx 2.2$. Here we can again clearly see from the higher carbon content that there is a contamination layer in addition to the deposited molecules.

## XUV Experiments on MBM 4179

Even if the sample can not be prepared in a clean way we can still learn something from it. When we expose it to XUV radiation we can try and find out whether the signal to noise ratio for the iodine 4d peak that we would be studying is high enough for time dependent experiments. If this is the case for a dirty sample then it is certainly true for a clean one. Just like for Os2172 we performed the measurement without an electrostatic lens in order not to change the spectrum in the observation. For these experiments we again used the AS3 beamline, but in this case we employed the FP3 laser system described in 2.2.1. Its repetition rate of 4 kHz is larger than that of FP2 with 3 kHz. Also its pulse energy is more than twice as high. This leads to much higher flux of XUV photons and to a cutoff

at higher photon energies. It is actually challenging to produce isolated XUV pulses at photon energies around or below 100 eV. When measuring with iodine tagged atoms it is however necessary to do so because its absorption cross section increases dramatically when reducing the photon energy (see figure 4.2). We chose a mirror at 93 eV with a width of 4.5 eV as a compromise between the cross section and the possibility of creating isolated pulses. In the measurements that we took we have seen strong modulation in the XUV photon spectrum in the energy range of our mirror so we are not working with isolated pulses. This does not change the validity of our experimental findings as we do not perform time dependent measurements in the first step.

An additional factor that needs to be considered is related to the central energy of the photoelectrons obtained from the I4d level. Its binding energy is roughly 55 eV. When we are working with 93 eV photons that yields a kinetic energy of 38 eV. This is already quite low and limits the intensity of a NIR pump pulse as the high energy edge the electron background can reach energies similar to that of the photoline and overwhelm the signal. So even if an isolated XUV pulse could be achieved at lower energies it is advisable to stay at energies around 90 eV in order to be able to pump efficiently.

The data we obtained is shown in figure 4.8. As is to be expected from the factors explained above (lower photon energy, higher NIR pulse energy, higher repetition rate, higher cross section) the acquisition time was significantly lower at six minutes compared to over three hours for Os2172. But in addition it is apparent that the iodine signal is much more discernible than the osmium signal was. It seems that even though the sample is not perfectly clean and there is probably a contamination layer the iodine cross section is high enough for a time resolved experiment.

The natural next step was to try a pump-probe experiment on the molecule. Even without isolated attosecond pulses it is possible to perform a time resolved experiment – it merely deteriorates the temporal resolution to the duration of the envelope of the pulse train as opposed to the duration of one single pulse. Unfortunately we were not able to see a time dependent signal. Possible reasons for the lack of signal included:

- Possible instability of the coordination binding when exposed to laser radiation at the intensities needed to see an excitation (we increased the intensity up slowly and scanned at different intensities without seeing a signal)

- Signal deterioration through the contamination layer

- Too small optical extinction of the molecule

With our next sample choice we aimed to remedy these points.

### 4.3.3 Iodine Tagging and Evaporation Deposition: Tetraiodo Copper Phthalocyanine

After learning that iodine tagging produces a detectable signal suitable for time dependent experiments and that a clean preparation scheme is very beneficial for the interpretation of any data we selected a molecule that fulfills our refined criteria: Tetra-Iodo
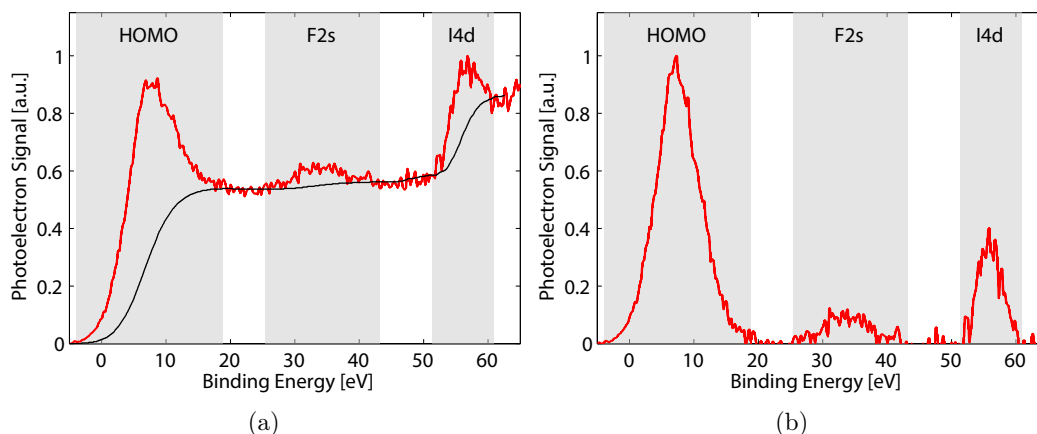
Figure 4.8: Photoelectron spectrum of MBM4179 on Si(111) obtained with XUV photons at 93 eV with a width of 4.5 eV. **a)** Spectrum with background **b)** Background subtracted. It is apparent that the signal to noise ratio and the signal to background ratio are sufficiently high for a time resolved experiment.

Copper Phthalocyanine ($I_4CuPc$), depicted in figure 4.9 along with its optical extinction coefficient in a dimethyl sulfoxide solution. In the previously used molecules the transitions of interest were metal to ligand charge transfers. The charge transfer lines on these molecules in the near infrared are spin forbidden and have a very low extinction coefficient of a few thousand $\frac{L\,cm}{mol}$ at most. This is not the case for $I_4CuPc$. The absorption line at 600 nm to 700 nm that overlaps with our light source corresponds to a transition between the $\Pi$-type HOMO and LUMO orbitals that are located on the aromatic ring [108]. This is potentially problematic since the charge density in the proximity of our iodine tags changes very little between HOMO and LUMO. Whether or not this change will be result in a detectable chemical shift remains to be determined.

In contrast to the molecules that we used in the previous experiments Phthalocyanines have a closed aromatic structure around the metal center. The aromatic part is not bound through coordination bindings to the metal center but through more stable covalent bindings. This makes it possible to evaporate Phthalocyanines and deposit them in a very clean and controlled way [109]. Whether or not this is true for the iodine tagged version that we are studying is a question that can and will be answered by scanning tunneling microscopy and scanning tunneling spectroscopy experiments [110].

## X-Ray Photoelectron Spectroscopy of $I_4CuPc$

Figure 4.10 shows an XPS spectrum of $I_4CuPc$ deposited on Si(111) via evaporation. When performing the same analysis as for the other two studied molecular species we chose to compare the peak areas of carbon 1s and iodine 3d. We would expect a ratio of $(^{C1s}/_{I3d})_{theory} \approx 0.2$, whereas we are seeing $(^{C1s}/_{I3d})_{experiment} \approx 0.025$. The iodine signal is one order of magnitude larger than expected. We also compared the iodine 3d level to the
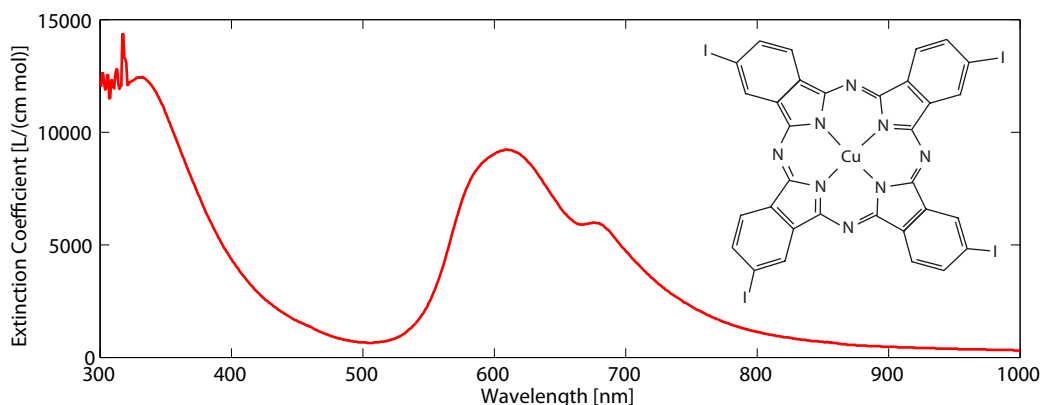
Figure 4.9: The optical absorption of tetraiodo copper phthalocyanine in dimethyl sulfoxide with a concentration of $1.44 \frac{\text{mmol}}{\text{L}}$. The strong absorption around $600\,\text{nm}$ corresponds to a HOMO-LUMO transition between $\Pi$-type orbitals on the organic ring [108]. Spectra courtesy of [111]. The inset shows the structure of $I_4CuPc$.

copper $2p^{1/2}$ level. The $2p^{3/2}$ peak overlaps with the iodine $3p^{1/2}$ peak. We adjusted the cross sections to account for the fact that we are only studying one of the two spin-orbit split levels. The expected result was $(^{I3d}/_{Cu2p})_{\text{theory}} \approx 5.4$ and the measurement yielded $(^{I3d}/_{Cu2p})_{\text{experiment}} \approx 6.4$. This is not exactly the stoichiometrically expected ratio but it is not nearly as far off as the ratio between carbon and iodine.

Combining the two comparisons tells us that there is no evidence for organic contamination on the sample – in contrast, there is a shortage of carbon. There might have been a contamination on the substrate from previous molecule preparations that could not be completely removed. When the sample is sputtered, the molecule can break apart and not all constituents stick to the surface in the same way.

### XUV Experiments on $I_4CuPc$

The first spectra of $I_4CuPc$ at a photon energy of $95\,\text{eV}$ are shown in figure 4.11. We cannot be certain that the large and well visible iodine peak exclusively stems from intact molecules, but it seems encouraging. Even if we can completely follow the XPS analysis and the molecular signal were one order of magnitude lower than measured here it would still be detectable. In addition it is possible to lower the photon energy even further and gain signal strength through the increasing cross section of iodine. At $90\,\text{eV}$ it is already $50\,\%$ higher and at $85\,\text{eV}$ it increased more than twofold compared to our current working point of $95\,\text{eV}$. This would make obtaining an isolated pulse more challenging, but it will still be feasible according to our experimental experience.

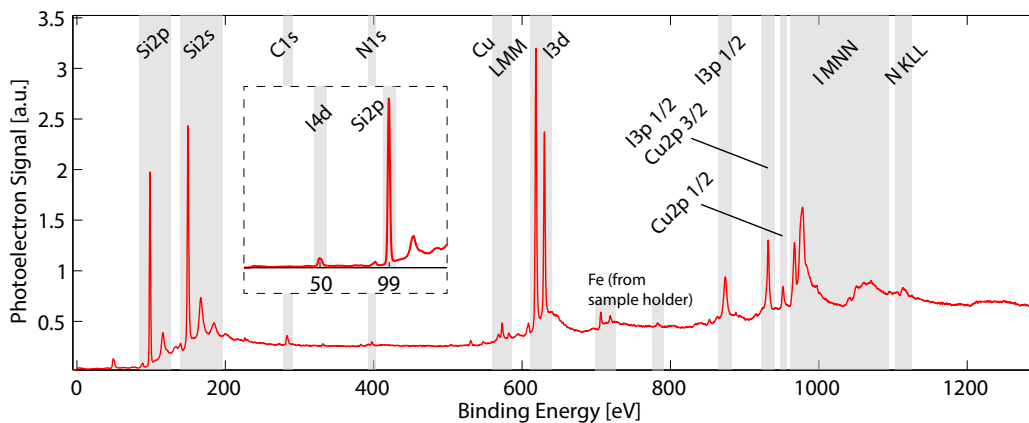Figure 4.10: XPS spectrum of I4CuPc deposited via evaporation in vacuum. The small peaks at $750\,\text{eV}$ and $800\,\text{eV}$ arise from the sample holder that contains steel.
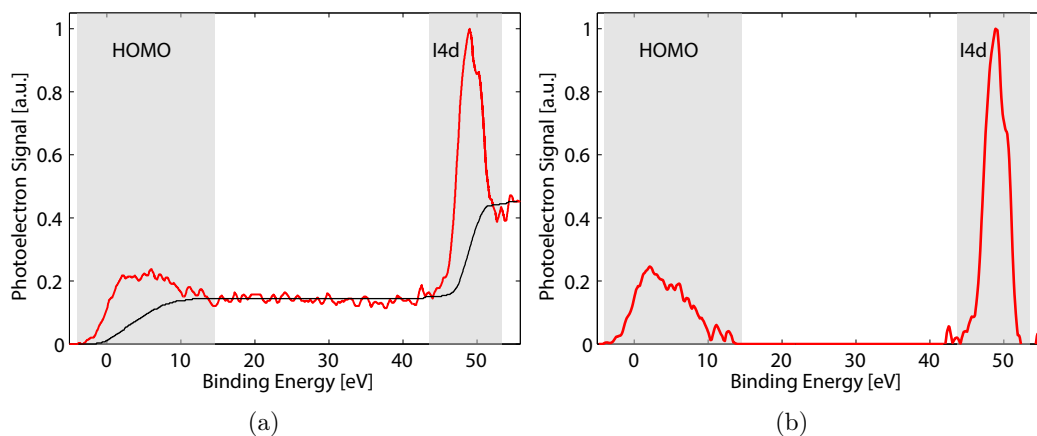


Figure 4.11: An XUV spectrum of I4CuPc acquired at a photon energy of $95\,\text{eV}$. This spectrum was acquired in merely three minutes without an electrostatic lens. Comparing this to Os2172 and MBM4179 demonstrates in stark contrast that the quadruple iodine tag in combination with a clean preparation scheme yields superior results. The signal is definitely strong enough for time resolved experiments.

## 4.4 Conclusions

We can draw these main conclusions from our experiments so far:

- The direct observation of a metal center in a thin layer of metal organic molecules is not possible with our setup. With a drastically increased XUV flux it could be an option in the future, but at the moment it is out of reach.

- An ex-situ preparation which involves removing the sample from vacuum and the depositing the molecular sample on it will result in a contamination of the sample. The influence of this contamination cannot easily be quantified.

- If we want to avoid contaminations in our samples we have to deposit them in vacuum. Evaporation, presenting the cleanest and most controlled option, is only possible for molecules that are not held together via coordination bindings to the central metal atom. This rules out a large subset of metal-organic molecules for our experiments.

- The observation of an iodine tag attached to a molecule is possible at photon energies around 90 eV.

## 4.5 Outlook

A challenge that has to be overcome is the clean and controlled preparation of an iodine-tagged phthalocyanine. In order to control all experimental parameters we do not only plan to perform XPS measurements but also scanning tunneling microscopy and scanning tunneling spectroscopy after a deposition through evaporation. With these techniques it is possible to determine the spatial orientation and structural integrity of molecular adlayers on semiconductors. Another possible problem lies in the hitherto unknown strength of the coupling between the orbitals involved in a $\Pi$–$\Pi^*$ transition with the iodine core levels. It is conceivable that a transition takes place but cannot be observed due to the large spatial separation between iodine tag and central $\Pi$-type electronic system. The experiments of Dachraoui et al. [15] do make it seem plausible, but an experimental proof has yet to be provided.

# Chapter 5

# Attosecond Delay Spectroscopy on Tungsten

Electronic transport in solids is a fundamental phenomenon that has a multitude of applications in electronics. The ongoing miniaturization of transistors leads to an increasing interest in electronic motion on the angstrom length scale. With the help of attosecond streaking we can monitor electronic transport through few atomic layers on an ultrashort timescale. In the past years the first first such findings of Cavalieri et al. [20] have been greatly refined. Here we present the extension of the streaking technique towards higher XUV photon energies and a summary of past measurements.

## 5.1 Principle of the Experiment

The basic idea of delay spectroscopy is an extension of the streaking method. As explained in section 2.1.3 this technique directly measures the vector potential of an intense pulse. In the discussion so far we have assumed that there is a target material that provides us with a state that we can photoionize to produce free electrons. But for some materials there is more than one state in the accessible energy range. If we photoionize two or more states in our experiment we get a curve resembling the vector potential for each of those states respectively. An example is given in figure 5.1. This data was acquired with XUV pulses centered at 145 eV with a spectral FWHM of 4.5 eV and a temporal duration of 480 as on a tungsten (110) surface. The two lines from the valence band and the 4f level are clearly discernible[1]. When we are streaking two lines both of the traces will represent the vector potential of the same NIR laser field. But there are still some things that can differ between the two. Since we are dealing with a solid here we have to consider whether the photoelectrons that we are studying are currently within the material or without. Inside the tungsten medium the streaking amplitude

---

[1] Actually there are more than two levels: the W4f is split up into $W4f_{5/2}$ and $W4f_{7/2}$. Both of these levels are split in a bulk and a surface contribution. There is also the additional W5p level very close by. But as all these levels are separated by less than the bandwidth of our XUV mirror (4.5 eV) the lines can not be easily separated any longer. In the analysis it is assumed that they have the same temporal structure for the TDSE evaluation. This is justified by the absence of interference between them. Since the W5p cross section is significantly smaller than that of W4f in the photon energy range discussed here we will refer to the photoline simply as the W4f line. A similar rationale applies to the other photoline that we will call the valence band from here on.
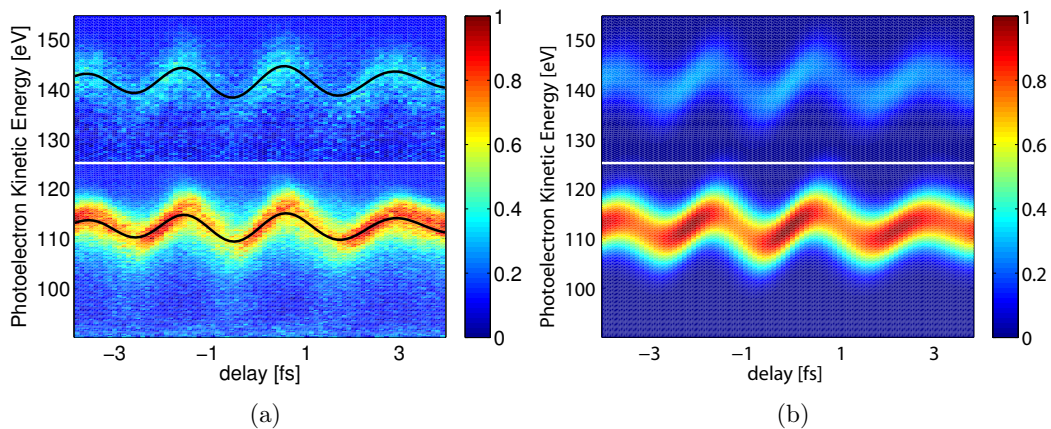
Figure 5.1: **a)** A streaking spectrogram of tungsten acquired with a central photon energy of 145 eV. The line at higher kinetic energies corresponds to the valence band while the line at lower kinetic energies corresponds to the 4f level of tungsten. The black line shows the result of a center of energy analysis. The white line denotes that above this line the spectrogram has been multiplied by 5 for better visibility. **b)** The reconstructed spectrogram, a result of a TDSE analysis of the data on the left. The chirp is qualitatively well reproduced in both lines. The challenge for both methods is in the discrepancy of signal strengths between the two lines. This will be discussed in detail in section 5.3.

will be reduced by a factor of $\approx 16$ [20]. Consequently, we are only effectively streaking electrons from the point in time when they reach the surface. If the electrons from the two different states leave the medium at different times they are exposed to a different field and their traces will be shifted on the delay axis with respect to each other.

This finding was first reported by Cavalieri et al. in 2007 [20], who discovered that the valence band emission in tungsten precedes the 4f core level emission in tungsten by $(110 \pm 70)$ as. This result was groundbreaking and opened the door for a number of possible theoretical explanations, which will be summarized in section 5.2. And yet the underlying data had major limitations: There is only one data point, generated by two measurements with relatively high uncertainty. The theoretical considerations yielded multiple possible physical origins of the delay that all fit this data point. In the last few years a series of experiments were performed that were designed to confirm or rule out the hypotheses provided by theory.

## 5.2 Theoretical Considerations

As mentioned in the previous section, there are a number of theoretical explanations for the measured delays in photoemission from solids so far. There have also been summaries of these publications in these sources: [69, 112]. The following table is intended to give a short and concise overview of the current status of calculations.

| Physical explanation for delay | Used methods, assumptions | results, prediction |
|---|---|---|
| CAVALIERI ET AL., 2007 [20] | | |
| Final state band structure within metal, different escape depths | Static band structure in excited state. Does not take photoexcitation into account: no selection rules and no transition probabilities for the individual transitions considered | Works for 90eV: predicts 90as |
| ZHANG AND THUMM, 2009 [113] | | |
| Interference effects in the 4f line due to photoemission from distinct depths. Valence band is delocalized and does not show this behaviour. | One step quantum mechanical photoionization calculation. Penetration depth of NIR much larger than escape depth of electrons | Delay depends on mean free path of 4f electrons, which changes with photon energy. |
| LEMELL ET AL., 2009 [114] | | |
| Group velocities, emission depths, scattering processes that slow VB electrons to 4f energy | Semiclassical Ansatz; classical transport theory with quantum scattering probabilities; influence of the NIR pulse on the primary photoexcitation process and local crystal-field effects on the emission time spectrum neglected | Predicts 42as delay at 90eV |
| KAZANSKY AND ECHENIQUE, 2009 [115] | | |
| Different localization characteristic for different initial states; no band structure effect because static band structure does not apply at these time scales | 1D TDSE; neglects hole in valence band | Predicts result at 90eV correctly within error margins: 85as |

| | | |
|---|---|---|
| KRASOVSKII, 2011 [116]<br>Final state effect caused by band structure | Assumes normal emission; 1D calculation | Strong variation with photon energy predicted |
| ZHANG AND THUMM, 2011 [117]<br>Different Localization characteristic for different initial states | Field penetration depth set to zero; 1D model surface with core potentials of different widths to represent localization | 120as at 90eV |
| NEPPL, 2012 [69]<br>Free electron transport | Free Electron- like dispersion assumed. Mean free paths from [99] | Predicts delay vs photon energy curve; delay too small at 95eV and a bit too small at 118eV; right for larger energies |
| BORISOV ET AL., 2013 [118]<br>Surface vs bulk: resonant emission in bulk vs nonresonant emission at surface; Amount of surface contribution to photoline plays large role in delay. | 1D model potentials with varying harmonics content which allows/forbids resonant interband transitions for core/valence levels | Explains experiments on Mg (see next paragraph); predicts right delay for W110 at 90 eV |

So far none of these publications is predicting our experiments precisely. Some of the identified problems include:

- Cavalieri et al., 2007 [20]:
  Offers a very simplistic approach that neglects the entire photoexcitation process.

- Zhang and Thumm, 2009 [113];
  Zhang and Thumm, 2011 [117] and
  Kazansky and Echenique, 2009 [115]:
  These studies conclude that the origin of the observed delay is given by different localization property of the initial states: a localized core state (4f) versus a delocalized valence band. If this were the case then it would have to occur also in other materials when comparing localized with delocalized levels. There has been a study on the (0001) surface of magnesium at a photon energy of 118 eV which found no appreciable delay between the delocalized valence band and the localized 2p level [69], even though the valence band of magnesium is delocalized to a higher degree than that of tungsten [119, 120]. In the free-electron metal magnesium the vanishing delay can be explained with free electron dispersion.

- Lemell et al., 2009 [114]:
  Provides a value for the delay at 90 eV that was inside the error bars for the very

first dataset of Cavalieri et al. It's prediction of 42 as is now safely outside the error bars.

- Neppl, 2012 [69]:
  Assumes free electron dispersion as the cause for the delay. The predicted delay versus photon energy is shown in figure 5.2. It evidently does not match the experimental data.

- Borisov et al., 2013 [118]:
  The main finding here is given by the idea that the ratio between emission from surface states and bulk states determines the delay. The measurements for W(110) at 90 eV and for Mg (0001) at 118 eV can be reproduced. This is a promising approach. It should be considered that there have been measurements on clean tungsten (110) with an added layer of hydrogen [112], which report a very similar delay value to clean tungsten. There are reports claiming that the adlayer strongly reduces the contribution of surface states to the photoemission [121]. This analysis of Feuerbacher and Fitton is likely incomplete since it only takes surface states into account that emit perpendicularly to the surface. Angularly resolved studies show that the hydrogen layer shifts the surface state photoemission towards the edges of the Brillouin zone [122]. Since we are integrating over a large angle of ca. $\pm20°$ we can still detect those states.

- Krasovskii, 2011 [116]:
  Concludes that the effect is caused by a final state effect: the band structure of W(110) above the Fermi edge. It predicts a much smaller delay for measurements at 105 eV than at 90 eV. This has not been observed experimentally. In addition there have also been measurements on a different crystal orientation of tungsten: W(100) at 105 eV. Since the band structure depends on the orientation, the delay should also vary between these two samples – but it is not measurably different between W(100) and W(110).

It is evident that the attosecond dynamics of tungsten still pose a conundrum and no single theoretical ansatz was able to fully explain them.

## 5.3 Past Measurements on Tungsten and O/W

The W(110) surface has been extensively studied at the Max–Planck–Institute for Quantum optics for several years. In this work we have built on the gathered experience, used the same sample preparation techniques that have been reported by Neppl [69] and will report on them only briefly. For the clean surface we performed alternating sputtering and annealing cycles after bringing the sample to vacuum. That leaves mostly carbon as a possible contaminant, which is removed by flashing the sample to 2400 K in an oxygen atmosphere. This makes the carbon desorb as carbon monoxide. Then the sample is flashed to 2400 K again to get rid of possible oxygen remnants. We also performed measurements on an oxygen overlayer in the $(1 \times 1)$ reconstruction on tungsten. This
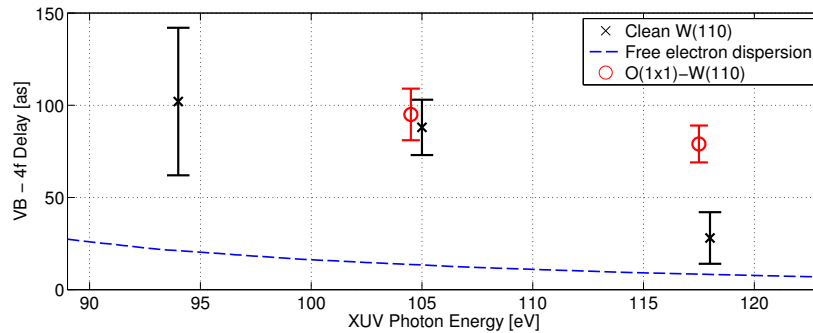
Figure 5.2: An overview of the measurements on clean W(110) and O/W that have been performed prior to this thesis. It seems like the delay is sloping downwards as the photon energy of the XUV beam is increased. The error bars represent the standard deviation of the data. The delay calculation for W(110) assuming free electron dispersion in the metal is shown as the blue dashed line. A positive number in the delay indicates that the valence band electrons arrive first [69, 123].
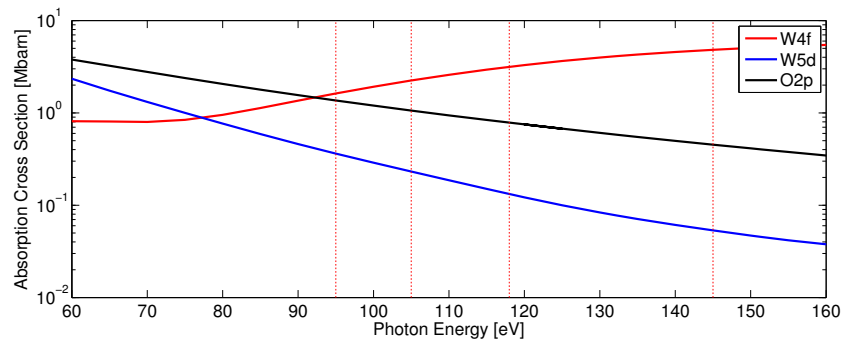


Figure 5.3: The cross sections of the relevant levels for tungsten delay spectroscopy: W4f and W5d/O2p (the chief contributions to the valence band of the clean tungsten and O/W surfaces). These values are calculated and not necessarily applicable to the highly surface sensitive spectra that we are acquiring. They will however reproduce the general trend quite well, which is sufficient to support our argument. On the logarithmic scale of the absorption cross section it becomes apparent that observing both tungsten levels simultaneously gets increasingly difficult at higher photon energies. The cross section of O2p dominates the valence band line of O/W for the energy range relevant to our application. Measurements have been performed at the photon energies that are indicated as dotted lines [102, 101].

will be referred to as *O/W* from here on. For its preparation we expose the sample to an oxygen atmosphere of $1 \times 10^{-5}$ mbar for 10 minutes after the standard cleaning steps.

Figure 5.2 shows the available data points on the photoemission delay of W(110) and O/W before the implementation of the FP3 laser system. From these points we would have to assume the delay to steadily decrease with increasing energy – possibly with a linear or quadratic slope. This would hint at a relatively simple explanation as opposed to a band structure effect that could be expected to exhibit a more complex dependence. But this is simply caused by the low number of data points, not by their values. In order to provide a better data basis for theoretical explanations we looked into the feasibility of more scans at different photon energies. There are three main obstacles to overcome for this endeavor:

- The cross section of tungsten must be high enough over the entire range for an experiment.

- The cross sections of the two involved photolines must not differ by too much. Figure 5.3 shows how the relevant cross sections change with photon energy. Towards lower energies the cross sections are similar and both high enough for experiments. Conversely, increasing the photon energy severely reduces the cross section of the valence band. At 145 eV the difference between the two lines is already a factor of 100. It is challenging to simultaneously measure two lines that differ by this much in their signal strength. The specific challenges of this measurement will be shown in section 5.4

- The isolated XUV photons must be produced with our high harmonic generation setup. With the standard Femtopower laser systems the XUV range in which one can generate enough photons for a time dependent experiment extends from 90 eV to 135 eV. At the edges of this range it gets exceedingly difficult to produce an adequate number of isolated photons – at the lower end one typically produces pulse trains and at the higher end there are no more photons. With the newly implemented booster system it is possible to extend this range to higher energies, as will be discussed in section 5.4.

For the measurements on O/W the situation is different. Here the cross sections are not diverging as fast as for the clean metal. But the data interpretation is more complicated due to the layered structure of the sample. The emission from the oxygen adlayer and the top tungsten layer are not distinguishable since the valence orbitals of both elements are responsible for the binding and form overlapping bands [69, 124]. Qualitatively the larger delay values for O/W than for clean W(110) can be explained by two factors: the emission depth and the temporal effect of the charge density at the O/W interface. The cross section for the O/W valence band is dominated by the surface contribution of the adlayer and the top tungsten layer whereas the 4f electrons can only emerge from the interface or below. This shifts the center of gravity of the emergence of valence band photoelectrons closer to the surface and makes them arrive earlier in the streaking
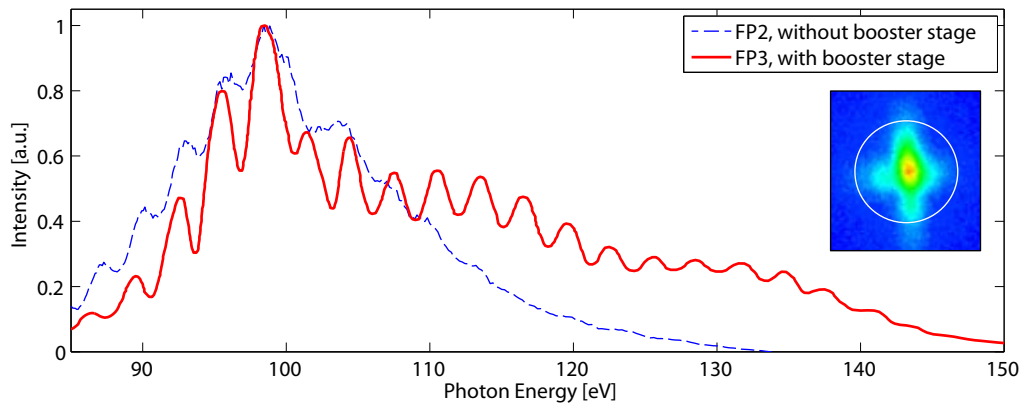
Figure 5.4: Typical XUV spectra for a Femtopower based system without a booster stage (FP2, blue dashed line) and with a booster stage (FP3, red line, see figure 2.5). Both spectra have been normalized. The experimentally usable photon energies for the booster system extend up to $\approx 150\,\mathrm{eV}$. The inset shows the beam profile as recorded on the MCP detector behind the experimental chamber of AS3 (see figure 2.10). The white ring indicates the circumference of the pellicle/wirecross filter in the final chamber of the AS3 beamline (see figure 2.9). The part of the mode that passes through this filter is usable in the experiment. Evidently almost the entire intensity is captured within this aperture.

field. Additionally the short binding length of O/W [2] leads to a higher charge density at the interface that affects the temporal properties of the emitted electrons. This is hard to quantify but it will affect the slower electrons from the 4f levels more strongly and delay them further. The higher delay values for the O/W measurements than for clean tungsten confirm these expectations.

## 5.4 Production and Characterization of High Harmonics at 145eV

As mentioned in the previous section the interpretation of our experiments on tungsten would greatly benefit from a data point at higher XUV photon energy. According to equation 2.6 the higher pulse energy provided by an additional booster stage in FP3 should translate to an increase in photon energy. Whether or not the calculated parameters can actually be reached experimentally is a more difficult question, since the pulse length varies between the laser systems and the response of the neon gas used for high

---

[2] Roughly 1 Å for the O/W bond compared to the tungsten lattice constant of roughly 3 Å. In the bcc crystal of tungsten this translates to a next neighbor distance of $\approx 2.6$ Å.

harmonic generation is complex. The output of FP3 is not as well compressed as the one of FP2[3] and hence the present slight pre-pulse contributes to ionization of the target medium, which greatly diminishes the XUV yield of following laser cycles. Also the non-optimal compression reduces the maximally achievable electric field, which in turn limits the XUV photon energy. Our experimental findings are shown in figure 5.4. We focused the beam with a spherical mirror with a focal length of 60 cm into a quasistatic gas cell containing 200 mbar Neon gas and optimized the spectrum on the high energy end. The FP2 spectrum was obtained with a 40 cm focusing length and similar gas pressure. Here we can see that the standard Femtopower systems are not able to generate intense harmonics above 130 eV. It is challenging, but possible to perform streaking spectroscopy with these lasers on tungsten surfaces at 135 eV – albeit at reduced count rates. For measurements at higher energies, the booster system of FP3 enables an extension of the range by roughly 15 eV up to $\approx$ 150 eV. We chose a compromise between photon number and energy by utilizing an XUV mirror at 145 eV with a spectral FWHM of 4.5 eV. This would support an XUV pulse length of 400 as if there was no dispersion. Comparing the absolute count rates between the systems is challenging. The XUV beam has to pass through filters and is reflected off mirrors at grazing incidence. These optical elements frequently deteriorate when we expose them to intense laser radiation. Such a deterioration can easily diminish the XUV flux by 30 % to 50 % for one optical element. For a reliable measurement one would have to compare the two different laser systems in the same beamline in direct succession, which was not done. FP3 drastically improves the electron count rates for high photon energies above 120 eV. This is due to the higher total energy that allows us to employ longer focusing lengths and larger beam diameters at the high harmonic generation. In this way we can reach the optimum intensity in a larger volume and create more XUV light. The total count rates are also improved simply by the higher repetition rate of FP3: It runs at 4 kHz compared to the 3 kHz of FP2. Another remarkable property of the created harmonics is their stability. In typical performance we measured around 1 % RMS intensity fluctuation over a time of one second.

## 5.5 Delay Spectroscopy of Tungsten and O/W at a Photon Energy of 145eV

### 5.5.1 Clean Tungsten 110

The cross sections predict the photolines of W4f and valence band to significantly differ in intensity. In the static spectrum shown in figure 5.5 this is experimentally reproduced. The two depicted spectra were acquired in direct succession with only one difference: we increased the voltage at the multichannel plate (MCP) of our detector from the blue spectrum to the red one. This increases the detection efficiency and improves signal to

---

[3]Approximately 5.5 fs for FP3 versus < 4 fs for FP2. The cycle length for our central wavelength is 2.5 fs so a full compression would push us below two cycles and should have a great effect.
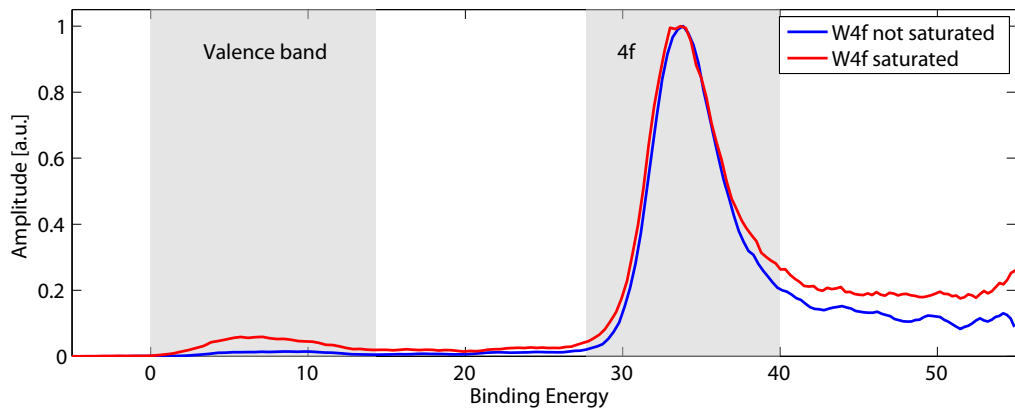
Figure 5.5: Two spectra of W(110) acquired in direct succession. The only difference between the two was the voltage applied to the multichannel plate at the TOF detector – it was increased for the scan shown in red. The spectra are normalized to the height of the W4f peak. From the change in relative peak height between the two spectra one can deduct that the 4f peak is in fact saturated in the red curve, even if it is not apparent from the peak shape.

noise ratio[4]. Both spectra were normalized to the highest peak. Since the ratio of peak heights of valence band and 4f changes with the applied voltage between the two spectra we can conclude that the 4f peak is saturated in the red spectrum. This is not obvious from the peak shape and has some repercussions on the data evaluation. The peak height of the valence band in the blue spectrum is not sufficient for a delay retrieval. So we have to work in slight saturation to extract the information we are interested in. It has been shown that non-drastic saturation (not affecting the peak shape) does not change the delay [69], so the main goal of our experiment will not be affected.

We performed 132 measurements over the course of 11 (successful) measurement days. Some scans had to be discarded because the ATI electron background was too close to the 4f photoline. This is not a problem if there is absolutely no light on the inner part of the concentric mirror pair that produces the delay. But if there is some NIR light reflected from both mirror parts then they will interfere on the surface and there will be a trace in the ATI signal that is similar to an interferometric autocorrelation. This would produce a time dependent space charge on the sample that can change the streaking traces.

We applied a TDSE retrieval algorithm (see section 2.1.3) to the data and found that on average the valence band electrons arrive in the streaking field $(2 \pm 35)\,\text{as}$[5] earlier. In our sign convention this is defined as positive delay. Additionally we attempted to confirm

---

[4]Of course this only works up to the point where essentially all electrons impinging onto the MCP are being detected. If the voltage is increased further the only thing that is left to be amplified is noise and the signal deteriorates

[5]The error given here is the standard deviation of the data.

that saturation does not play a large role by studying only a subset of the scans where the integrated counts over the W4f line are below 2000 per second. This is equal to half the repetition rate of the excitation source. Reducing the count rate further would result in a non retrievable line from the valence band. For the subset of 59 scans with reduced count rates the retrieved delay is $(-2 \pm 27)$ as. The deviation of 4 as is much smaller than the statistical spread and we can confirm that saturation does indeed not play a role for delay retrievals. There was no correlation between the streaking intensity and the retrieved delay. The median intensity was $7 \times 10^{10} \, \text{W/cm}^2$, which is well below the damage threshold of tungsten [69].

A chirp extraction for both levels simultaneously from the same set of measurements is much more challenging. Since a chirped XUV pulse leads to a modulation of the peak height the chirp retrieval will be directly and strongly affected by saturation. We have to saturate the 4f line in order to even properly detect the valence band and thus we cannot retrieve the chirp for both lines at the same time at high XUV photon energies. It is however possible to obtain the chirps for the respective levels one at a time: we study the 4f line for scans with low count rates and the valence band chirp for those with high count rates. The retrieved chirp will be a combination of the contributions from the material and the XUV pulse. While the chirp of the pulse will strongly depend on the creation process and can differ from day to day the material contribution should stay constant. In an attempt to determine its value we performed measurements on the tungsten surface and on neon gas alternately. We expected to detect a constant shift between the two values that would then represent the material contribution. Unfortunately no such shift could be seen. This result is shown in figure 5.6. The difference between chirps from the neon and tungsten data do not even have the same sign. It might be possible to perform this type of measurement with a large database to provide sufficient statistics, but with the state of the art in streaking measurements this is a challenging endeavor. In general the retrieval from the valence band is less reliable due to the low count rates. An additional problem arising for this experiment is the positioning reproducibility of the solid state target in the streaking field. When switching between samples we have to remove the solid by several millimeters and then bring it back into the beam after the gas phase scans. The short focal length of 12.5 cm of the double mirror translates to a very sharp focus. This leads to the electric field changing rapidly spatially: in magnitude as well as Gouy phase. Due to the Donut shape of our outer mirror which focuses the NIR light in the concentric double mirror assembly it also changes its shape much more than a pure gaussian beam. This situation could be simplified by using a mirror with a longer focal length.

The data analysis revealed that there is a correlation between the retrieved chirp and the delay. This was also found by Kim [123], who notes that a retrieval algorithm very similar to ours can produce erroneous results in the delay for chirp values greater than $11 \, \text{fs}^{-2}$. The retrieved delay can be wrong by several tens of attoseconds. We reviewed the results of our own retrieval software with simulated data in the chirp range $-10$ as to 10 as and a vanishing delay. We found that there is no clear correlation between chirp and delay for these chirp values. In order to confirm this we checked the correlation
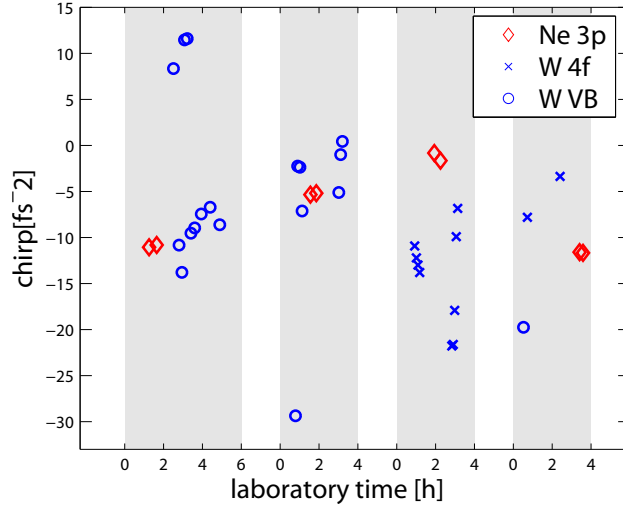
Figure 5.6: The retrieved chirp of the wavepackets emerging from the tungsten surface and a Neon gas. The horizontal axis indicates the time that it takes to perform the measurement, not the time of day. All scans in a day (indicated by the gray shading) were performed in direct succession while keeping the CE phase constant. For the sample switch we have to remove the solid tungsten and bring in a gas needle or the other way around. This process takes roughly 20 minutes. An entire series of scans on both systems takes roughly four hours. For the scans with more than 2000 counts in the W4f line we studied the retrieved chirp for the valence band since the W4f chirp retrieval would be affected by saturation. Also, a strong W4f translates to enough counts in the valence band for a retrieval. For the scans with less than this threshold we applied the reverse rationale. It is apparent that there is no clear offset between tungsten 4f, valence band and neon chirp values.
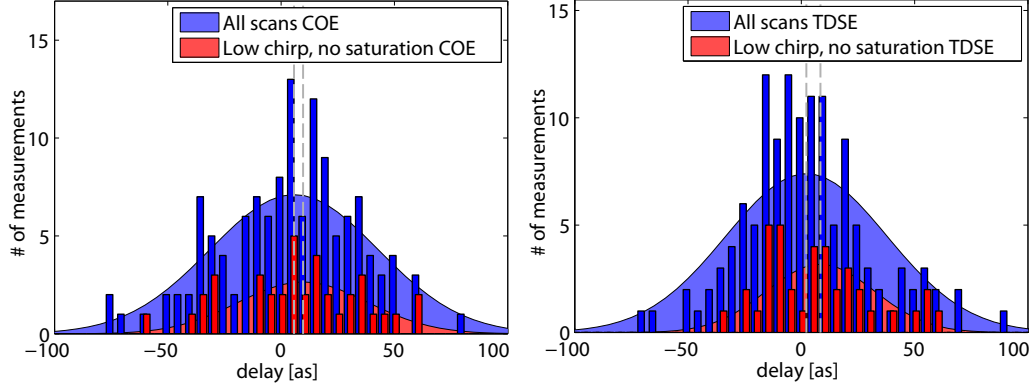
Figure 5.7: The dataset of all evaluated scans and the subset below the critical chirp absolute value of $13\,\mathrm{fs}^{-2}$. The area graph represents a normal distribution with the width and mean value of the corresponding data. The retrieved mean values for the delay in the respective subset and evaluation method are indicated as dashed lines. For all the subsets and evaluation methods the retrieved values are well within the error bars of all other subsets. A detailed discussion is given in 5.4.

between retrieved chirp and delay in the measured data. A trustworthy chirp retrieval in the 4f line is only possible for scans that are not saturated so we excluded scans with more than 2000 counts in the W4f line. Among these data points we found that the scans with a chirp absolute value smaller than $13\,\mathrm{fs}^{-2}$ showed no correlation between chirp and delay. The mean delay value for this subset was $(8 \pm 24)\,\mathrm{as}$, which is within one third of the standard deviation from the value for all scans, $(2 \pm 35)\,\mathrm{as}$.

As a further check on the performance of our retrieval we evaluated the data with the center of energy method and found very similar results. The histograms for all of the just mentioned subsets are shown in figure 5.7. The retrieved values for the just mentioned subsets are:

| Subset | Delay | Number of Scans |
|---|---:|---:|
| All scans | $(2 \pm 35)\,\mathrm{as}$ | 132 |
| All scans, COE | $(6 \pm 37)\,\mathrm{as}$ | 132 |
| No saturation | $(-2 \pm 27)\,\mathrm{as}$ | 59 |
| Low chirp | $(10 \pm 31)\,\mathrm{as}$ | 101 |
| Low chirp, no saturation | $(8 \pm 24)\,\mathrm{as}$ | 38 |
| Low chirp, no saturation, COE | $(10 \pm 29)\,\mathrm{as}$ | 38 |

## 5.5.2 Clean Tungsten 100

We performed additional measurements on tungsten at a different crystal orientation. Gathering data on the same material means that we are probing a system with the same cross sections, escape depths and localization properties but a different band structure. The crystal is cleaned in a similar procedure as W(110) in UHV and the measurement performed in the same way. The histogram of our delay findings is shown in figure 5.8. For these data there remains a weak correlation[6] for all chirp values. When we are studying only the spectrograms that are not saturated we are left with just 10 out of the 40 performed scans, so the applicability of statistical terms becomes questionable. We saw that the COE results scattered heavily with a result of $(42 \pm 55)$ as, so we scrutinized the data with another method: the ATTOGRAM algorithm by Justin Gagnon [44, 125]. This algorithm performs a full FROG retrieval of the spectrogram while assuming that there is just one state to be ionized. If it is applied to the tungsten data it will assume that the XUV pulse consists of two spectrally separated pulses in order to reproduce the W4f and valence band line. Since this is a FROG retrieval it yields the phase of the XUV pulse. From this phase one can calculate the group delay – and the difference between the group delay in the W4f and VB line corresponds to the emission delay we are interested in. This analysis was first applied by Schultze et al. [19]. Here it was performed by Johann Riemensberger. The retrieved delay values for all methods are:

| Subset | Delay | Number of Scans |
|---|---:|---:|
| All scans, TDSE | $(-13 \pm 30)$ as | 40 |
| All scans, COE | $(-17 \pm 37)$ as | 40 |
| All scans, Attogram | $(5 \pm 24)$ as | 36 |
| No Saturation | $(-17 \pm 37)$ as | 10 |

Four scans had to be excluded from the Attogram retrieval as the algorithm did not converge. All methods and subsets yield results that are within one standard deviation of each other.

## 5.5.3 Measurements on O/W

As mentioned in the preceding sections a chirp retrieval for the valence band is a difficult endeavor due to the low signal strength. Increasing it would also mean saturation in the 4f line, making an analysis of the chirp in the 4f line impossible – while still leaving the valence band signal quite low for a reliable chirp retrieval. For the O/W system the situation is different: the cross section of the valence band is now larger and allows for a more trustworthy analysis (see figure 5.9). On the other hand the retrieved chirp values would be more difficult to interpret since the valence band is now comprised of two atomic species. We thus focused our efforts on the delay measurement. We slightly saturated

---

[6]The probability that the observed distribution occurs by chance is roughly $20\,\%$. Usually one would speak of a correlation if this probability is below $5\,\%$
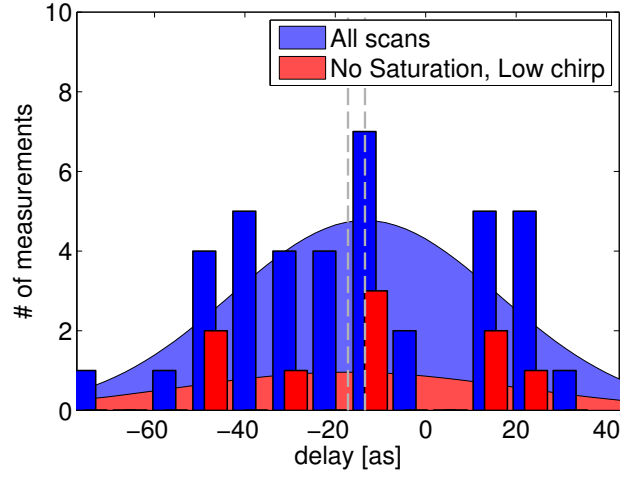
Figure 5.8: A histogram of all acquired data on tungsten in the 100 orientation at 145 eV compared to the selected scans that were not saturated and had less than 15 fs$^{-2}$ chirp. Note that the graph is not centered at zero but at the mean value of the unsaturated scans: $(-17 \pm 37)$ as
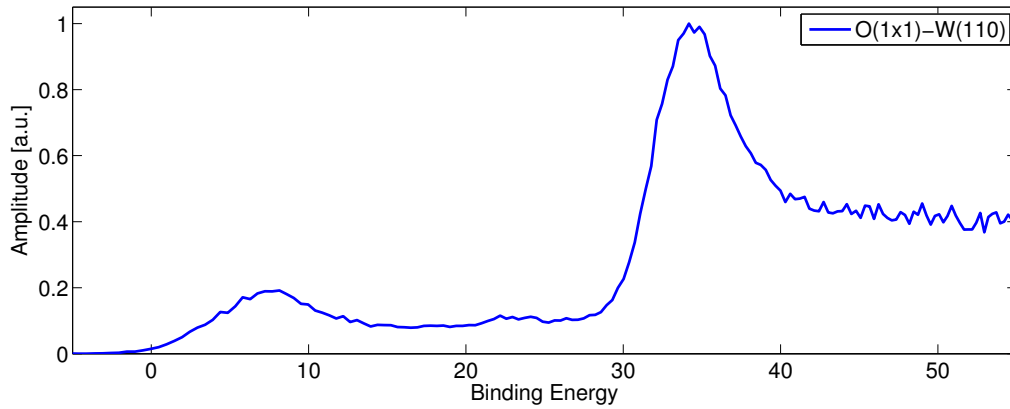


Figure 5.9: A static spectrum of oxygen on tungsten (110) acquired with a 145 eV mirror with a FWHM of 4.5 eV. Compared to the static spectrum for clean tungsten (see figure 5.5) it is apparent that the valence band region yields a much stronger signal, as expected from the cross sections.
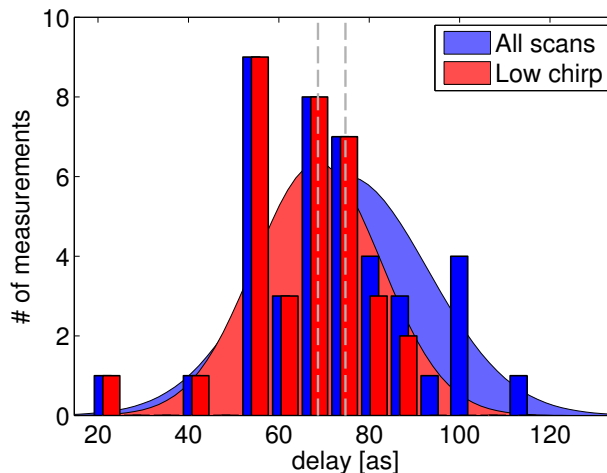
Figure 5.10: A histogram of all delay measurements on W/O at 145 eV photon energy. The retrieval yields a mean delay of $(75 \pm 19)$ as. As with the data for clean W(110), the red dashed line represents a normal distribution with the width and standard deviation of the data.

a large part of the scans, knowing that this would not affect the delay and improve the data quality of the valence band line. With this approach we can retrieve the chirp for one of the lines in all scans while reliably extracting the most important observable to us: the delay. Just as for the clean metal surface, there is a correlation between chirp and delay for large chirp values. This correlation vanishes below an absolute value of $7 \, \text{fs}^{-2}$, when we discard 8 out of 42 scans. The retrieved delays for both algorithms and subsets are:

| Subset | Delay | Number of Scans |
|---|---|---|
| All scans | $(75 \pm 19)$ as | 42 |
| All scans, COE | $(65 \pm 21)$ as | 42 |
| Low chirp | $(69 \pm 14)$ as | 34 |
| Low chirp, COE | $(58 \pm 17)$ as | 34 |

And as for the clean W(110) surface the retrieved delay values are all within a standard deviation of each other (see figure 5.10 for the histogram). We can also confirm the qualitative argument for the delay magnitude made in section 5.3. The delay for the layered system does not change as strongly as the clean surface, which also seems to confirm that the layered nature of the sample is a main contributor to the magnitude of the delay as opposed to a band structure effect in the final state which would change more strongly with photon energy.

## 5.6 Overview of Delay Measurements on Tungsten

In figure 5.11 the results of all delay measurements on clean tungsten (110), tungsten (100), tungsten (110) with an oxygen adlayer and tungsten (110) with a hydrogen adlayer are shown. Comparing this graph to figure 5.2 emphasizes the new trend in the data. Before the measurements at high photon energies we had to presume an ongoing drop in the delay for increasing XUV photon energies. But the new data points reveal a peculiar behavior for clean tungsten. The delay change with increasing photon energy starts at a relatively flat slope of $\approx 1\,\frac{as}{eV}$ for the low energy side, then quadruples between $105\,eV$ and $118\,eV$ and then reverts back to the flat slope. With the additional data point at higher energies we can now see that there is not an ongoing drop increasing in steepness but actually a step in the delay. The data confirms that this is not only the case for the (110) orientation but also for the (100) orientation of tungsten. The band structure differs between these two crystal faces, but the localization, surface to bulk ratio and escape depth do not. This makes a band structure effect unlikely as a cause of the measured delay. As mentioned in section 5.2 it is possible that the calculations emphasizing the contrast between surface and bulk emission as the leading cause for the delay are not contradicted by our findings on H/W. The experiments yielded a negligible difference between emission from tungsten 110 with and without a hydrogen adlayer at $105\,eV$. If the hydrogen merely rearranges the emission in the Brillouin zone towards larger k-vectors in the surface plane we would still observe surface states even if their emission is strongly reduced in the direction perpendicularly to the surface. It is possible to test this behavior with our setup by comparing scans that were obtained with and without the electrostatic lens of the TOF detector. Without the lens the system has a collection angle of ca. $\pm 2°$. This is increased tenfold to ca. $\pm 20°$ while using the lens and changes the angular characteristics of the recorded photoelectrons significantly.

## 5.7 Conclusions

We have shown that it is possible to extend the streaking method for photoemission delay measurements to photon energies of $145\,eV$ with a laser system based on CPA stages and a hollow core fiber. The currently maximally achievable photon energy with enough flux for photoelectron experiments on solids is around $150\,eV$. It is likely that this energy will increase as soon as the pulses are completely compressed to the sub $4\,fs$ range that is already the standard mode of operation for the laser system without the booster stage. Delay measurements between the 4f core and valence levels have been performed at the highest photon energy possible so far. These measurements have revealed that the band structure is unlikely to be the origin of the delay. At the short mean free paths that are typical for our experiments the photoelectrons originate from the first few layers of the solid, where they spend only around $100\,as$ before being streaked. Our data could potentially be the first step towards experimentally identifying a lower bound for the time it takes to establish a band structure in a solid. Another possible interpretation hinges
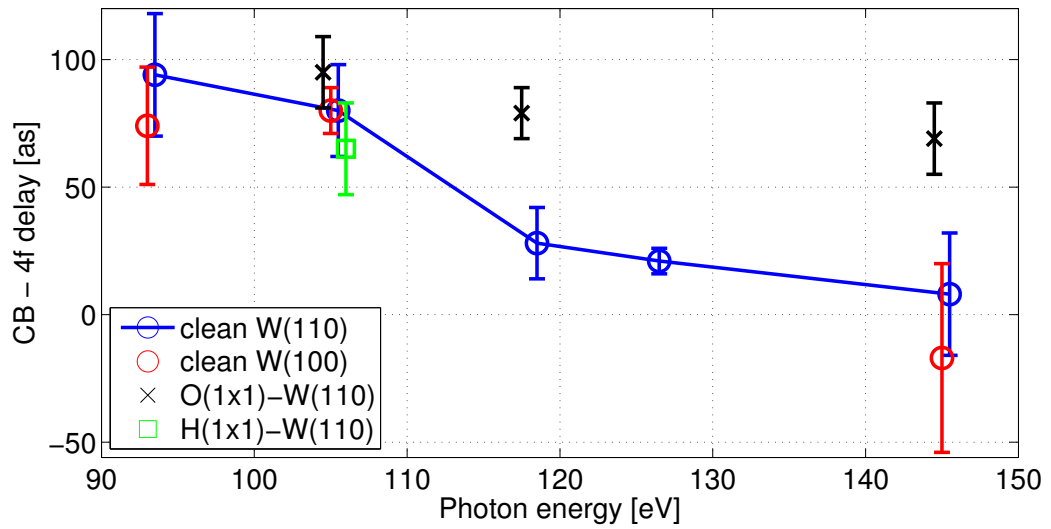
Figure 5.11: An overview of all the streaking measurements performed on tungsten at two crystal orientations, oxygen on tungsten and hydrogen on tungsten at central XUV energies of 93 eV, 105 eV, 118 eV, 126 eV and 145 eV. Some points have been slightly offset for clarity. The measurement at 126 eV has such small error bars because there are only four data points in this set that were all performed on the same day. The intra-day variation is typically significantly smaller than the inter-day fluctuation and we thus have to take this particular data point with a grain of salt.

on the fact that we are integrating over a large angular range with our detector. This could smear out the band structure effects and lead to only very small delays that would be smaller than the statistical spread of the data. The effect of angular integration can be measured by comparing delay scans that were obtained with and without the electrostatic lens of the TOF detector. It can also be quantified by performing streaking measurements with the hemispherical detector, which has an angular resolution.

We have observed a correlation between chirp and delay in our data for sufficiently large chirp values. For the analysis as it is being performed now we can rule out a systematic error in the retrieval software as we were able to prove by means of simulated data. Also we were able to draw our conclusions about the delay from a subset of data that does not show this correlation. But there might be a physical origin of this behavior. Sabbar, Heuser, and Boge recently reported on a measurement comparing the photoemission delays of neon and argon with chirped XUV pulses [126]. In the presence of chirp in the XUV there is a relation between the instantaneous frequency (i.e. photon energy) and the arrival time of the XUV photons. Since there is also a relation between the absorption cross section and the photon energy the arrival time of specific frequencies is being matched to the emission time. In their report Sabbar, Heuser, and Boge are working close to a dominant spectral feature in argon that strongly modulates the cross section. It varies by more than $80\,\%$ over the relevant bandwidth, which translates to a large chirp induced delay shift of over $100\,\text{as}$. In our case the cross sections vary by much less – only $4\,\%$ for the W4f and $14\,\%$ for the valence band. We would expect a much smaller effect that can be buried in the statistical noise for small chirp values. As the W4f cross section increases and the valence band decreases with photon energy a negative chirp would introduce a negative delay – meaning the W4f electrons would be perceived as arriving earlier in the streaking field than they actually are. This is the qualitative behavior we observe in the experiment. As an experimental proof for the magnitude of the effect we could introduce additional chirp to the pulse by employing a thicker metal filter or by using chirped XUV mirrors and then compare the obtained delays [73]. It is unlikely that the delay values measured at lower photon energies have been heavily affected by chirp since the typical XUV pulses for these energies were less strongly chirped than the ones we were using at $145\,\text{eV}$. We believe that the multilayer XUV mirror is responsible for the high XUV chirp. It was the first chromium/scandium multilayer mirror that was used in attosecond experiments and it introduces significant unwanted second order dispersion [127].

A manuscript reporting on the photon energy dependence of the photoemission delay is being prepared [128].

## 5.8 Outlook

Based on our experimental findings we are looking to perform the following experiments in the near future:

- Full compression of the NIR pulse.

Chapter 5 Attosecond Delay Spectroscopy on Tungsten

- Delay measurements at photon energies below 100 eV where we can generate enough XUV photons to obtain a very high signal. This allows us to compare data acquired with and without the electrostatic lens. Then we can reproduce the H/W data without the lens and clarify the rearrangement of valence band states in the Brillouin zone.

- Obtain Static spectra and possibly streaking measurements of H/W at low photon energies with the hemispherical detector. This is more challenging than the previous point but it would provide more detailed insight.

- A delay measurement at 112 eV – in between the two data points that show the drastic change in slope. With this experiment we can find out where the step really occurs and how steep it is – or whether there is even a peak.

- Variation of the chirp of the XUV pulse with the help of filters to verify the influence of chirp on the emission delay.

84

# Bibliography

[1]  M. Hentschel et al. "Attosecond metrology". In: *Nature* 414.6863 (2001), pp. 509–513 (cit. on pp. 1, 4, 12, 23).

[2]  A. Föhlisch et al. "Direct observation of electron dynamics in the attosecond domain." In: *Nature* 436.7049 (2005), pp. 373–6. DOI: `10.1038/nature03833` (cit. on p. 1).

[3]  T. Udem et al. "Accurate measurement of large optical frequency differences with a mode-locked laser". In: *Opt. Lett.* 24.13 (1999), pp. 881–883. DOI: `10.1364/OL.24.000881` (cit. on p. 2).

[4]  T. Fuji et al. "Attosecond control of optical waveforms". In: *New J. Phys.* 7 (2005), pp. 116–116. DOI: `10.1088/1367-2630/7/1/116` (cit. on p. 2).

[5]  P. Eckle et al. "Attosecond angular streaking". In: *Nat. Phys.* 4.7 (2008), pp. 565–570. DOI: `10.1038/nphys982` (cit. on p. 2).

[6]  P. Eckle et al. "Attosecond ionization and tunneling delay time measurements in helium." In: *Science* 322.5907 (2008), pp. 1525–9. DOI: `10.1126/science.1163439` (cit. on p. 2).

[7]  L. Torlina et al. "Interpreting Attoclock Measurements of Tunnelling Times". In: *ArXiv e-prints* (2014). arXiv: `1402.5620 [physics.atom-ph]` (cit. on p. 2).

[8]  B. Bergues et al. "Attosecond tracing of correlated electron-emission in non-sequential double ionization." In: *Nat. Commun.* 3.May (2012), p. 813. DOI: `10.1038/ncomms1807` (cit. on p. 2).

[9]  T. Wittmann et al. "Single-shot carrier–envelope phase measurement of few-cycle laser pulses". In: *Nat. Phys.* 5.5 (2009), pp. 357–362. DOI: `10.1038/nphys1250` (cit. on p. 2).

[10]  A. Mcpherson et al. "Studies of multiphoton production of vacuum-ultraviolet radiation in the rare gases". In: *J. Opt. Soc. Am. B* 4.4 (1987), pp. 595–601 (cit. on pp. 2, 9).

[11]  P. B. Corkum. "Plasma perspective on strong field multiphoton ionization". In: *Phys. Rev. Lett.* 71.13 (1993), pp. 1994–1997. DOI: `10.1103/PhysRevLett.71.1994` (cit. on pp. 2, 9, 10).

[12]  J. Itatani et al. "Tomographic imaging of molecular orbitals". In: *Nature* 432.7019 (2004), pp. 867–871 (cit. on p. 2).

[13]    N. L. Wagner et al. "Monitoring molecular dynamics using coherent electrons from high harmonic generation". In: *Proc. Natl. Acad. Sci.* 103.36 (2006), pp. 13279–13285. DOI: `10.1073/pnas.0605178103` (cit. on p. 2).

[14]    H. J. Wörner et al. "Following a chemical reaction using high-harmonic interferometry." In: *Nature* 466.7306 (2010), pp. 604–7. DOI: `10.1038/nature09185` (cit. on p. 2).

[15]    H. Dachraoui et al. "Photoinduced Reconfiguration Cycle in a Molecular Adsorbate Layer Studied by Femtosecond Inner-Shell Photoelectron Spectroscopy". In: *Phys. Rev. Lett.* 106.10 (2011), pp. 46–49. DOI: `10.1103/PhysRevLett.106.107401` (cit. on pp. 3, 58, 64).

[16]    K. Zhao et al. "Tailoring a 67 attosecond pulse through advantageous phase-mismatch". In: *Opt. Lett.* 37.18 (2012), pp. 3891–3893. DOI: `10.1364/OL.37.003891` (cit. on p. 3).

[17]    E. Goulielmakis et al. "Real-time observation of valence electron motion". In: *Nature* 466.7307 (2010), pp. 739–743 (cit. on p. 3).

[18]    M. Schultze et al. "Controlling dielectrics with the electric field of light". In: *Nature* 493.7430 (2013), pp. 75–78 (cit. on p. 3).

[19]    M. Schultze et al. "Delay in Photoemission". In: *Science* 328.5986 (2010), pp. 1658–1662. DOI: `10.1126/science.1189401` (cit. on pp. 4, 78).

[20]    A. L. Cavalieri et al. "Attosecond spectroscopy in condensed matter." In: *Nature* 449.7165 (2007), pp. 1029–32. DOI: `10.1038/nature06229` (cit. on pp. 4, 6, 14, 65–69).

[21]    W. A. Okell et al. "Attosecond streaking of photoelectron emission from disordered solids". In: *ArXiv e-prints* (2014). arXiv: `1410.5613 [physics.optics]` (cit. on p. 4).

[22]    S. Neppl et al. "Direct observation of electron propagation and dielectric screening on the atomic length scale". In: *Accept. Publ. Nat.* (2014) (cit. on pp. 4, 25).

[23]    J. H. Houtgraaf, J. Versmissen, and W. J. van der Giessen. "A concise review of DNA damage checkpoints and repair in mammalian cells." In: *Cardiovasc. Revasc. Med.* 7.3 (2006), pp. 165–72. DOI: `10.1016/j.carrev.2006.02.002` (cit. on p. 5).

[24]    J. C. Farman, B. G. Gardiner, and J. D. Shanklin. "Large losses of total ozone in Antarctica reveal seasonal ClOx/NOx interaction". In: *Nature* 315 (1985), pp. 207–210. DOI: `10.1038/315207a0` (cit. on p. 5).

[25]    A. Jones and J. Shanklin. "Continued decline of total ozone over Halley, Antarctica, since 1985". In: *Nature* 376.6539 (1995), pp. 409–411 (cit. on p. 5).

[26]    Y. Matsumi and M. Kawasaki. "Photolysis of atmospheric ozone in the ultraviolet region." In: *Chem. Rev.* 103.12 (2003), pp. 4767–82. DOI: `10.1021/cr0205255` (cit. on p. 5).

[27] G. J. Halász et al. "Simulation of laser-induced quantum dynamics of the electronic and nuclear motion in the ozone molecule on the attosecond time scale". In: *Phys. Rev. A* 86.4 (2012), p. 043426. DOI: `10.1103/PhysRevA.86.043426` (cit. on pp. 5, 41, 44).

[28] B. Mignolet, R. D. Levine, and F. Remacle. "Localized electron dynamics in attosecond-pulse-excited molecular systems: Probing the time-dependent electron density by sudden photoionization". In: *Phys. Rev. A* 86.5 (2012), p. 053429. DOI: `10.1103/PhysRevA.86.053429` (cit. on p. 5).

[29] F. Remacle and R. D. Levine. "An electronic time scale in chemistry". In: *Proc. Natl. Acad. Sci. U. S. A.* 103.18 (2006), pp. 6793–6798. DOI: `10.1073/pnas.0601855103` (cit. on p. 5).

[30] M. Grätzel. "Dye-sensitized solar cells". In: *J. Photochem. Photobiol. C Photochem. Rev.* 4.2 (2003), pp. 145–153. DOI: `10.1016/S1389-5567(03)00026-1` (cit. on pp. 5, 51).

[31] B. Oregan and M. Gratzel. "A Low-cost, High-efficiency Solar-cell Based On Dye-sensitized Colloidal Tio2 Films". In: *Nature* 353.6346 (1991), pp. 737–740 (cit. on p. 5).

[32] J. Schnadt et al. "Experimental evidence for sub-3-fs charge transfer from an aromatic adsorbate to a semiconductor". In: *Nature* 418 (2002), pp. 620–623 (cit. on p. 5).

[33] R. W. Boyd. *Nonlinear Optics*. 3rd editio. Academic Press Inc, 2003 (cit. on pp. 8, 9, 15).

[34] K. Kulander, K. Schafer, and J. Krause. "Dynamics of short-pulse excitation, ionization and harmonic conversion". In: *Super-Intense Laser-Atom Phys.* Ed. by B. Piraux, A. L'huillier, and K. Rzazewski. Vol. 316. New York: Plenum, 1993, p. 95 (cit. on p. 9).

[35] K. J. Schafer et al. "Above threshold ionization beyond the high harmonic cutoff". In: *Phys. Rev. Lett.* 70.11 (1993), pp. 1599–1602. DOI: `10.1103/PhysRevLett.70.1599` (cit. on p. 9).

[36] M. Lewenstein et al. "Theory of high-harmonic generation by low-frequency laser fields". In: *Phys. Rev. A* 49.3 (1994), pp. 2117–2132. DOI: `10.1103/PhysRevA.49.2117` (cit. on p. 9).

[37] K. Varjú et al. "Physics of attosecond pulses produced via high harmonic generation". In: *Am. J. Phys.* 77.5 (2009), p. 389. DOI: `10.1119/1.3086028` (cit. on pp. 10, 11).

[38] G. Sansone et al. "Isolated single-cycle attosecond pulses." In: *Science (80-. ).* 314.5798 (2006), pp. 443–6. DOI: `10.1126/science.1132838` (cit. on p. 10).

[39] P. Heissler et al. "Few-Cycle Driven Relativistically Oscillating Plasma Mirrors: A Source of Intense Isolated Attosecond Pulses". In: *Phys. Rev. Lett.* 108.23 (2012), p. 235003. DOI: `10.1103/PhysRevLett.108.235003` (cit. on p. 10).

[40]   T. W. Barbee , Jr., S. Mrowka, and M. C. Hettrick. "Molybdenum-silicon multi-layer mirrors for the extreme ultraviolet". In: *Appl. Opt.* 24.6 (1985), p. 883. DOI: 10.1364/AO.24.000883 (cit. on p. 10).

[41]   M. Hofstetter et al. "Lanthanum-molybdenum multilayer mirrors for attosecond pulses between 80 and 130 eV". In: *New J. Phys.* 13.6 (2011), p. 063038. DOI: 10.1088/1367-2630/13/6/063038 (cit. on p. 10).

[42]   V. S. Yakovlev, F. Bammer, and A. Scrinzi. "Attosecond streaking measurements". In: *J. Mod. Opt.* 52.2-3 (2005), pp. 395–410. DOI: 10.1080/09500340412331283642 (cit. on p. 11).

[43]   F. Krausz and M. Ivanov. "Attosecond physics". In: *Rev. Mod. Phys.* 81.1 (2009), pp. 163–234. DOI: 10.1103/RevModPhys.81.163 (cit. on p. 11).

[44]   J. Gagnon. "Attosecond electron spectroscopy theory and its applications". PhD thesis. Ludwig-Maximilians-Universität München, 2010 (cit. on pp. 11, 78).

[45]   D. J. Bradley, B. Liddy, and W. E. Sleat. "Direct linear measurement of ultra-short light pulses with a picosecond streak camera". In: *Opt. Commun.* 2.8 (1971), pp. 391–395. DOI: http://dx.doi.org/10.1016/0030-4018(71)90252-5 (cit. on p. 11).

[46]   E. Goulielmakis et al. "Direct measurement of light waves." In: *Science* 305.5688 (2004), pp. 1267–9. DOI: 10.1126/science.1100866 (cit. on p. 13).

[47]   R. Kienberger et al. "Atomic transient recorder". In: *Nature* 427.6977 (2004), pp. 817–821 (cit. on p. 14).

[48]   V. S. Yakovlev et al. "Attosecond Streaking Enables the Measurement of Quantum Phase". In: *Phys. Rev. Lett.* 105.7 (2010), p. 073001. DOI: 10.1103/PhysRevLett.105.073001 (cit. on p. 14).

[49]   M. T. Ossiander. "On the Expansion of Attosecond Streaking Spectroscopy towards Ultrafast Surface Dynamics". MA thesis. Technische Universität München, 2014 (cit. on p. 14).

[50]   P. Baum, S. Lochbrunner, and E. Riedle. "Generation of tunable 7-fs ultraviolet pulses: achromatic phase matching and chirp management". In: *Appl. Phys. B* 79.8 (2004), pp. 1027–1032. DOI: 10.1007/s00340-004-1668-2 (cit. on p. 15).

[51]   P. Baum, S. Lochbrunner, and E. Riedle. "Tunable sub-10-fs ultraviolet pulses generated by achromatic frequency doubling." In: *Opt. Lett.* 29.14 (2004), pp. 1686–8 (cit. on p. 15).

[52]   F. Reiter et al. "Generation of sub-3 fs pulses in the deep ultraviolet." In: *Opt. Lett.* 35.13 (2010), pp. 2248–50 (cit. on pp. 15, 36, 39, 50).

[53]   R. Trebino. *Frequency-Resolved Optical Gating: The Measurement of Ultrashort Laser Pulses.* Boston, MA: Springer US, 2000. DOI: 10.1007/978-1-4615-1181-6 (cit. on p. 16).

[54]   R. Trebino et al. "Measuring ultrashort laser pulses in the time-frequency do-main using frequency-resolved optical gating". In: *Rev. Sci. Instrum.* 68.9 (1997), p. 3277. DOI: 10.1063/1.1148286 (cit. on p. 16).

[55]   J. N. Sweetser, D. N. Fittinghoff, and R. Trebino. "Transient-grating frequency-resolved optical gating." In: *Opt. Lett.* 22.8 (1997), pp. 519–21 (cit. on p. 16).

[56]   H. W. Schweinberger. "A Laser Source for the Generation of Intense Attosecond Pulses and its First Applications". PhD thesis. Ludwig-Maximilians-Universität München, 2014 (cit. on p. 17).

[57]   R. Szipocs et al. "Chirped multilayer coatings for broadband dispersion control in femtosecond lasers." In: *Opt. Lett.* 19.3 (1994), p. 201 (cit. on p. 17).

[58]   A. Stingl et al. "Sub-10-fs mirror-dispersion-controlled Ti:sapphire laser." In: *Opt. Lett.* 20.6 (1995), pp. 602–4 (cit. on p. 17).

[59]   T. Fuji et al. "Monolithic carrier-envelope phase-stabilization scheme." In: *Opt. Lett.* 30.3 (2005), pp. 332–4 (cit. on p. 17).

[60]   D. Strickland and G. Mourou. "Compression of amplified chirped optical pulses". In: *Opt. Commun.* 55.6 (1985), pp. 447–449 (cit. on p. 17).

[61]   P. Tournois. "Acousto-optic programmable dispersive filter for adaptive compen-sation of group delay time dispersion in laser systems". In: *Opt. Commun.* 4018.Au-gust (1997) (cit. on p. 17).

[62]   T. Clausnitzer et al. "Highly efficient transmission gratings in fused silica for chirped-pulse amplification systems". In: *Appl. Opt.* 42.34 (2003), pp. 6934–6938. DOI: 10.1364/AO.42.006934 (cit. on p. 21).

[63]   J. Rauschenberger et al. "Carrier-envelope phase-stabilized amplifier system". In: *Laser Phys. Lett.* 3.1 (2006), pp. 37–42. DOI: 10.1002/lapl.200510053 (cit. on p. 21).

[64]   A. Baltuska et al. "Phase-controlled amplification of few-cycle laser pulses". In: *Sel. Top. Quantum Electron. IEEE J.* 9.4 (2003), pp. 972–989. DOI: 10.1109/JSTQE.2003.819107 (cit. on p. 21).

[65]   A. L. Cavalieri et al. "Intense 1.5-cycle near infrared laser waveforms and their use for the generation of ultra-broadband soft-x-ray harmonic continua". In: *New J. Phys.* 9.7 (2007), p. 242 (cit. on pp. 22, 57).

[66]   P. O'shea et al. "Increased-bandwidth in ultrashort-pulse measurement using an angle-dithered nonlinear-optical crystal". In: *Opt. Express* 7.10 (2000), p. 342. DOI: 10.1364/OE.7.000342 (cit. on p. 22).

[67]   Patrick Rupprecht. "FROG / 2DSI dual Characterization of Femtosecond Pulses using External Dithering". BA thesis. Technische Universität München, 2014 (cit. on p. 23).

[68]   E. Magerl et al. "A flexible apparatus for attosecond photoelectron spectroscopy of solids and surfaces". In: *Rev. Sci. Instrum.* 82.6 (2011), p. 063104. DOI: 10.1063/1.3596564 (cit. on pp. 23, 26).

[69]   S. Neppl. "Attosecond Time-Resolved Photoemission from Surfaces and Interfaces". PhD thesis. Technische Universität München, 2012 (cit. on pp. 25, 26, 67–71, 74, 75).

[70]   S. Hüfner. *Photoelectron spectroscopy: principles and applications.* Springer Verlag, 2003 (cit. on pp. 25, 55).

[71]   A. Naumkin et al. *NIST XPS Database.* 2012 (cit. on pp. 26, 56).

[72]   K. Varju, P. Johnsson, and R. Lopez-martens. "Experimental studies of attosecond pulse trains". In: *Laser Phys.* 15.6 (2005), pp. 888–898 (cit. on p. 26).

[73]   M. Hofstetter et al. "Attosecond dispersion control by extreme ultraviolet multilayer mirrors." In: *Opt. Express* 19.3 (2011), pp. 1767–76 (cit. on pp. 26, 83).

[74]   S. Neppl et al. "Attosecond Time-Resolved Photoemission from Core and Valence States of Magnesium". In: *Phys. Rev. Lett.* 109.8 (2012), p. 087401. DOI: `10.1103/PhysRevLett.109.087401` (cit. on p. 26).

[75]   M. Fiess et al. "Versatile apparatus for attosecond metrology and spectroscopy". In: *Rev. Sci. Instrum.* 81.9 (2010), p. 93103. DOI: `10.1063/1.3475689` (cit. on p. 27).

[76]   C. Jakubeit. "Upgrade of an Attosecond Beamline". MA thesis. Technische Universität München, 2013 (cit. on pp. 27, 28).

[77]   A. Serdyuchenko et al. "High spectral resolution ozone absorption cross-sections – Part 2: Temperature dependence". In: *Atmos. Meas. Tech.* 7.2 (2014), pp. 625–636. DOI: `10.5194/amt-7-625-2014` (cit. on p. 30).

[78]   H. Keller-rudek et al. "The MPI-Mainz UV/VIS Spectral Atlas of Gaseous Molecules of Atmospheric Interest". In: *Earth Syst. Sci. Data* 5.2 (2013), pp. 365–373. DOI: `10.5194/essd-5-365-2013` (cit. on p. 30).

[79]   S. Sander et al. "Chemical Kinetics and Photochemical Data for Use in Atmospheric Studies. Evaluation Number 15". In: *JPL Publ.* 06-2 (2006) (cit. on p. 30).

[80]   G. M. Platz and C. K. Hersh. "Preparation of Liquid Ozone and Ozone-Oxygen Mixtures for Rocket Application". In: *Ind. Eng. Chem.* 48.4 (1956), pp. 742–744. DOI: `10.1021/ie50556a024` (cit. on p. 31).

[81]   G. A. Cook et al. "Explosion Limits of Ozone-oxygen Mixtures". In: *Ind. Eng. Chem.* 48.4 (1956), pp. 736–741 (cit. on p. 31).

[82]   H. von Siemens. "Über Dampfdruckmessungen und Thermometrie bei tiefen Temperaturen". In: *Ann. Phys.* 42.14 (1913), 871–U40 (cit. on p. 31).

[83]   D. Hanson and K. Mauersberger. "The Vapor-pressures of Solid and Liquid Ozone". In: *J. Chem. Phys.* 85.8 (1986), pp. 4669–4672 (cit. on p. 31).

[84]   E. Coleman et al. "A Versatile Low-pressure Ozone Source". In: *J. Vac. Sci. Technol. A* 9.4 (1991), pp. 2408–2409 (cit. on p. 31).

[85]   U. Graf et al. "Intense few-cycle light pulses in the deep ultraviolet". In: *Opt. Express* 16.23 (2008), pp. 18956–18963 (cit. on pp. 32, 36, 39, 50).

[86]  T. Metzger et al. "High-repetition-rate picosecond pump laser based on a Yb:YAG disk amplifier for optical parametric amplification". In: *Opt. Lett.* 34.14 (2009), pp. 2123–2125. DOI: 10.1364/OL.34.002123 (cit. on p. 33).

[87]  S. Kahra et al. "A molecular conveyor belt by controlled delivery of single molecules into ultrashort laser pulses". In: *Nat. Phys.* 8.3 (2012), pp. 238–242. DOI: 10.1038/nphys2214 (cit. on p. 39).

[88]  A. Schiffrin et al. "Optical-field-induced current in dielectrics." In: *Nature* 493.7430 (2013), pp. 70–4. DOI: 10.1038/nature11567 (cit. on p. 40).

[89]  S. Y. Grebenshchikov et al. "New theoretical investigations of the photodissociation of ozone in the Hartley, Huggins, Chappuis, and Wulf bands". In: *Phys. Chem. Chem. Phys.* 9.17 (2007), pp. 2044–2064. DOI: 10.1039/b701020f (cit. on p. 40).

[90]  G. J. Halász et al. "Coherence revival during the attosecond electronic and nuclear quantum photodynamics of the ozone molecule". In: *Phys. Rev. A* 88.2 (2013), p. 023425. DOI: 10.1103/PhysRevA.88.023425 (cit. on pp. 41, 43).

[91]  D. Imre et al. "Chemical dynamics studied by emission spectroscopy of dissociating molecules". In: *J. Phys. Chem.* 88.18 (1984), pp. 3956–3964. DOI: 10.1021/j150662a017 (cit. on p. 42).

[92]  A. Perveaux et al. "Attosecond electronic and nuclear quantum photodynamics of ozone: time-dependent Dyson orbitals and dipole". In: *J. Phys. B At. Mol. Opt. Phys.* 47.12 (2014), p. 124010. DOI: 10.1088/0953-4075/47/12/124010 (cit. on p. 42).

[93]  L. Grill and C. Joachim. *Imaging and Manipulating Molecular Orbitals.* September. Springer Berlin Heidelberg, 2013. DOI: http://dx.doi.org/10.1007/978-3-642-38809-5?nosfx=yVerlagVolltext (cit. on pp. 42, 54).

[94]  A. Perveaux et al. "Monitoring the Birth of an Electronic Wavepacket in a Molecule with Attosecond Time-Resolved Photoelectron Spectroscopy". In: *J. Phys. Chem. A* 118.38 (2014), pp. 8773–8778. DOI: 10.1021/jp508218n (cit. on pp. 42, 43).

[95]  T. Latka. *Private Communications* (cit. on p. 44).

[96]  F. Schwabl. *Quantenmechanik.* Springer Verlag, 2008 (cit. on p. 44).

[97]  D. Kuciauskas et al. "Transient Absorption Spectroscopy of Ruthenium and Osmium Polypyridyl Complexes Adsorbed onto Nanocrystalline TiO2 Photoelectrodes". In: *J. Phys. Chem. B* 106.36 (2002), pp. 9347–9358 (cit. on p. 51).

[98]  G. Sauve et al. "Dye sensitization of nanocrystalline titanium dioxide with osmium and ruthenium polypyridyl complexes". In: *J. Phys. Chem. B* 104.29 (2000), pp. 6821–6836. DOI: 10.1021/jp0002143 (cit. on pp. 52, 54).

[99]  S. Tanuma, C. J. Powell, and D. R. Penn. "Calculations of electron inelastic mean free paths. IX. Data for 41 elemental solids over the 50 eV to 30 keV range". In: *Surf. Interface Anal.* 43.3 (2011), pp. 689–713. DOI: 10.1002/sia.3522 (cit. on pp. 53, 68).

[100]   A. Schiffrin. *Private Communications.* 2012 (cit. on p. 54).

[101]   J. Yeh and I. Lindau. "Atomic subshell photoionization cross sections and asymmetry parameters". In: *At. data Nucl. data tables* 32.l (1985) (cit. on pp. 54, 70).

[102]   *Atomic Calculation of Photoionization Cross-Sections and Asymmetry Parameters* (cit. on pp. 54, 70).

[103]   J. V. Barth. "Molecular architectonic on metal surfaces." In: *Annu. Rev. Phys. Chem.* 58 (2007), pp. 375–407. DOI: `10.1146/annurev.physchem.56.092503.141259` (cit. on p. 54).

[104]   H. Dürr and H. Bouas-laurent. *Photochromism: Molecules and Systems.* Elsevier Science, 2003 (cit. on p. 54).

[105]   T. A. Heimer, C. A. Bignozzi, and G. J. Meyer. "Molecular-level Photovoltaics - the Electrooptical Properties of Metal Cyanide Complexes Anchored To Titaniumdioxide". In: *J. Phys. Chem.* 97.46 (1993), pp. 11987–11994 (cit. on p. 54).

[106]   K.-L. Wu et al. "Engineering of osmium(II)-based light absorbers for dye-sensitized solar cells." In: *Angew. Chem. Int. Ed. Engl.* 51.23 (2012), pp. 5642–6. DOI: `10.1002/anie.201200071` (cit. on p. 54).

[107]   M. Majewski and M. Wolf. *Private Communications.* 2012 (cit. on p. 58).

[108]   F. Evangelista et al. "Electronic structure of copper phthalocyanine: an experimental and theoretical study of occupied and unoccupied levels." In: *J. Chem. Phys.* 126.12 (2007), p. 124709. DOI: `10.1063/1.2712435` (cit. on pp. 61, 62).

[109]   M. El-nahass et al. "Structural and optical properties of thermal evaporated magnesium phthalocyanine (MgPc) thin films". In: *Appl. Surf. Sci.* 254.8 (2008), pp. 2458–2465. DOI: `10.1016/j.apsusc.2007.09.064` (cit. on p. 61).

[110]   G. Binnig et al. "Surface studies by scanning tunneling microscopy". In: *Phys. Rev. Lett.* 49.1 (1982) (cit. on p. 61).

[111]   J. F. Horstbrink. "Zeitaufgelöste spektroskopische Untersuchung ultraschneller Moleküldynamik". MA thesis. Technische Universität München, 2014 (cit. on p. 62).

[112]   M. Gerl. "Time-resolved investigation of photoelectron dynamics by Attosecond Streaking Spectroscopy on solids". MA thesis. Technische Universität München, 2013 (cit. on pp. 67, 69).

[113]   C.-H. Zhang and U. Thumm. "Attosecond Photoelectron Spectroscopy of Metal Surfaces". In: *Phys. Rev. Lett.* 102.12 (2009), p. 123601. DOI: `10.1103/PhysRevLett.102.123601` (cit. on pp. 67, 68).

[114]   C. Lemell et al. "Simulation of attosecond streaking of electrons emitted from a tungsten surface". In: *Phys. Rev. A* 79.6 (2009), p. 062901. DOI: `10.1103/PhysRevA.79.062901` (cit. on pp. 67, 68).

[115]   A. Kazansky and P. Echenique. "One-Electron Model for the Electronic Response of Metal Surfaces to Subfemtosecond Photoexcitation". In: *Phys. Rev. Lett.* 102.17 (2009), p. 177401. DOI: `10.1103/PhysRevLett.102.177401` (cit. on pp. 67, 68).

[116]   E. E. Krasovskii. "Attosecond spectroscopy of solids: Streaking phase shift due to lattice scattering". In: *Phys. Rev. B* 84.19 (2011), p. 195106. DOI: 10.1103/PhysRevB.84.195106 (cit. on pp. 68, 69).

[117]   C. H. Zhang and U. Thumm. "Effect of wave-function localization on the time delay in photoemission from surfaces". In: *Phys. Rev. A - At. Mol. Opt. Phys.* 84 (2011). DOI: 10.1103/PhysRevA.84.065403 (cit. on p. 68).

[118]   A. Borisov et al. "Resonant and nonresonant processes in attosecond streaking from metals". In: *Phys. Rev. B* 87.12 (2013), p. 121110. DOI: 10.1103/PhysRevB.87.121110 (cit. on pp. 68, 69).

[119]   R. Bartynski et al. "Angle-resolved photoemission study of the surface and bulk electronic structure of Mg (0001) and Mg (112- 0)". In: *Phys. Rev. B* 33.6 (1986) (cit. on p. 68).

[120]   F. Schiller et al. "Electronic structure of Mg: From monolayers to bulk". In: *Phys. Rev. B* 70.12 (2004), p. 125106. DOI: 10.1103/PhysRevB.70.125106 (cit. on p. 68).

[121]   B. Feuerbacher and B. Fitton. "Electronic energy levels of hydrogen adsorbed on tungsten". In: *Phys. Rev. B* 8.10 (1973) (cit. on p. 69).

[122]   E. Rotenberg and S. Kevan. "Evolution of Fermi level crossings versus H coverage on W (110)". In: *Phys. Rev. Lett.* (1998), pp. 2905–2908 (cit. on p. 69).

[123]   A. Kim. "TBD". PhD thesis. Technische Universität München, 2014 (cit. on pp. 70, 75).

[124]   M. Stöhr. "First Principles Investigations of Adsorption on a Transition Metal Surface: Oxygen and Indium on the (110) Surface of Tungsten". PhD thesis. Universität Wien, 2009 (cit. on p. 71).

[125]   J. Gagnon, E. Goulielmakis, and V. Yakovlev. "The accurate FROG characterization of attosecond pulses from streaking measurements". In: *Appl. Phys. B* 92.1 (2008), pp. 25–32. DOI: 10.1007/s00340-008-3063-x (cit. on p. 78).

[126]   M. Sabbar, S. Heuser, and R. Boge. "Attochirp-corrected photo ionization time delays using coincidence attosecond streaking". In: *arXiv* (2014) (cit. on p. 83).

[127]   A. Guggenmos et al. "Ion polished Cr/Sc attosecond multilayer mirrors for high water window reflectivity". In: *Opt. Express* 22.22 (2014), p. 26526. DOI: 10.1364/OE.22.026526 (cit. on p. 83).

[128]   M. Jobst et al. "Excitation energy dependent photoemission timing in tungsten". In: *Prep.* (2015) (cit. on p. 83).

# Curriculum Vitae

**Michael Jobst**
born on August 2nd,1982

*Education*

| | |
|---|---|
| 04/2010—12/2014 | PhD student at the Max Planck Institut for Quantum Optics in the group of Prof. Dr. Reinhard Kienberger and the department of Prof. Dr. Krausz |
| 08/2008—08/2009 | Diploma thesis at ETH Zürich under supervision of Prof. Dr. Vahid Sandoghdar |
| 08/2006—06/2007 | Studies of physics at the University of Colorado at Boulder, USA |
| 09/2003—08/2009 | Studies of physics at the Universität Regensburg |
| 2002 | Abitur at Gymnasium Neutraubling |

*Teaching*

| | |
|---|---|
| 2012–2014 | Advanced laboratory course, TU München |
| 2008–2009 | Teaching assistant for several lectures, ETH Zürich |

# Publication List

**P1**   S. Neppl, R. Ernstorfer, A. L. Cavalieri, C. Lemell, G. Wachter, E. Magerl, E. Bothschafter, **M. Jobst**, M. Hofstetter, U. Kleineberg, J. Barth, D. Menzel, J. Burgdörfer, P. Feulner, F. Krausz, and R. Kienberger. "Direct observation of electron propagation and dielectric screening on the atomic length scale". *Accepted for publication in Nature* (2014).

**P2**   **M. Jobst**, S. Neppl, E. Bothschafter, J. Riemensberger, M. Ossiander, M. Schäffer, E. Magerl, A. Kim, P. Feulner, and R. Kienberger. "Excitation energy dependent photoemission timing in tungsten. *In preparation* (2015).

## Presentations

**O1**   **M. Jobst**, M. Fieß, A. Sommer, S. Holzner, M. Schultze, F. Krausz and R. Kienberger., "Towards time resolving attosecond electron dynamics in ozone". *ATTOFEL Summer School in Crete* (2011)

**O2**   **M. Jobst**, S. Neppl, E. Bothschafter, W. Helml, A. Schiffrin, R. Ernstorfer, F. Krausz, and R. Kienberger. "Attosecond spectroscopy on solid surfaces (Poster Presentation)". *ATTOFEL Meeting in Berlin* (2011)

**O3**   **M. Jobst**, M. Fieß, A. Sommer, S. Holzner, M. Schultze, F. Krausz, and R. Kienberger. "Towards time resolving attosecond electron dynamics in ozone". *FEMTO10 – The Madrid Conference on Femtochemistry, Poster Presentation* (2011)

**O4**   **M. Jobst**, J. Riemensberger, M. Ossiander, M. Schäffer, S. Neppl, A.Kim, A.Guggenmoos, J.V. Barth, F. Krausz, P. Feulner, and R. Kienberger. "Photon-energy Dependent Delays in Photoemission from Tungsten Surfaces". *MAP-B Symposium* (2014)

**O5**   **M. Jobst**. "Attosecond Dynamics in Molecules and on Interfaces". *Multiple oral contributions to the International Max Planck Research School of Advanced Photon Science*

# Chapter 6

# Acknowledgement

record speed. When Alex promised a mirror in two weeks you would get it in two days.
Special thanks to Nicholas Karpowicz for always being approachable with any question.
I am convinced that it is impossible to have a five minute conversation with Nick without
becoming smarter in the process.

Everyone in my office was incredibly relieved when it was confirmed that Peter Feulner
would continue working after his 65th birthday. His unmatched laboratory experience is
simply irreplaceable and was tremendously helpful.

Miss Wild and her general unstoppability guaranteed that Frauenchiemsee and every
IMPRS event was flawlessly organized. I am sure she would be capable of herding cats
without breaking a sweat.

I am grateful to the mechanical workshop of MPQ for dealing with my small requests
spontaneously – and with my large requests in time.

My deepest gratitude goes to my parents for always supporting me.

And last but definitely not least: thank you, Katharina. For everything.